



HAL
open science

Gas-sheared falling liquid films beyond the absolute instability limit

Misa Ishimura, Sophie Mergui, Christian Ruyer-Quil, Georg F. Dietze

► **To cite this version:**

Misa Ishimura, Sophie Mergui, Christian Ruyer-Quil, Georg F. Dietze. Gas-sheared falling liquid films beyond the absolute instability limit. *Journal of Fluid Mechanics*, 2023, 971, pp.A37. 10.1017/jfm.2023.670 . hal-04304395

HAL Id: hal-04304395

<https://hal.science/hal-04304395v1>

Submitted on 24 Nov 2023

HAL is a multi-disciplinary open access archive for the deposit and dissemination of scientific research documents, whether they are published or not. The documents may come from teaching and research institutions in France or abroad, or from public or private research centers.

L'archive ouverte pluridisciplinaire **HAL**, est destinée au dépôt et à la diffusion de documents scientifiques de niveau recherche, publiés ou non, émanant des établissements d'enseignement et de recherche français ou étrangers, des laboratoires publics ou privés.

Banner appropriate to article type will appear here in typeset article

1 **Gas-sheared falling liquid films beyond the absolute** 2 **instability limit**

3 **Misa Ishimura^{1,3,4}, S. Mergui^{1,2}, C. Ruyer-Quil³, and G. F. Dietze¹†**

4 ¹Université Paris-Saclay, CNRS, FAST, 91405, Orsay, France.

5 ²Sorbonne Université, UFR 919, 4 place Jussieu, F-75252 Paris CEDEX 05, France.

6 ³Université Savoie Mont Blanc, CNRS, LOCIE, 73376 Le Bourget du Lac, France.

7 ⁴Department of Mechanical Engineering, Yokohama National University, Kanagawa 240-8501, Japan.

8 (Received 9 August 2023; revised xx; accepted xx)

9 We study the effect of a confined turbulent counter-current gas flow on the waviness of a
10 weakly-inclined falling liquid film. Our study is centered on experiments in a channel of 13
11 mm height, using water and air, where we have successively increased the counter-current gas
12 flow rate until flooding. Computations with a new low-dimensional model and linear stability
13 calculations are used to elucidate the linear and nonlinear wave dynamics. We find that the gas
14 pressure gradient plays an important role in countering the stabilizing effect of the tangential
15 gas shear stress at the liquid-gas interface. At very low inclination angles, the latter effect
16 dominates and can suppress the long-wave Kapitza instability unconditionally. By contrast,
17 for non-negligible inclination, the gas-effect is linearly destabilizing, amplifies the height of
18 nonlinear Kapitza waves, and exacerbates coalescence-induced formation of large-amplitude
19 tsunami waves. Kapitza waves do not undergo any catastrophic transformation when the
20 counter-current gas flow rate is increased beyond the absolute instability (AI) limit. On the
21 contrary, we find that AI is an effective linear wave selection mechanism in a noise-driven
22 wave evolution scenario, leading to highly regular downward-travelling nonlinear wave trains,
23 which preclude coalescence events. In our experiments, where Kapitza waves develop in a
24 protected region before coming into contact with the gas, flooding is eventually caused far
25 beyond the AI limit by upward-travelling short-wave ripples. Based on our linear stability
26 calculations for arbitrary wave numbers, we have uncovered a new short-wave interfacial
27 instability mode with negative linear wave speed, causing these ripples.

28 **Key words:** Thin films, gas/liquid flow

29 **1. Introduction**

30 Falling liquid films intervene in many engineering applications (Alekseenko *et al.* 2007;
31 Azzopardi *et al.* 2011; Lapkin & Anastas 2018). One example are rectification columns
32 containing structured packings for cryogenic air separation (Fair & Bravo 1990), where

† Email address for correspondence: dietze@fast.u-psud.fr

the liquid film is subject to a turbulent counter-current gas flow within narrow channels (Valluri *et al.* 2005). Surface waves, forming at the liquid-gas interface due to the inertia-driven Kapitza instability (Kapitza 1948), which consist of large humps preceded by several precursory capillary ripples, are known to greatly intensify inter-phase heat and mass transfer (Yoshimura *et al.* 1996; Miyara 1999; Dietze 2019). At the same time, they can trigger flooding events (Bankoff & Lee 1986) that are detrimental to adequate process operation. Such events include obstruction of the channel cross-section (Vlachos *et al.* 2001), wave reversal (Tseluiko & Kalliadasis 2011), fragmentation and droplet entrainment (Zapke & Kröger 2000), or (partial) liquid reversal (Trifonov 2010*b*, 2019). In light of these two competing roles played by surface waves, numerous experimental (Vlachos *et al.* 2001; Drosos *et al.* 2006; Kofman *et al.* 2017), numerical (Trifonov 2010*a*; Vellingiri *et al.* 2015; Schmidt *et al.* 2016; Trifonov 2019; Lavalle *et al.* 2019), and modelling (Tseluiko & Kalliadasis 2011; Dietze & Ruyer-Quil 2013; Lavalle *et al.* 2020, 2021) works have been dedicated to unraveling the effect of a counter-current gas flow on the linear and nonlinear dynamics of wavy falling liquid films. Our current manuscript seeks to further contribute to this task.

We study the configuration of a laminar falling liquid film sheared by a turbulent counter-current gas flow confined in a rectangular channel of height $H^* \sim 10$ mm (the star superscript denotes dimensional quantities throughout), according to the experimental setup sketched in figure 1. The confinement level chosen here is representative of structured packings (Fair & Bravo 1990) and lies in between those used in the experiments of Lavalle *et al.* (2019), $H^* \sim 5$ mm, where the gas flow was laminar, and those of Kofman *et al.* (2017), $H^* \sim 20$ mm, where the confinement was weak and the gas flow was turbulent. We have applied three different approaches to study this flow: (i) experiments, where developed surface waves of prescribed frequency were produced within a protected zone before being submitted to the counter-current gas flow, (ii) linear stability analysis based on the full governing equations, and (iii) nonlinear numerical computations with a new integral boundary layer model. Our study is guided by a set of experimental runs, where we have successively increased the counter-current gas flow rate, starting from conditions where the gas-effect is weak, up until breakdown of the experiment due to flooding. Computations with our low-dimensional model and linear stability calculations have allowed us to elucidate the linear and nonlinear wave dynamics associated with this transition.

We focus mainly (but not exclusively) on weakly-inclined falling liquid films, which allows to investigate weakly supercritical flow regimes. According to Brooke Benjamin (1957) and Yih (1963), the onset of the Kapitza instability for a liquid film falling in a passive atmosphere is given by $\text{Re}_L = 5/6 \cot(\phi)$, where ϕ denotes the inclination angle, and $\text{Re}_L = q_L^*/\nu_L$ is the liquid Reynolds number based on the liquid flow rate per unit width q_L^* and liquid kinematic viscosity ν_L . Thus, the smaller ϕ , the more closely the instability threshold can be approached while maintaining an experimentally realizable film thickness $h_0^* = (3\text{Re}_L \nu_L^2 / g / \sin(\phi))^{1/3}$, where the subscript 0 denotes the primary flow and g the gravitational acceleration. Closer to the instability threshold, the interfacial dynamics are less complicated and surface waves are predominantly two-dimensional (Kofman *et al.* 2014).

Our current work is inspired by several recent findings reported in the literature, which we discuss next. Lavalle *et al.* (2019) demonstrated that the onset of the Kapitza instability can be significantly delayed at low inclination angles, by strongly confining the surrounding gas, as conjectured by Tilley *et al.* (1994). Moreover, they discovered that the gas-induced stabilization is strongest in the counter-current configuration, and increases with increasing magnitude of the gas flow rate. Kushnir *et al.* (2021) subsequently showed that stabilization also occurs in the case of a confined recirculating gas, i.e. when the net gas flow rate is zero. In the above three studies, the gas flow was considered laminar and the stabilization occurred

82 for strong confinement, i.e. $H^* \leq 5$ mm. As demonstrated by Lavalle *et al.* (2019), it is
 83 caused by the linear response of the interfacial tangential gas shear stress T_G to a perturbation
 84 of the liquid film thickness. Potentially, gas-induced stabilization may thus be achieved for
 85 weaker confinement if the gas flow is turbulent, as turbulence increases the magnitude of
 86 T_G . In the current manuscript, we have checked this hypothesis based on linear stability
 87 calculations. In particular, we find that the Kapitza instability can be fully suppressed by a
 88 turbulent counter-current gas flow for $H^* \sim 10$ mm, when the inclination angle is very small
 89 ($\phi \sim 1^\circ$). By *full suppression*, we mean that the falling liquid film becomes unconditionally
 90 stable to long-wave disturbances, i.e. for all Re_L . By contrast, at non-negligible inclination
 91 ($\phi \sim 5^\circ$), the linear gas-effect is destabilizing and the counter-current gas flow can render the
 92 liquid film unconditionally unstable to long-wave disturbances, as previously reported for
 93 laminar flow conditions (Trifonov 2017; Kushnir *et al.* 2021). We find that turbulence can
 94 significantly delay the onset of this unconditional instability.

95 Recent numerical (Lavalle *et al.* 2021) and experimental (Mergui *et al.* 2023) investiga-
 96 tions of weakly-inclined falling liquid films have shown that a strongly-confined laminar
 97 counter-current gas flow can attenuate the amplitude of nonlinear travelling-wave solutions
 98 (TWS), even though the linear gas-effect is destabilizing. In our current configuration, where
 99 the inclination angle is similar but the confinement is weaker and the gas flow is turbulent,
 100 both the TWS amplitude and the linear spatial growth rate increase with increasing counter-
 101 current gas flow rate, at least until the absolute instability (AI) limit is reached.

102 Several works on gas-sheared falling liquid films in narrow (vertical) channels have
 103 identified wave coalescence as a possible route toward flooding. For example, Drosos *et al.*
 104 (2006) measured the probability density function of the wave height and found that the
 105 dominant wave frequency strongly decreases as the flooding limit is approached. Later,
 106 Dietze & Ruyer-Quil (2013) computed the noise-driven spatial evolution of Kapitza waves
 107 sheared by a superconfined laminar gas flow and showed that coalescence can trigger an
 108 intermittent obstruction of the channel. Geometrical obstruction is not possible in our current
 109 configuration, where H^* , although smaller than the typical wavelength Λ^* , is much greater
 110 than h_0^* . Nonetheless, we find that the counter-current gas flow exacerbates coalescence
 111 events, entailing very large waves that form via the successive absorption of smaller waves.
 112 Such waves have been designated as tsunami waves (Meza & Balakotaiah 2008), and we
 113 will employ this term throughout. In particular, the onset of coalescence moves upstream
 114 significantly when the counter-current gas flow rate is increased, precipitating the usual wave
 115 coarsening dynamics observed in liquid films falling in a quiescent gas (Chang *et al.* 1996b).

116 The transition between convective instability (spatial growth) and absolute instability
 117 (temporal growth), which occurs when the counter-current gas flow rate is increased, has been
 118 suggested as another potential cause for the onset of flooding. For example, Vellingiri *et al.*
 119 (2015) showed that the AI limit predicted by their linear stability analysis lies not too far
 120 from the flooding threshold reported in the experiments of Zapke & Kröger (2000), where
 121 a vertically-falling liquid film was sheared by a counter-current gas flow. However, the
 122 trends of the two limits versus the liquid Reynolds number Re_L were opposed, i.e. the
 123 flooding onset, expressed in terms of the superficial gas velocity, increased with increasing
 124 Re_L , whereas the AI limit diminished. In the current work, we have thus explored the spatio-
 125 temporal evolution of nonlinear Kapitza waves beyond the AI limit, based on experiments and
 126 numerical computations. We find that AI is not necessarily dangerous in our configuration,
 127 i.e. no catastrophic events occur until far beyond the AI limit. Moreover, in the case of a
 128 noise-driven wave evolution scenario, AI can act as an effective linear selection mechanism,
 129 leading to a regular train of downward-travelling nonlinear surface waves, thus precluding
 130 dangerous coalescence events.

131 Lavalle *et al.* (2020) studied vertically-falling wavy liquid films sheared by a superconfined

132 laminar counter-current gas flow, and discovered an oscillatory secondary instability. This
133 instability entails a regular spatial modulation of TWS generated by coherent inlet forcing.
134 We have performed computations for the same liquid-side parameters, but with our moderate
135 confinement, i.e. $H^* \sim 10$ mm. Although we do not observe any oscillatory instability, wave
136 amplitude modulations occur nonetheless, albeit due to an entirely different mechanism,
137 which sets in beyond the AI limit. There, a competition between the forcing frequency and
138 the absolute frequency can lead to coalescence-induced tsunami waves that are separated by
139 a long and thin residual film, on which small-amplitude standing ripples form as a result of
140 AI. These ripples continually perturb the tsunami waves passing over them, similar to the
141 effect of wall corrugations (Dietze 2019).

142 Several numerical works have suggested that a counter-current gas flow may provoke
143 the reversal of nonlinear Kapitza waves, which can be viewed as another manifestation
144 of flooding. Tseluiko & Kalliadasis (2011) observed this for a vertically-falling liquid film
145 sheared by a weakly-confined turbulent gas flow. However, in their computations, the average
146 film thickness \bar{h} was fixed instead of the liquid flow rate, which is more representative of
147 a sudden gas flow rate increase in an experiment. Trifonov (2017) observed the reversal of
148 travelling Kapitza waves in the case of an inclined falling liquid film sheared by a laminar
149 gas flow. However, the gas Reynolds number in his computations was far greater than the
150 turbulence threshold, i.e. $|\text{Re}_G| > 10000$. Lavalle *et al.* (2020) observed wave reversal due to
151 a gas-induced secondary instability of TWS in the case of extreme confinement ($H^* \sim 1$ mm).
152 In our current configuration, where the liquid flow rate is imposed, the gas flow is turbulent,
153 and the confinement is moderate, we did not observe any reversal of Kapitza waves, neither
154 in terms of TWS nor in the case of spatially evolving waves.

155 In our experiments, flooding is triggered (far beyond the AI limit) by upward-travelling
156 short ripples that first coexist with the initial Kapitza waves and then overpower the latter.
157 As soon as these ripples appear, liquid, in the form of small droplets, starts to accumulate
158 in the gas loop, eventually forcing a shut-down of the experiment. Such ripples were first
159 observed in the experiments of Kofman *et al.* (2017). In the current manuscript, we elucidate
160 their origin, which has remained an open question.

161 Kofman *et al.* (2017) pointed out that the ripples observed in their experiments have
162 similar wavelengths and amplitudes than ripples forming in horizontal liquid films sheared
163 by an unconfined co-current turbulent gas flow (Özgen *et al.* 2002). Those ripples are
164 caused by a short-wave interfacial instability mode (Miesen & Boersma 1995). They have
165 also been observed when the co-current gas flow is confined, e.g. in the experiments
166 of Hanratty & Engen (1957), where $H^* = 25.4$ mm, and where the ripples were seen to
167 coalesce into fast-travelling slugs. The corresponding instability mode was identified by
168 McCready & Chang (1994). They showed that the dispersion curve of the linear temporal
169 growth rate kc_i , where k and c_i denote the wave number and complex celerity, originates at
170 $k=c_i=0$, and displays two unstable ($kc_i > 0$) humps, one at small and another at large k , the
171 short-wave hump being dominant. However, no short-wave instability mode has ever been
172 identified for falling liquid films sheared by a counter-current (turbulent) gas flow, despite
173 several previous linear stability investigations. And, the ripples observed in our experiments
174 move upstream, i.e. in opposite direction to the liquid.

175 Schmidt *et al.* (2016) applied the Chebyshev collocation approach (Orszag 1971;
176 Barmak *et al.* 2016a) to study this problem in the vertical configuration at $|\text{Re}_G| > 35000$,
177 where $\text{Re}_G = q_G^* / \nu_G$ designates the gas Reynolds number based on the gas flow rate per unit
178 width q_G^* and the gas kinematic viscosity ν_G . Although the gas flow under these conditions
179 would be turbulent in an experiment, the laminar Navier-Stokes equations were used. The
180 authors identified four instability modes: (1) the long-wave Kapitza mode (Brooke Benjamin
181 1957; Yih 1963), which is an interfacial mode; (2) the liquid-side short-wave Tollmien-

182 Schlichting mode (Floryan *et al.* 1987; Samanta 2020), which travels in the direction of
 183 the liquid and occurs at very large Re_L ; (3) the gas-side short-wave Tollmien-Schlichting
 184 mode; and (4) a so-called long-wave internal mode, which appears at $|Re_G| \sim 10 \times 10^4$ and
 185 can merge with the Kapitza mode. Trifonov (2017) applied the same approach to the case
 186 of an inclined falling liquid film, and showed that the gas-side Tollmien-Schlichting mode
 187 corresponds to the classical result for channel flow, i.e. $|Re_G| = \frac{4}{3} 5772 = 7696$ (Orszag 1971).
 188 This mode always travels in the direction of the gas flow, but it does not meaningfully perturb
 189 the liquid-gas interface. Thus, it cannot generate the upward-travelling ripples observed in
 190 our experiment, which, moreover, occur at $|Re_G| \sim 6000$.

191 The works of Schmidt *et al.* (2016) and Trifonov (2017) did not account for turbulence
 192 in the primary flow, even though the gas Reynolds number $|Re_G|$ was far greater than
 193 the experimental turbulence threshold $|Re_G| \sim 1800$ (Pope 2000). Following the seminal
 194 work of Náraigh *et al.* (2011), this shortcoming was remedied by Vellingiri *et al.* (2015),
 195 who represented the turbulent gas flow via the Reynolds averaged Navier-Stokes equations
 196 (RANS), using curvilinear coordinates and Prandtl's mixing-length approach. These authors
 197 observed a transition of the long-wave Kapitza instability from downward-convective to
 198 upward-convective upon increasing the counter-current gas flow rate q_{L0} . However, as the
 199 liquid film thickness h_0 and not q_{L0} was fixed in these calculations, upward-travelling waves
 200 were associated with $q_{L0} < 0$. By contrast, q_{L0} is fixed and positive in our experiments.
 201 Vellingiri *et al.* (2015) did not identify any short-wave instability mode. Nonetheless, they
 202 reported a non-monotonic variation of the cut-off wave number k_c upon increasing $|Re_G|$ for
 203 the long-wave instability mode, i.e. a decrease followed by an increase in k_c . Trifonov (2017)
 204 later made a similar observation. We will show that this behavior results from an interaction
 205 between the long-wave Kapitza instability mode and a new short-wave interfacial instability
 206 mode, which we have detected via temporal linear stability calculations at fixed $q_{L0} > 0$, using
 207 the Chebyshev collocation approach.

208 This new short-wave mode emerges around the AI limit of the long-wave Kapitza instability
 209 mode, upon increasing the counter-current gas flow rate. Initially, the long-wave and short-
 210 wave modes coexist, but, at sufficiently large $|Re_G|$, they merge to form a two-humped
 211 dispersion curve originating at $k=c_i=0$, and the short-wave maximum eventually becomes
 212 dominant. Linear waves corresponding to this maximum display a negative wave celerity
 213 $c_r < 0$, and both their wavelength Λ and c_r agree well with the upward-travelling ripples
 214 observed in our experiment. The wave celerity c_r of the new short-wave instability mode
 215 is always negative at the most-amplified wave number $k=k_{max}$, but it can change sign at
 216 lower k . This is a fundamental difference with the gas-side Tollmien-Schlichting mode.
 217 Conversely, when $c_r < 0$, the liquid film surface velocity is not necessarily negative. Thus,
 218 ripples travel upward, even when the liquid travels downward across the entire film thickness.
 219 This is a difference with the interfacial mode observed in co-current liquid/gas flows
 220 (Miesen & Boersma 1995).

221 Nonlinear computations in the current manuscript have been performed with a new low-
 222 dimensional model, which we introduce. Therein, the liquid film is represented via the
 223 weighted residual integral boundary layer (WRIBL) approach of Ruyer-Quil & Manneville
 224 (1998), leading to two coupled evolution equations for the local instantaneous film thickness
 225 h and liquid flow rate q_L . We develop these equations up to second order in the long-wave
 226 parameter, and account for the effect of an adjacent gas via the gas shear stress T_G and
 227 the gas pressure P_G , acting at the liquid-gas interface. Following Camassa *et al.* (2017), we
 228 obtain these coupling quantities from a first-order long-wave (LW) approximation of the
 229 gas-side RANS equations written in curvilinear coordinates (Thorsness *et al.* 1978), while
 230 assuming a frozen liquid-gas interface. Our thus obtained WRIBL-LW model represents
 231 several improvements w.r.t. previous works, which we will discuss next.

232 Demekhin (1981) used the IBL approach of Shkadov (1967) to model the liquid film, and
233 accounted for the effect of a turbulent gas flow, via T_G and P_G , through the linear response of
234 the gas-side RANS equations to a waviness of the liquid-gas interface (assumed frozen). This
235 linearized approach is valid in the limit $h/H \ll 1$, i.e. assuming a large channel height versus
236 the film thickness. Further, the authors invoked the quasi-laminar assumption (Miles 1957;
237 Brooke Benjamin 1959), where turbulence enters only via the unperturbed flow and linear
238 perturbations of the Reynolds stresses are neglected, which is usually valid in gas-sheared
239 wavy liquid films (Náraigh *et al.* 2011). However, the liquid-side IBL approach is known to
240 significantly over-predict the instability threshold of an inclined falling liquid film.

241 Tseluiko & Kalliadasis (2011) remedied this shortcoming by combining the gas-side
242 description of Demekhin (1981) with a WRIBL representation of the liquid film. However,
243 their liquid-side WRIBL model was developed only up to first order in the long-wave
244 parameter, and, thus, in conjunction with the linear gas-side approach, the gas pressure P_G
245 did not enter the problem. We will show that this changes the linear response of the liquid film
246 qualitatively in our configuration, and that a second-order liquid-side WRIBL development,
247 accounting for P_G , is needed to accurately capture the effect of the counter-current gas flow.

248 Such a liquid-side treatment was applied by Samanta (2014), but the author made several
249 simplifications in the gas-side description, i.e. P_G was neglected altogether, and T_G was
250 assumed constant. The latter assumption entails that the gas-induced stabilization observed
251 in superconfined falling liquid films (Lavalle *et al.* 2019), which relies on the linear response
252 of T_G , cannot be captured.

253 Camassa *et al.* (2017) accounted for variations in P_G and T_G in their gas-side description.
254 Moreover, their gas-side description relies on a long-wave rather than a low-amplitude
255 expansion of the RANS equations, and, thus, finite confinement levels can be studied.
256 However, their description of the liquid film relied on the lubrication approach. Thus, the
257 inertia-driven Kapitza instability, which is responsible for generating long waves in our
258 configuration but was irrelevant in theirs, cannot be captured.

259 By coupling the gas-side approach of Camassa *et al.* (2017) with a second-order WRIBL
260 description of the liquid film, our WRIBL-LW model remedies the different limitations
261 discussed above. Our model is aimed at moderate confinement levels, where the gas flow
262 is turbulent and the gas pressure is relevant. In that sense, it complements the model
263 of Dietze & Ruyer-Quil (2013), for superconfined laminar liquid-gas flows, and those of
264 Demekhin (1981) and Tseluiko & Kalliadasis (2011), for weakly-confined falling liquid films
265 sheared by a turbulent gas flow, where the effect of P_G is negligible. For completeness, we
266 point out that our model does not rely on the quasi-laminar assumption (Alekseenko *et al.*
267 2009; Trifonov 2010a; Tseluiko & Kalliadasis 2011; Vellingiri *et al.* 2015). We will show
268 that it accurately predicts the dynamics of Kapitza waves under the effect of a counter-current
269 turbulent gas flow, in good agreement with experiments.

270 Our manuscript is structured as follows. In §2, we introduce our experimental setup
271 for studying surface waves in gas-sheared falling liquid films. In §3, we present our low-
272 dimensional WRIBL-LW model (subsections 3.1 and 3.2), and the numerical methods
273 underlying our linear and nonlinear computations therewith (subsection 3.4). Section 4
274 concerns linear stability calculations based on the full RANS equations in the gas, where
275 the liquid-side description is based either on the WRIBL model (subsection 4.1) or on the
276 full Navier-Stokes equations (subsection 4.2). Section 6 presents our results concerning the
277 gas-effect on linear and nonlinear wave dynamics. We first focus on waves resulting from
278 the long-wave Kapitza instability (subsection 6.1), and then discuss upward-travelling short-
279 wave ripples (subsection 6.2). Conclusions are drawn in §7, followed by appendices A and
280 B, containing validation results.

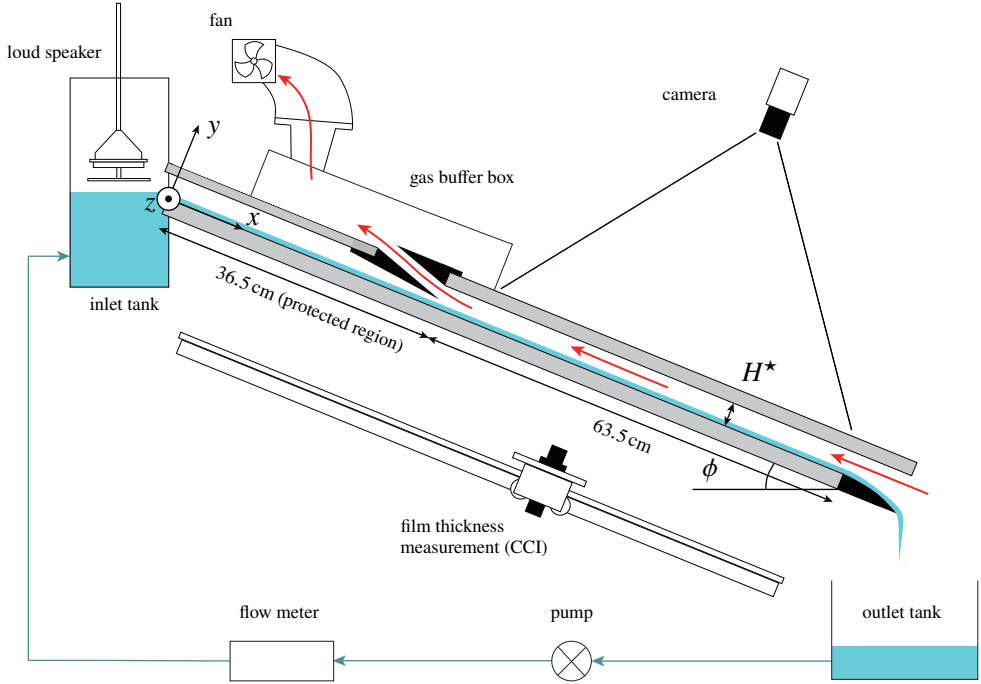


Figure 1: Sketch of our experimental setup. A falling liquid film of water flows down a glass plate inclined at an angle $\phi=5^\circ$ and enters in contact with a counter-current turbulent air flow within a rectangular channel of height $H^*=13$ mm and width $W^*=27$ mm. A loudspeaker is used to force Kapitzka waves on the surface of the liquid film, which grow and saturate within a protected region of the setup.

281 2. Experiments

282 Figure 1 sketches the setup used for our experiments. A liquid film (index L) of water flows
 283 down a glass plate inclined at $\phi=5^\circ$, and enters into contact with a counter-current turbulent
 284 gas flow (index G) of air confined within a rectangular channel of height $H^*=13$ mm and
 285 width $W^*=27$ mm. This setup is a slightly modified version of the setup used in the work of
 286 Mergui *et al.* (2023), where $H^*=5$ mm and the gas flow was laminar.

287 The liquid flow rate q_L^* is controlled through a gear pump and measured with an error of
 288 $\pm 3\%$ using a conductance flow meter (IFM electronic, SM6000). In the current manuscript,
 289 we focus on two liquid-side regimes: $Re_L \sim 33$ and $Re_L \sim 45$. A loudspeaker integrated into
 290 the upstream liquid reservoir enables the forcing of Kapitzka waves with prescribed frequency
 291 f_0^* on the surface of the liquid film. These waves are allowed to grow and saturate within a
 292 protected region spanning from $x^*=0$ to $x^*=36.5$ cm, before entering the gas-sheared
 293 section of the setup ($36.5 \text{ cm} \leq x^* \leq 100 \text{ cm}$). In our experiments, f_0^* is chosen such as to maximize
 294 the linear growth rate of the Kapitzka waves, yielding a train of regular waves within the
 295 protected region. Also, the forcing amplitude is adjusted so that the waves reach a saturated
 296 amplitude before entering the gas-sheared section.

297 The gas flow rate q_G^* is controlled through a fan, and quantified via a calibration curve
 298 (relating the fan power to q_G^*) obtained from gas velocity measurements in the dry channel.
 299 Details of the procedure are given in Mergui *et al.* (2023). An error on Re_G of 3% was
 300 estimated for all our experiments. For a given liquid flow rate, the fan power was varied from
 301 zero up until breakdown of the experiment due to flooding, when liquid droplets accumulated
 302 in the gas buffer box. At zero fan power, the gas is subject to an aerostatic pressure drop,

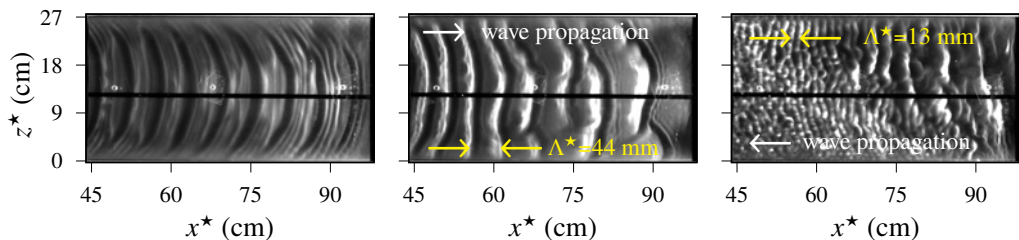


Figure 2: Transition of the wavy falling liquid film under a counter-current gas flow: water/air, $Re_L^{as}=44.7$, $Re_L=43.1$, $f_0^*=3$ Hz. Shadowgraphs of the liquid-gas interface for increasingly strong fan power. Left: zero fan power (aerostatic configuration), regularly-spaced Kapitza waves; middle: $Re_G=-5830$, coalescence of Kapitza waves; right: $Re_G=-6760$, coexistence of Kapitza waves with upward-travelling short ripples.

303 which is imposed by the quiescent ambient air. In this case, which we will designate as
 304 *aerostatic configuration*, the gas flows downward under the shearing action of the falling
 305 liquid film, i.e. $q_G^* > 0$. Conversely, in the case of a counter-current gas flow, we have $q_G^* < 0$.
 306 Thus, we consider q_G^* , and the gas Reynolds number Re_G , as signed quantities.

307 In our counter-current experimental runs, Re_G was typically varied from $Re_G=-3000$ to
 308 $Re_G=-6800$, after an initial measurement under aerostatic conditions. Due to evaporation, the
 309 liquid temperature typically decreased by a few Kelvin between the aerostatic and counter-
 310 current configurations. As q_L^* remained fixed during each run, a corresponding variation of
 311 Re_L occurred due to changes in the fluid properties. To account for this, we have monitored
 312 the liquid temperature T_{inlet} in the inlet tank over the course of each experiment, using a
 313 thermocouple. The temperature decrease was observed as soon as the counter-current air
 314 flow was imposed, but the temperature varied little upon increasing the gas flow rate after
 315 that. Thus, when reporting experimental data, we will give Re_L^{as} , which corresponds to the
 316 aerostatic configuration, and Re_L , which corresponds to the counter-current configuration.

317 Representative values of the density and kinematic viscosity of water and air for our
 318 counter-current experiments ($T_{inlet} \approx 19^\circ\text{C}$) are $\rho_L=998.3$ kg/m³, $\nu_L=1.03 \times 10^{-6}$ m²/s, and
 319 $\rho_G=1.21$ kg/m³, $\nu_G=14.9 \times 10^{-6}$ m²/s. The surface tension of our water was measured once
 320 and for all at $T=19.9^\circ\text{C}$ with a Drop Shape Analyzer (Krüss), yielding $\sigma=71$ mN m⁻¹. Based
 321 on this, we obtain $Ka=\sigma/\rho_L/\nu_L^{4/3}/g^{1/3}=3174$ for the Kapitza number. Conversely, for our
 322 experiments in the aerostatic configuration ($T_{inlet} \approx 21^\circ\text{C}$), we obtain $Ka=3394$.

323 Two methods were applied to characterize the gas-effect on the dynamics of nonlinear sur-
 324 face waves (see Kofman *et al.* (2014) and Mergui *et al.* (2023) for details): (1) shadowgraphy
 325 of the wavy liquid-gas interface, using an sCMOS camera (PCO, pco.edge 5.5) with 100 Hz
 326 framerate; (2) pointwise measurements of the film thickness time trace, using a confocal
 327 chromatic imaging (CCI) technique (Cohen-Sabban *et al.* 2001; Lel *et al.* 2005) with 400 Hz
 328 acquisition frequency and an accuracy of ± 1 μm (Stil S.A., CL-MG CL4 line sensor).

329 Figures 2 and 3 show typical data obtained with these two methods. Figure 2 represents
 330 shadowgraphs for an experiment, where the fan power was increased step by step (from left
 331 to right panel), while maintaining q_L^* and $f_0^*=3$ Hz fixed. Each shadowgraph represents the
 332 entire width of the channel and almost the entire length of the gas-sheared section of the setup,
 333 i.e. $44\text{ cm} \leq x^* \leq 100\text{ cm}$. At zero fan power (leftmost panel), regularly-spaced Kapitza waves
 334 with quasi-two-dimensional wave fronts are observed. Applying and increasing a counter-
 335 current gas flow rate, first causes coalescence events (middle panel), and then the emergence
 336 of upward-travelling short ripples that coexist with the long Kapitza waves (rightmost panel).
 337 This dynamics will be the focus of section 6.

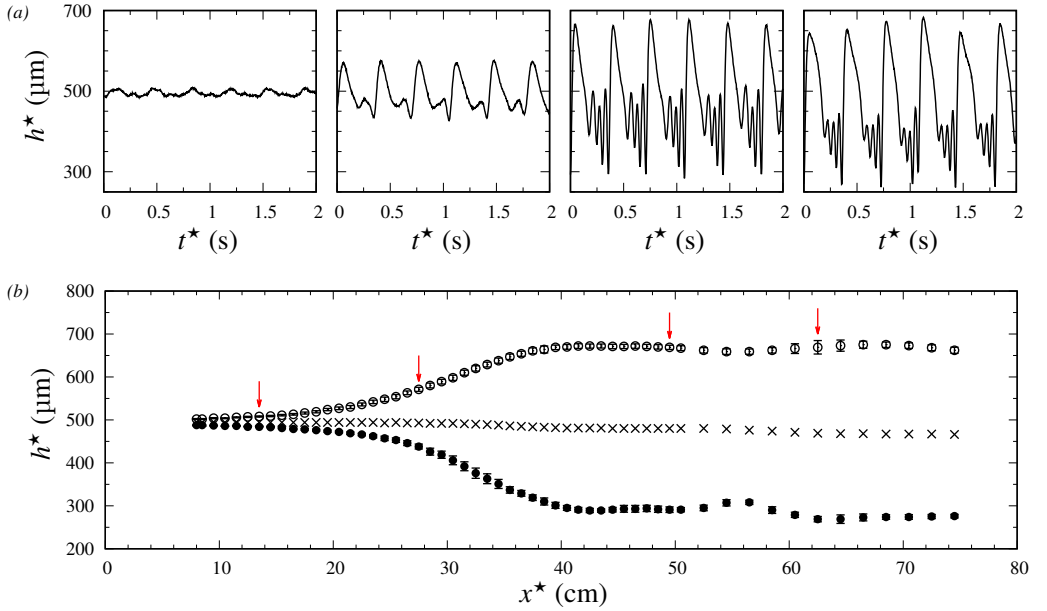


Figure 3: Typical CCI film thickness measurements in the aerostatic configuration: water/air, $Re_L^{as}=33.7$, $f_0^*=2.8$ Hz. (a) Film thickness time traces measured at different positions. From left to right: $x^*=13.5$ cm, 27.5 cm, 49.5 cm, and 62.5 cm; (b) spatial profiles of averaged quantities (at least 100 waves). Open/filled circles: ensemble-averaged wave height h_{max}^* and minimum film thickness h_{min}^* , crosses: time-averaged film thickness \bar{h}^* . Error bars indicate standard deviation and red arrows mark positions for panel a.

338 Figure 3 represents measurement data obtained with the CCI technique for the aerostatic
 339 configuration at $Re_L^{as}=33.7$ and $f_0^*=2.8$ Hz. In panel 3a, we have plotted time traces of the
 340 film thickness h^* at streamwise positions representative for the regimes of linear growth,
 341 nonlinear growth, and saturation of Kapitza waves. These time traces evidence the formation
 342 of characteristic precursory capillary ripples. Panel 3b represents spatial profiles of the
 343 ensemble-averaged (over at least 100 waves) maximum film thickness h_{max}^* , minimum film
 344 thickness h_{min}^* , and time-averaged (over at least 100 wave periods) film thickness \bar{h}^* . Error
 345 bars illustrate the standard deviation. To obtain these profiles, the CCI probe was displaced
 346 incrementally using a rail (figure 1).

347 3. Low-dimensional WRIBL-LW model

348 We consider the flow in figure 4. A two-dimensional laminar falling liquid film of thickness
 349 $h(x, t)$ flows along an inclined plane under the action of gravity, while being sheared by a
 350 counter-current turbulent gas flow. The gas flow is confined by a second wall at $y^*=H^*$ (the
 351 star superscript denotes dimensional quantities throughout), which is not represented. We
 352 impose a symmetry condition at the center line of the average gas layer, i.e. $y^*=D^*$. In the
 353 case of a symmetrical vertical configuration with liquid films lining both walls (Vlachos *et al.*
 354 2001), this condition is satisfied analytically, and we have $D^*=H^*/2$. In the case of an
 355 inclined configuration with a dry upper wall, which is the one considered here, the symmetry
 356 condition remains a reasonable approximation, provided the liquid holdup \bar{h}^*/H^* , where
 357 \bar{h}^* designates the average film thickness, is not too large. In the current work, $\bar{h}^*/H^*<0.1$,
 358 and thus the symmetry condition is acceptable. In that case, $D^*=(H^*+\bar{h}^*)/2$. Moreover, due

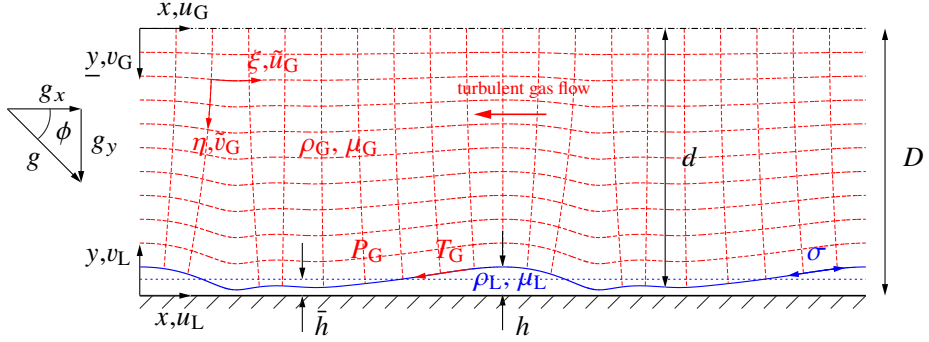


Figure 4: Falling liquid film (subscript L) on an inclined wall subject to a counter-current turbulent gas flow (subscript G). The flow is confined by an upper wall (not shown) at $y^*=H^*$ (stars denote dimensional quantities) and a symmetry condition is imposed at the center line of the average gas layer $y^*=D^*$. Gas-liquid coupling is expressed via the tangential gas shear stress T_G and the gas pressure P_G at the film surface $y^*=h^*$. Red dashed lines illustrate orthogonal curvilinear coordinate system (η, ξ) , where $\eta=y\bar{d}/d$.

359 to the inter-phase coupling conditions we will apply in our gas-side description (frozen-
 360 interface assumption) and the nature of our calculations (linear stability analysis and long-
 361 wave asymptotic expansion), the symmetry condition at $y^*=D^*$ holds analytically, even when
 362 the upper wall is dry. This will be further explained in sections 3.2 and 4.1.

363 Following previous works (Halpern & Grotberg 2003; Tseluiko & Kalliadasis 2011;
 364 Samanta 2014; Camassa *et al.* 2017), we relax the inter-phase coupling conditions and apply
 365 a weakly-coupled treatment of the two-phase flow. The liquid film (section 3.1) is modelled
 366 with the WRIBL method (Kalliadasis *et al.* 2012), where the effect of the gas enters via the
 367 tangential gas shear stress T_G and the gas pressure P_G acting at the film surface $y^*=h^*$ (figure
 368 4), neglecting the normal gaseous viscous stress. These inter-phase coupling quantities
 369 are obtained from the gas-side model (section 3.2), which is derived via long-wave (LW)
 370 asymptotic expansion, following Camassa *et al.* (2017).

371 3.1. Liquid-side WRIBL model

372 The liquid film (subscript L), with density ρ_L , dynamic viscosity μ_L , and surface tension σ ,
 373 is governed by the dimensionless continuity and Navier-Stokes equations written in Cartesian
 374 coordinates x and y (figure 4):

$$375 \quad \partial_x u_L + \partial_y v_L = 0, \quad (3.1a)$$

$$377 \quad \epsilon(\partial_t u_L + u_L \partial_x u_L + v_L \partial_y u_L) = -\epsilon \partial_x p + \frac{1}{\text{Re}_L} (\epsilon^2 \partial_{xx} u_L + \partial_{yy} u_L) + \frac{\sin(\phi)}{\text{Fr}^2}, \quad (3.1b)$$

$$379 \quad \epsilon^3(\partial_t v_L + u_L \partial_x v_L + v_L \partial_y v_L) = -\epsilon \partial_y p_L + \frac{1}{\text{Re}_L} (\epsilon^4 \partial_{xx} v_L + \epsilon^2 \partial_{yy} v_L) - \epsilon \frac{\cos(\phi)}{\text{Fr}^2}, \quad (3.1c)$$

380 where $\text{Re}_L = \rho_L \mathcal{U}_L \mathcal{L} / \mu_L$ and $\text{Fr} = \mathcal{U}_L / \sqrt{\mathcal{L}g}$ denote the liquid Reynolds number and Froude
 381 number, and where we have applied the following scaling:

$$382 \quad u_L = \frac{u_L^*}{\mathcal{U}_L}, \quad v_L = \frac{v_L^*}{\epsilon \mathcal{U}_L}, \quad x = \epsilon \frac{x^*}{\mathcal{L}}, \quad y = \frac{y^*}{\mathcal{L}}, \quad t = \epsilon t^* \frac{\mathcal{U}_L}{\mathcal{L}}, \quad p_L = \frac{p_L^*}{\rho_L \mathcal{U}_L^2}. \quad (3.1d)$$

383 Here, we have introduced the long-wave parameter $\epsilon = \mathcal{L} / \Lambda^*$, which relates the cross-stream
 384 length scale \mathcal{L} to the streamwise length scale given by the wavelength Λ^* . For the purpose
 385 of the current derivation, it suffices to say that the scales \mathcal{L} and \mathcal{U}_L are representative of

386 the film thickness h^* and streamwise liquid velocity u_L^* . In section 3.3, we will rescale our
387 problem and make the final choice for \mathcal{L} and \mathcal{U}_L .

388 The system is closed with the boundary conditions at $y=0$:

$$389 \quad u_L = v_L = 0, \quad (3.1e)$$

390 the kinematic condition:

$$391 \quad v_L|_{y=h} = u_L|_{y=h} \partial_x h + \partial_t h, \quad (3.1f)$$

392 and the inter-phase stress coupling conditions at $y=h$:

$$393 \quad -\partial_y u_L \frac{1}{1 + \epsilon^2 \partial_x h^2} (-\epsilon^4 \partial_x h^2 \partial_x v_L - 4\epsilon^2 \partial_x h \partial_x u_L + \epsilon^2 \partial_x v_L) = \frac{\Pi_\mu \Pi_u}{\Pi_L} T_G, \quad (3.1g)$$

395

$$396 \quad \epsilon P_L + \frac{2}{1 + \epsilon^2 \partial_x h^2} \frac{1}{\text{Re}_L} (\epsilon^4 \partial_x h^2 \partial_x u_L - \epsilon^4 \partial_x h \partial_x v_L - \epsilon^2 \partial_x u_L - \epsilon^2 \partial_x h \partial_y u_L) \\ - \epsilon^3 \text{We} \partial_{xx} h = \frac{1}{\text{Re}_G} \frac{\Pi_\rho \Pi_u^2}{\Pi_L} P_G, \quad (3.1h)$$

397 where $\text{We} = \sigma / \rho_L / \mathcal{L} / \mathcal{U}_L^2$ denotes the Weber number. The liquid-gas coupling enters through
398 T_G and P_G , which are scaled as follows:

$$399 \quad T_G = \frac{\mathcal{L}_G}{\mu_G \mathcal{U}_G} T_G^*, \quad P_G = \frac{\epsilon}{\mu_G \mathcal{U}_G} P_G^*, \quad (3.2)$$

400 where \mathcal{L}_G , \mathcal{U}_G , and $\epsilon = \mathcal{L}_G / \Lambda^* = \epsilon \Pi_L$ denote the gas-side cross-stream length scale, velocity
401 scale, and long-wave parameter, which will be defined in section 3.2. As a result, the gas
402 Reynolds number $\text{Re}_G = \rho_G \mathcal{U}_G \mathcal{L}_G / \mu_G$, the velocity scale ratio $\Pi_u = \mathcal{U}_G / \mathcal{U}_L$, the length scale
403 ratio $\Pi_L = \mathcal{L}_G / \mathcal{L}$, and the viscosity and density ratios $\Pi_\mu = \mu_G / \mu_L$ and $\Pi_\rho = \rho_G / \rho_L$ enter (3.1g)
404 and (3.1h).

405 Next, we apply the WRIBL approach to derive two evolution equations involving the local
406 instantaneous liquid flow rate $q(x, t)$ and the film thickness $h(x, t)$. In principle, we follow
407 the same steps as Samanta (2014), only that we account for the gas pressure P_G , which plays
408 an important role in our current configuration, allow P_G and T_G to vary in space and time,
409 and account for turbulence in the gas.

410 First, the governing equations (3.1) are truncated at $\mathcal{O}(\epsilon^2)$, except for inertial terms, which
411 are truncated at $\mathcal{O}(\text{Re}_L \epsilon)$. Next, we eliminate p from (3.1b) via an integrated form of (3.1c)
412 using (3.1h). Then, we substitute for the streamwise velocity u (v is obtained from equation
413 3.1a) the following decomposition:

$$414 \quad u_L = \hat{u}_L + \epsilon u_L^{(1)}, \quad (3.3)$$

415 where the base profile \hat{u}_L is governed by:

$$416 \quad \partial_{yy} \hat{u}_L = \text{const.}, \quad \partial_y \hat{u}_L|_{y=h} = \frac{\Pi_\mu \Pi_u}{\Pi_L} T_G, \quad \hat{u}_L|_{y=0} = 0, \quad (3.4) \\ \int_0^{h(x,t)} \hat{u}_L dy = q_L(x, t).$$

417 Finally, the unknown $\mathcal{O}(\epsilon)$ velocity correction $\epsilon u_L^{(1)}$ is eliminated from the problem by
418 multiplying the truncated form of (3.1b) with a weight function $w(y)$, integrating the result
419 across the film thickness $h(x, t)$, and applying the tangential inter-phase coupling condition

420 (3.1g). The weight function w satisfies:

$$421 \quad \partial_{yy}w = \text{const.}, \quad w|_{y=0} = 0, \quad \partial_y w|_{y=h} = 0. \quad (3.5)$$

423 As a final result, we obtain the integral momentum equation for the liquid film:

$$\begin{aligned}
 \partial_t q_L + \frac{17}{7} \frac{q_L}{h} \partial_x q_L - \frac{9}{7} \frac{q_L^2}{h^2} \partial_x h &= \frac{5}{6} \text{We} h \partial_{xxx} h + \frac{5}{6} \text{Fr}^{-2} h \{ \sin(\phi) - \cos(\phi) \partial_x h \} \\
 &+ \text{Re}_L^{-1} \left\{ -\frac{5}{2} \frac{q_L}{h^2} + 4 \frac{q_L}{h^2} \partial_x h^2 - \frac{9}{2h} \partial_x q_L \partial_x h - 6 \frac{q_L}{h} \partial_{xx} h + \frac{9}{2} \partial_{xx} q_L \right\} \\
 &+ \frac{\Pi_\mu \Pi_u}{\Pi_L} T_G \left\{ \text{Re}_L^{-1} \left[\frac{5}{4} + \frac{h}{6} \partial_{xx} h + \frac{1}{2} \partial_x h^2 \right] - \frac{5}{112} q_L \partial_x h - \frac{19}{336} \partial_x q_L h \right\} \\
 &- \frac{19}{672} \frac{\Pi_\mu^2 \Pi_u^2}{\Pi_L^2} h^2 \partial_x h T_G^2 - \frac{5}{6} \text{Re}_G^{-1} \frac{\Pi_\rho \Pi_u^2}{\Pi_L} h \partial_x P_G \\
 &+ \frac{\Pi_\mu \Pi_u}{\Pi_L} \left\{ \partial_x T_G \left[\text{Re}_L^{-1} \frac{3}{4} h \partial_x h - \frac{15}{224} h q_L \right] - \frac{25}{1344} \frac{\Pi_\mu \Pi_u}{\Pi_L} h^3 T_G \partial_x T_G - \frac{h^2}{48} \partial_t T_G \right\}, \quad (3.6a)
 \end{aligned}$$

425 to which is added an integral continuity equation obtained by integrating (3.1a) across the
 426 liquid film and applying (3.1f):

$$427 \quad \partial_t h + \partial_x q_L = 0. \quad (3.6b)$$

428 In the limit $T_G = \partial_x P_G = 0$, (3.6a) reduces to equation (41) from Ruyer-Quil & Manneville
 429 (2000). In the limit $\partial_x T_G = \partial_t T_G = \partial_x P_G = 0$, it collapses with equation (3.9) from Samanta
 430 (2014), except for a typo in the $T_G \partial_x h^2$ term of that reference. Here, we will neglect the terms
 431 involving $\partial_x T_G$ and $\partial_t T_G$, but we will account for the space and time variation of $T_G(x, t)$ and
 432 $P_G(x, t)$ in the remaining terms. This amounts to a quasi-developed approach. **See appendix**
 433 **C for a justification of this approximation.**

434 Versus the model of Tseluiko & Kalliadasis (2011), which is based on a linear repre-
 435 sentation of the gas response, our model accounts for the gas pressure P_G , which plays a
 436 role for the confinement considered here. It also accounts for streamwise viscous diffusion
 437 in the liquid, which is known to affect the dynamics of precursory capillary ripples
 438 (Ruyer-Quil & Manneville 2002).

439 3.2. Gas-side asymptotic long-wave (LW) model

440 We represent the turbulent flow of the gas (subscript G), with density ρ_G and dynamic
 441 viscosity μ_G , in two dimensions via the (dimensionless) Reynolds-averaged continuity and
 442 steady Navier-Stokes (RANS) equations, written here in the Cartesian gas-side coordinates
 443 x and \underline{y} (see figure 4):

$$444 \quad \partial_x u_G + \partial_{\underline{y}} v_G = 0, \quad (3.7)$$

$$\begin{aligned}
 446 \quad \underline{\epsilon} (u_G \partial_x u_G + v_G \partial_{\underline{y}} u_G) &= -\frac{1}{\text{Re}_G} \partial_x P_G + \frac{\Pi_L}{\Pi_u^2} \frac{\sin(\phi)}{\text{Fr}^2} + \frac{1}{\text{Re}_G} \left\{ \partial_{\underline{y}\underline{y}} u_G + \underline{\epsilon}^2 \partial_{xx} u_G \right\} \\
 447 \quad &+ \frac{1}{\text{Re}_G} \left\{ \partial_{\underline{y}} \left(\frac{\mu_t}{\mu_G} \partial_{\underline{y}} u_G \right) + \underline{\epsilon}^2 \partial_x \left(\frac{\mu_t}{\mu_G} \partial_x u_G \right) \right\}, \quad (3.8a)
 \end{aligned}$$

$$\begin{aligned}
 448 \quad \underline{\epsilon}^3 (u_G \partial_x v_G + v_G \partial_y v_G) = & - \frac{1}{\text{Re}_G} \partial_y p_G + \underline{\epsilon} \frac{\Pi_L \cos(\phi)}{\Pi_u^2 \text{Fr}^2} + \frac{1}{\text{Re}_G} \left\{ \underline{\epsilon}^2 \partial_{yy} v_G + \underline{\epsilon}^4 \partial_{xx} v_G \right\} \quad (3.8b) \\
 449 \quad & + \frac{1}{\text{Re}_G} \left\{ \underline{\epsilon}^2 \partial_y \left(\frac{\mu_t}{\mu_G} \partial_y v_G \right) + \underline{\epsilon}^4 \partial_x \left(\frac{\mu_t}{\mu_G} \partial_x v_G \right) \right\}, \\
 450
 \end{aligned}$$

451 where μ_t denotes the turbulent viscosity, $\text{Re}_G = \rho_G \mathcal{U}_G \mathcal{L}_G / \mu_G$ is the gas Reynolds number,
 452 and where we have applied the following scaling:

$$453 \quad u_G = \frac{u_G^*}{\mathcal{U}_G}, \quad v_G = \frac{v_G^*}{\underline{\epsilon} \mathcal{U}_G}, \quad x = \underline{\epsilon} \frac{x^*}{\mathcal{L}_G}, \quad y = \frac{y^*}{\mathcal{L}_G}, \quad p_G = p_G^* \frac{\underline{\epsilon} \mathcal{L}_G}{\mu_G \mathcal{U}_G}, \quad (3.9)$$

454 introducing the gas-side long-wave parameter $\underline{\epsilon} = \mathcal{L}_G / \Lambda^*$. For the gas-side reference scales,
 455 we choose once and for all:

$$456 \quad \mathcal{L}_G = H^*, \quad \mathcal{U}_G = \frac{q_{G0}^*}{H^*}, \quad (3.10)$$

457 where q_{G0}^* is the nominal gas flow rate per unit width of the primary flow (subscript 0), and,
 458 thus, \mathcal{U}_G corresponds to the superficial gas velocity. We have scaled pressure with a measure
 459 for the viscous shear stress, in contrast to (3.1d), where the dynamic pressure was used.

460 The turbulent viscosity μ_t is formulated via the mixing-length approach (Prandtl 1925):

$$461 \quad \frac{\mu_t}{\mu_G} = \text{Re}_G l_t^2 \left| \partial_y u_G \right|, \quad (3.11)$$

462 where $l_t = l_t^* / \mathcal{L}_G$ denotes the dimensionless mixing length. At this point, a remark about
 463 choosing a turbulent viscosity model, such as (3.11), is in order. Luchini & Charru (2019)
 464 have shown that such models cannot fully reproduce the momentum redistribution induced
 465 by wall perturbations to a parallel turbulent flow. Nonetheless, comparisons with different
 466 experiments (Zilker *et al.* 1977; Frederick & Hanratty 1988) have shown that turbulent-
 467 viscosity models based on the van Driest equation, which will be introduced in (3.22), capture
 468 satisfactorily the linear (Russo & Luchini 2016) and nonlinear (Tseluiko & Kalliadasis 2011;
 469 Camassa *et al.* 2017) responses of the wall shear stress. Thus, such models allow to adequately
 470 account for the inter-phase coupling in our current configuration.

471 We assume a large gas/liquid velocity contrast $\Pi_u \gg 1$, which warrants two simplifications.
 472 First, we have neglected time derivatives in (3.8), as:

$$473 \quad O \left\{ \frac{\partial_t u_G^*}{u_G^* \partial_x u_G^*} \right\} = \frac{1}{\Pi_u} \ll 1, \quad (3.12)$$

474 assuming that the time scale is dictated by the waviness of the liquid film, i.e. $\mathcal{T} = \Lambda^* / \mathcal{U}_L$.
 475 Second, we set zero-velocity conditions at the film surface $y=d$:

$$476 \quad u_G = v_G = 0. \quad (3.13a)$$

477 Thus, from the point of view of the gas, the film surface is represented as a frozen wavy wall
 478 (Tseluiko & Kalliadasis 2011). Our system is closed via a symmetry condition at $y=0$:

$$479 \quad \partial_y u_G = v_G = 0. \quad (3.13b)$$

480 The ultimate aim of the gas-side model, to be derived next, is to obtain the inter-phase
 481 coupling quantities in (3.6a), which are evaluated at $y=d$, implying $l_t=0$:

$$482 \quad P_G = p_G, \quad (3.14a)$$

484

$$T_G = \frac{T_G^*}{\mu_G \mathcal{U}_G / \mathcal{L}_G} = -\partial_{\underline{y}} u_G - \{\epsilon^2 \partial_x d^2 - 1\}^{-1} \left\{ 2\epsilon^2 \partial_x d \partial_{\underline{y}} v_G \right. \\ \left. + 2\epsilon^2 \partial_x d \partial_x u_G + \epsilon^2 \partial_x v_G - \epsilon^4 \partial_x d^2 \partial_x v_G \right\}. \quad (3.14b)$$

486

487

Following Camassa *et al.* (2017), we introduce the curvilinear coordinates η and ξ (see figure 4), which will facilitate the account of turbulence:

488

$$\eta = \frac{\bar{d}}{d} y, \quad \xi = x + \underline{\epsilon} F(\xi, \eta), \quad (3.15)$$

489

where \bar{d} denotes the spatial average of d , and where orthogonality implies:

490

$$\partial_\eta F = \underline{\epsilon} \frac{d}{\bar{d}^2} \partial_\xi d \frac{1}{\underline{\epsilon} \partial_\xi F - 1}. \quad (3.16)$$

491

Red dashed lines in figure 4 represent curves of constant η and ξ , where:

492

$$\partial_x y \Big|_\eta = -\partial_y x \Big|_\xi = \frac{y}{\bar{d}} \partial_x d. \quad (3.17)$$

493

494

Next, we recast the governing equations (3.8) and (3.13) in the curvilinear coordinate system (tilde symbol), using the projection rules:

495

$$u_G = \tilde{u}_G + \mathcal{O}(\underline{\epsilon}^2), \quad v_G = \tilde{v}_G + \frac{\partial_\xi d}{\bar{d}} \eta \tilde{u}_G + \mathcal{O}(\underline{\epsilon}), \quad (3.18)$$

496

$$\partial_x = \partial_\xi - \eta \frac{\partial_\xi d}{\bar{d}} \partial_\eta + \mathcal{O}(\underline{\epsilon}), \quad \partial_y = \frac{\bar{d}}{d} \partial_\eta + \mathcal{O}(\underline{\epsilon}^2), \quad (3.19)$$

497

498

and truncate the result at $\mathcal{O}(\underline{\epsilon}^1)$. Upon eliminating the pressure variable p in (3.8a) via an appropriate integration of (3.8b), we obtain:

499

$$\frac{\partial_\xi d}{\bar{d}} \partial_\xi \tilde{u}_G + \partial_\xi \tilde{u}_G + \frac{\bar{d}}{d} \partial_\eta \tilde{v}_G = 0, \quad (3.20a)$$

501

$$\underline{\epsilon} \tilde{u}_G \partial_\xi \tilde{u}_G + \underline{\epsilon} \frac{\bar{d}}{d} \tilde{v}_G \partial_\eta \tilde{u}_G = -\frac{1}{\text{Re}_G} \partial_\xi P_G + \frac{\Pi_L}{\Pi_u^2} \frac{1}{\text{Fr}^2} (\sin(\phi) + \underline{\epsilon} \cos(\phi) \partial_\xi d) \\ + \frac{1}{\text{Re}_G} \frac{\bar{d}^2}{d^2} \left\{ \partial_{\eta\eta} \tilde{u}_G + \partial_\eta \left[\frac{\tilde{\mu}_t}{\mu_G} \partial_\eta \tilde{u}_G \right] \right\}, \quad (3.20b)$$

502

503

where $P_G = p_G|_{\eta=\bar{d}}$, and $\tilde{\mu}_t$ satisfies:

504

$$\frac{\tilde{\mu}_t}{\mu_G} = \frac{d}{\bar{d}} \text{Re}_G \tilde{l}_t^2 |\partial_\eta \tilde{u}_G|, \quad (3.21)$$

505

with $\tilde{l}_t = l_t \bar{d} / d$.

506

507

508

509

In this curvilinear formulation, the variation of the mixing length \tilde{l}_t is expressed in terms of η , i.e. normal to the film surface, and thus correlations for parallel flows can be used. Following Tseluiko & Kalliadasis (2011), we employ the van Driest equation (Van Driest 1956):

510

$$\tilde{l}_t = \kappa (\bar{d} - \eta) \left\{ 1 - \exp \left[\sqrt{|T_{G0}|} \frac{\text{Re}_G}{A} \frac{\eta - \bar{d}}{A} \right] \right\}, \quad (3.22)$$

511

where $A=26$, $\kappa=0.41$ is the von Karman constant, and T_{G0} denotes the primary-flow tangential

512 stress, obtained by evaluating (3.30) in the limit $\underline{\epsilon}=0$, which intervenes in the traditional
513 scaling based on the friction velocity \mathcal{U}^+ :

$$514 \quad \mathcal{U}^+ = \{\rho_G^{-1} |T_{G0}^*|\}^{\frac{1}{2}}, \quad \mathcal{L}^+ = \frac{\mu_G}{\rho_G \mathcal{U}^+}. \quad (3.23)$$

515 Finally, the boundary conditions (3.13) become:

$$516 \quad \tilde{u}_G|_{\eta=\bar{d}} = \tilde{v}_G|_{\eta=\bar{d}} = 0, \quad \partial_\eta \tilde{u}_G|_{\eta=0} = \tilde{v}_G|_{\eta=0} = 0. \quad (3.24)$$

517 The BVP given by (3.20) and (3.24) is solved order by order based on a regular expansion
518 in $\underline{\epsilon}$ around $\underline{\epsilon}=0$ (Camassa *et al.* 2017):

$$519 \quad \tilde{u}_G = \tilde{u}_G^{(0)} + \underline{\epsilon} \tilde{u}_G^{(1)} + O(\underline{\epsilon}^2), \quad (3.25a)$$

$$520 \quad \tilde{v}_G = \tilde{v}_G^{(0)} + \underline{\epsilon} \tilde{v}_G^{(1)} + O(\underline{\epsilon}^2), \quad (3.25b)$$

$$521 \quad P_G = P_G^{(0)} + \underline{\epsilon} P_G^{(1)} + O(\underline{\epsilon}^2). \quad (3.25c)$$

523 The zeroth-order problem is obtained by inserting (3.25a) into (3.20) and (3.24) and then
524 truncating at $O(\underline{\epsilon}^0)$. We anticipate a solution in the form of the product ansatz:

$$525 \quad \tilde{u}_G^{(0)} = g_0(\xi) U_0(\eta) = \frac{\bar{d}}{d} U_0(\eta), \quad (3.26)$$

526 which leads to the variable-separated zeroth-order momentum equation:

$$\frac{d^3}{\bar{d}^3} \left\{ \frac{1}{\text{Re}_G} \partial_\xi P_G^{(0)} - \frac{\Pi_L}{\Pi_u^2} \frac{1}{\text{Fr}^2} \sin(\phi) \right\} = \frac{1}{\text{Re}_G} \partial_{\eta\eta} U_0 + \partial_\eta \left\{ \tilde{l}_r^2 \text{sgn}(\partial_\eta U_0) (\partial_\eta U_0)^2 \right\} = C_0, \quad (3.27a)$$

528 subject to the boundary conditions:

$$529 \quad U_0|_{\eta=\bar{d}} = \partial_\eta U_0|_{\eta=0} = 0, \quad (3.27b)$$

530 where we have employed the signum function sgn to substitute $|\partial_\eta U_0| = \text{sgn}(\partial_\eta U_0) \partial_\eta U_0$,
531 and where the separation constant C_0 is obtained from the gauge condition:

$$532 \quad \int_0^{\bar{d}} \tilde{u}_G^{(0)} d\bar{y} = \int_0^{\bar{d}} U_0 d\eta = \frac{q_{G0}}{2} = \frac{1}{2}. \quad (3.27c)$$

534 At the next order, i.e. $O(\underline{\epsilon}^1)$, we obtain in a similar way:

$$\frac{d^2}{\bar{d}^2} \left\{ \frac{1}{\text{Re}_G} \partial_\xi P_G^{(1)} \frac{d}{\partial_\xi d} - \frac{\Pi_L}{\Pi_u^2} \frac{1}{\text{Fr}^2} \cos(\phi) d \right\} = U_0^2 + \frac{1}{\text{Re}_G} \partial_{\eta\eta} U_1$$

$$535 \quad + \partial_\eta \left\{ \tilde{l}_r^2 \text{sgn}(\partial_\eta U_0) \partial_\eta U_0 \partial_\eta U_1 \right\} = C_1, \quad (3.28a)$$

536

$$537 \quad U_1|_{\eta=\bar{d}} = \partial_\eta U_1|_{\eta=0} = 0, \quad (3.28b)$$

538

$$539 \quad \int_0^{\bar{d}} \tilde{u}_G^{(1)} d\bar{y} = \int_0^{\bar{d}} U_1 d\eta = 0, \quad (3.28c)$$

540 where we have employed the product ansatz:

$$541 \quad \tilde{u}_G^{(1)} = g_1(\xi) U_1(\eta) = \frac{\partial_\xi d}{d} U_1(\eta), \quad (3.29)$$

542 and where the separation constant C_1 is obtained from (3.28c).

543 The two BVPs (3.27) and (3.28) are solved numerically for U_0 , U_1 , C_0 , and C_1 via the
544 continuation software `Auto07P` (Doedel 2008). The solution is obtained for a given \bar{d} on
545 a fixed domain spanning $0 \leq \eta \leq \bar{d}$. Based on this, the coupling quantities T_G and $\partial_x P_G$,
546 which appear in the liquid-side model (3.6a), are readily constructed at $O(\underline{\epsilon}^1)$:

$$547 \quad T_G = -\frac{\bar{d}}{d} \partial_\eta \tilde{u}_G \Big|_{\eta=\bar{d}} + O(\underline{\epsilon}^2) = -\frac{\bar{d}}{d} \left\{ \partial_\eta \tilde{u}_G^{(0)} \Big|_{\eta=\bar{d}} + \underline{\epsilon} \partial_\eta \tilde{u}_G^{(1)} \Big|_{\eta=\bar{d}} \right\} + O(\underline{\epsilon}^2), \quad (3.30a)$$

$$548 \quad = -\frac{\bar{d}^2}{d^2} \left\{ \partial_\eta U_0 \Big|_{\eta=\bar{d}} + \frac{\partial_{x^*} d^*}{\bar{d}} \partial_\eta U_1 \Big|_{\eta=\bar{d}} \right\} + O(\underline{\epsilon}^2),$$

$$549 \quad \partial_x P_G = \partial_\xi P_G^{(0)} + \underline{\epsilon} \partial_\xi P_G^{(1)} + O(\underline{\epsilon}^2) \quad (3.30b)$$

$$550 \quad = \text{Re}_G \left\{ \frac{\bar{d}^3}{d^3} \left(C_0 + C_1 \frac{\partial_{x^*} d^*}{\bar{d}} \right) + \frac{\Pi_L}{\Pi_u^2} \frac{1}{\text{Fr}^2} (\sin(\phi) + \cos(\phi) \partial_{x^*} d^*) \right\} + O(\underline{\epsilon}^2),$$

552 where we have used the velocity expansion (3.25a):

$$553 \quad \tilde{u}_G = \frac{\bar{d}}{d} U_0 + \frac{\partial_{x^*} d^*}{d} U_1 + O(\underline{\epsilon}^2). \quad (3.31)$$

554 Importantly, at fixed \bar{d} , T_G and $\partial_x P_G$ (3.30) depend only on $d=D-h/\Pi_L$, which varies with x
555 and t . By contrast, Samanta (2014) assumed $T_G=\text{const}$ and $\partial_x P_G=0$.

556 In contrast to the gas-side description of Demekhin (1981) and Tseluiko & Kalliadasis
557 (2011), (3.30) is obtained from a long-wave and not from a small-wave-amplitude expansion.
558 Thus, it works better when the liquid holdup is larger, whereas the cited models work better
559 when the liquid holdup is small, i.e. $h^*/\bar{d}^* \rightarrow 0$.

560 As a result of our frozen-interface assumption ($\Pi_u \gg 1$) expressed via (3.13), one would
561 obtain exactly the same relations for the functions U_0 and U_1 appearing in (3.30), should
562 one apply no slip and no penetration conditions at $y^*=H^*$ instead of a symmetry condition
563 at $y^*=D^*$. This is because the BVPs for U_0 (3.27) and U_1 (3.28) would remain symmetrical
564 in that case. Thus, up to the order of expansion of our WRIBL-LW model, our symmetry
565 condition (3.13b) is valid without loss of generality.

566 3.3. Rescaling

567 For the remainder of the manuscript, we rescale streamwise lengths by setting $\epsilon=\underline{\epsilon}=1$, and
568 we choose:

$$569 \quad \mathcal{L} = \mathcal{L}_G = H^*, \quad \mathcal{U}_L = \frac{q_{L0}^*}{H^*}, \quad \mathcal{U}_G = \frac{q_{G0}^*}{H^*}. \quad (3.32)$$

570 This implies $\Pi_L=1$, i.e. all lengths are now scaled with the channel height H^* . We recall that
571 q_{L0}^* and q_{G0}^* are the primary-flow liquid and gas flow rates per unit width, and, thus, \mathcal{U}_L and
572 \mathcal{U}_G are the superficial velocities. The corresponding Reynolds numbers are:

$$573 \quad \text{Re}_L = \frac{q_{L0}^*}{\nu_L}, \quad \text{Re}_G = \frac{q_{G0}^*}{\nu_G}, \quad (3.33)$$

574 where $\nu_L=\mu_L/\rho_L$ and $\nu_G=\mu_G/\rho_G$.

575 At some places, we will rescale quantities with the natural scales:

$$576 \quad \mathcal{L}_v = \nu_L^{2/3} g^{-1/3}, \quad \mathcal{U}_v = (\nu_L g)^{1/3}, \quad \mathcal{T}_v = \frac{\mathcal{L}_v}{\mathcal{U}_v} = \nu_L^{1/3} g^{-2/3}. \quad (3.34)$$

577

3.4. Model computations

578 We perform three types of numerical computations based on our WRIBL-LW model (3.6),
 579 (3.30): linear stability calculations, nonlinear computations of travelling-wave solutions
 580 (TWS), and nonlinear computations of spatially-evolving falling liquid films.

581 To obtain the linear stability formulation, we perturb the dependent variables q_L and h
 582 around their primary flow values q_{L0} and h_0 :

$$583 \quad q_L = q_{L0} + \check{q}_L(x, t) = q_0 + \hat{q} \exp\{i(kx - \omega t)\}, \quad (3.35a)$$

$$584 \quad h = h_0 + \check{h}(x, t) = h_0 + \hat{h} \exp\{i(kx - \omega t)\}, \quad (3.35b)$$

585 where the check mark denotes infinitesimal perturbations, ω denotes the angular frequency,
 586 and $\hat{q}_L = \hat{h}\omega/k$ follows from (3.6b). Surface waves resulting from the Kapitza instability grow
 587 spatially, but a counter-current gas flow can cause the onset of absolute instability (AI). Both
 588 phenomena can be captured via a spatial stability formulation (Vellingiri *et al.* 2015). Thus,
 589 we will usually (but not exclusively) assume $k \in \mathbb{C}$ and $\omega \in \mathbb{R}$, with:

$$590 \quad k = k_r + ik_i, \quad (3.36)$$

591 where $k_r = 2\pi/\Lambda$ is the physical wavenumber and $-k_i$ is the spatial growth rate.

592 The film surface perturbation (3.35b) translates to the gas-side problem via:

$$593 \quad d = d_0 + \check{d} = d_0 + \hat{d} \exp\{i(kx - \omega t)\}, \quad \hat{d} = -\frac{\hat{h}}{\Pi_L}. \quad (3.37)$$

594 Inserting this in (3.30) and then linearizing, yields the linear responses of the inter-phase
 595 coupling quantities:

$$596 \quad T_G = T_{G0} + \check{T}_G = T_{G0} + \hat{T}_G \exp\{i(kx - \omega t)\}, \quad (3.38a)$$

$$597 \quad P_G = P_{G0} + \check{P}_G = P_{G0} + \hat{P}_G \exp\{i(kx - \omega t)\}, \quad (3.38b)$$

599 with:

$$600 \quad T_{G0} = -\partial_\eta U_0|_{d_0}, \quad \hat{T}_G = \frac{\hat{d}}{d_0} \left\{ 2 \partial_\eta U_0|_{d_0} + \Pi_L ik \partial_\eta U_1|_{d_0} \right\}, \quad (3.39)$$

601

$$602 \quad \partial_x P_{G0} = \text{Re}_G \left\{ C_0 + \frac{\Pi_L \sin(\phi)}{\Pi_u^2 \text{Fr}^2} \right\}, \quad \hat{P}_G = -\text{Re}_G \frac{\hat{d}}{ik} \left\{ 3 \frac{C_0}{d_0} - \Pi_L \frac{C_1}{d_0} - \frac{\Pi_L^2 \cos(\phi)}{\Pi_u^2 \text{Fr}^2} \right\}. \quad (3.40)$$

603

603 Introducing (3.35) and (3.38) into (3.6), and linearizing once again, yields the dispersion
 605 relation for the spatial stability problem:

$$606 \quad \text{DR} = -i\omega^2 + ik\omega \frac{17}{7} \frac{q_{L0}}{h_0} - ik^2 \frac{9}{7} \frac{q_{L0}^2}{h_0^2} + \frac{5}{6} \text{Fr}^{-2} \left\{ ik^2 \cos(\phi) h_0 - k \sin(\phi) \right\}$$

$$- i^3 k^4 \frac{5}{6} \text{We} h_0 + \frac{5}{2} \frac{1}{\text{Re}_L} \frac{1}{h_0^2} \left\{ \omega - k \frac{2q_{L0}}{h_0} \right\} + i^2 k^3 \frac{6}{\text{Re}_L} \frac{q_{L0}}{h_0} - i^2 k^2 \omega \frac{9}{2} \frac{1}{\text{Re}_L}$$

$$+ \frac{\Pi_\mu \Pi_u}{\Pi_L} \left\{ T_{G0} \left[ik\omega \frac{19}{336} h_0 - i^2 k^3 \frac{1}{6} \frac{1}{\text{Re}_L} h_0 + ik^2 \frac{5}{112} q_{L0} \right] + k \frac{5}{4} \frac{1}{\text{Re}_L} \frac{1}{\Pi_L} \frac{\hat{T}_G}{\hat{d}} \right\}$$

$$+ ik^2 \frac{19}{672} \frac{\Pi_\mu^2 \Pi_u^2}{\Pi_L^2} h_0^2 T_{G0}^2 + k \frac{5}{6} \frac{\Pi_\rho \Pi_u^2}{\Pi_L} \frac{1}{\text{Re}_G} \left\{ \partial_x P_{G0} - \frac{h_0}{\Pi_L} ik \frac{\hat{P}_G}{\hat{d}} \right\} = 0, \quad (3.41)$$

607 where \hat{d} will cancel, due to $\hat{T}_G \propto \hat{d}$ and $\hat{P}_G \propto \hat{d}$ according to (3.39) and (3.40).

608 To compute nonlinear travelling-wave solutions (TWS), we recast (3.6a) into an ODE in
609 terms of the wave coordinate $\gamma = x - ct$:

$$610 \quad h''' = \text{NL}(h, h', h''; \bar{h}, c, q_L^{\text{MF}}), \quad (3.42a)$$

$$611 \quad q_L^{\text{MF}} = q_L - hc = \bar{q}_L - \bar{h}c, \quad (3.42b)$$

612 where primes denote differentiation w.r.t. γ , bars signify averaging over the wavelength
613 Λ in terms of γ , c denotes the nonlinear wave speed, and the subscript MF refers to the
614 moving reference frame. Further, (3.42b) is the integral form of (3.6b), which we have used
615 to eliminate q from (3.42a). The system is closed through periodicity boundary conditions:

$$616 \quad h^{(j)} \Big|_{\gamma=0} = h^{(j)} \Big|_{\gamma=\Lambda}, \quad j = 0, 1, 2, \quad (3.42c)$$

617 and it is solved for a fixed value of \bar{q}_L , enforced through the integral condition:

$$618 \quad \Lambda^{-1} \int_0^\Lambda q_L d\gamma = \bar{q}_L. \quad (3.43)$$

619 We do this numerically via the continuation software `Auto07P`, after recasting (3.42a) into a
620 dynamical system. First, we continue the fixed-point solutions ($h' = h'' = h''' = 0$) of (3.42a) at
621 $q_L = q_{L0}$ and $h = h_0$ in terms of c , until reaching the Hopf bifurcation of the Kapitza instability.
622 Then, starting from this point, periodic solutions are continued in terms of a selected control
623 parameter, e.g. the liquid Reynolds number Re_L . The BVPs associated with the turbulent gas
624 flow, (3.27) and (3.28), are solved simultaneously. In addition, we solve the linear dispersion
625 relation (3.41) for the spatially most-amplified angular frequency ω_{\max} :

$$627 \quad \text{DR}(\omega_{\max}, k) = 0, \quad \partial_\omega k_i \Big|_{\omega=\omega_{\max}} = 0. \quad (3.44)$$

628 By imposing $f = f_{\max} = \omega_{\max}/2\pi$, TWS most-likely to emerge in an experiment can be tracked.

629 To compute the spatial evolution of nonlinear Kapitza waves, we solve (3.6a) and (3.6b)
630 numerically on an open domain with inlet/outlet conditions. Details of the numerical scheme
631 are given in appendix F3 of Kalliadasis *et al.* (2012). In particular, we apply a second-
632 order central-differences spatial discretization and a quasi-linearized Crank-Nicolson time
633 integration. At the liquid outlet, we impose the soft boundary conditions of Richard *et al.*
634 (2016). At the liquid inlet, we explicitly prescribe h and q at the first two grid points ($i_x = 1, 2$),
635 based on the primary flow:

$$636 \quad h \Big|_{i_x=1} = h \Big|_{i_x=2} = h_0, \quad (3.45a)$$

$$637 \quad q_L \Big|_{i_x=1} = q_L \Big|_{i_x=2} = q_{L0} [1 + F(t)], \quad (3.45b)$$

639 where the function $F(t)$ allows to apply a tailored inlet forcing:

$$640 \quad F(t) = \varepsilon_1 \sin(2\pi f t) + \varepsilon_2 \sum_{k=1}^N \sin(2\pi k \Delta f t + \varphi_{\text{rand}}), \quad \Delta f = 2 f_c / N. \quad (3.46)$$

641 The first term in (3.46) constitutes a harmonic perturbation of frequency f and the second
642 one mimics white noise through a series of $N=1000$ Fourier modes that are shifted by a
643 random phase shift $\varphi_{\text{rand}} = \varphi_{\text{rand}}(k) \in [0, 2\pi]$ and that span a frequency range of twice the
644 linear cut-off frequency f_c (Chang *et al.* 1996a). When $\varepsilon_1 = 0$, the inlet perturbation consists
645 of only white noise. This setting will be used to simulate the natural, noise-driven, evolution
646 of a wavy film as it would occur in a real system. In other computations, we will apply
647 additional coherent inlet forcing by setting $\varepsilon_1 > 0$.

648 4. Linear stability analysis based on full RANS equations

649 The long-wave asymptotic expansion underlying the gas-side representation (3.30) in our
 650 WRIBL-LW model is truncated at order $\underline{\epsilon}^1$, whereas our liquid-side representation (3.6) is
 651 consistent up to order ϵ^2 . To validate linear stability predictions based on this model, and
 652 to go beyond its limitations, we introduce two linear stability formulations that are based on
 653 the full RANS equations in the gas (4.3). The first formulation (section 4.1) relies on the
 654 WRIBL model in the liquid (3.6), and we designate this approach as WRIBL-OS, where OS
 655 refers to the Orr-Sommerfeld equation. The second formulation (section 4.2) relies on the
 656 full Navier-Stokes equations in the liquid (3.1), and we designate that approach as OS-OS.

657 4.1. WRIBL-OS approach

658 In our WRIBL-OS approach, the linear response of the liquid film is governed by the
 659 dispersion relation (3.41), but the perturbation amplitudes \hat{T}_G and \hat{P}_G are now obtained from
 660 the full (steady) RANS equations (3.8). For this, we recast (3.8) in terms of the curvilinear
 661 coordinates (3.15) and introduce the gas stream function Ψ :

$$662 \quad \tilde{u} = \frac{\hat{d}}{d} \partial_\eta \Psi, \quad \tilde{v} = -\partial_\xi \Psi, \quad (4.1)$$

663 which we perturb, along with p_G and d , around the primary flow (subscript 0):

$$664 \quad \Psi = \Psi_0 + \check{\Psi} = \Psi_0 + \psi(\eta) \exp \{i(k\xi - \omega t)\}, \quad (4.2a)$$

$$665 \quad p_G = p_{G0} + \check{p}_G = p_{G0} + \hat{p}_G(\eta) \exp \{i(k\xi - \omega t)\}, \quad (4.2b)$$

$$666 \quad d = d_0 + \check{d} = d_0 + \hat{d} \exp \{i(k\xi - \omega t)\}, \quad (4.2c)$$

668 where $k = k_r \in \mathbb{R}$, and the time dependence is included formally to account for the the
 669 unsteadiness of the liquid film. Upon linearization and subtraction of the primary flow,
 671 we obtain the linearized curvilinear RANS equations in ξ -direction:

$$672 \quad \text{OS}_\xi : \quad \text{Re}_G ik \left\{ \psi' \Psi_0' - \frac{\hat{d}}{d_0} \Psi_0'' - \psi \Psi_0'' \right\} + \text{Re}_G \tilde{l}_t |\Psi_0''| \left\{ \tilde{l}_t' \left[k^2 \left(-2\psi + 3 \frac{\hat{d}}{d_0} \eta \Psi_0' \right) - 4\psi'' \right. \right. \\ \left. \left. + 6 \frac{\hat{d}}{d_0} \Psi_0'' \right] + \tilde{l}_t \left[-2\psi''' + 6 \frac{\hat{d}}{d_0} \Psi_0''' - 2 \frac{\Psi_0''''}{\Psi_0''} \psi'' + k^2 \left(-\psi' + \frac{3}{2} \frac{\hat{d}}{d_0} \Psi_0' + \frac{3}{2} \frac{\hat{d}}{d_0} \eta \Psi_0'' \right. \right. \right. \\ \left. \left. \left. - \frac{\Psi_0''''}{\Psi_0''} \psi + \frac{3}{2} \frac{\hat{d}}{d_0} \eta \frac{\Psi_0'''' \Psi_0'}{\Psi_0''} \right) \right] \right\} = -ik \hat{p}_G + \psi''' - 3 \frac{\hat{d}}{d_0} \Psi_0''' - k^2 \left\{ \psi' - \frac{\hat{d}}{d_0} \Psi_0' - \frac{\hat{d}}{d_0} \eta \Psi_0'' \right\}, \quad (4.3a)$$

674 and in η direction:

$$675 \quad \text{OS}_\eta : \quad \text{Re}_G k^2 \left\{ \psi \Psi_0' - \frac{\hat{d}}{d_0} \eta \Psi_0'^2 \right\} + \text{Re}_G \tilde{l}_t |\Psi_0''| ik \left\{ 2\tilde{l}_t' \frac{\hat{d}}{d_0} \eta \Psi_0'' + \tilde{l}_t \left[-2\psi'' + 2 \frac{\hat{d}}{d_0} \Psi_0'' \right. \right. \\ \left. \left. + 2\eta \frac{\hat{d}}{d_0} \Psi_0''' + k^2 \left(-\psi + \frac{3}{2} \frac{\hat{d}}{d_0} \eta \Psi_0' \right) \right] \right\} = -\hat{p}'_G - ik^3 \left\{ -\psi + \frac{\hat{d}}{d_0} \eta \Psi_0' \right\} \\ - ik \left\{ \psi'' - 2 \frac{\hat{d}}{d_0} \Psi_0'' - \frac{\hat{d}}{d_0} \eta \Psi_0''' \right\}, \quad (4.3b)$$

676 where primes denote differentiation w.r.t. η . The pressure perturbation amplitude \hat{p}_G can be
677 removed from (4.3a) and (4.3b) via:

$$678 \quad \text{OS} : \quad \partial_\eta \text{OS}_\xi - ik \text{OS}_\eta, \quad (4.3c)$$

679 where OS is the final gas-side Orr-Sommerfeld equation, involving only ψ and its derivatives.
680 The problem is closed with the boundary conditions (3.24):

$$681 \quad \psi''|_{\eta=0} = 0, \quad \psi|_{\eta=0} = 0, \quad \psi'|_{\eta=d_0} = 0, \quad \psi|_{\eta=d_0} = 0. \quad (4.3d)$$

682 We solve (4.3) numerically for ψ with the continuation software Auto07P, starting from
683 the analytically tractable laminar long-wave limit ($\tilde{l}_t=k=0$). The amplitudes of the linear
684 perturbations of the inter-phase coupling quantities:

$$685 \quad \check{T}_G = \hat{T}_G \exp \{i(k\xi - \omega t)\}, \quad \check{P}_G = \hat{P}_G \exp \{i(k\xi - \omega t)\}, \quad (4.4)$$

686 can be readily obtained by recasting (3.14) in curvilinear coordinates, inserting (4.2), and
687 linearizing:

$$688 \quad \hat{T}_G = -\psi''|_{\eta=d_0} + 2\frac{\hat{d}}{d_0} \Psi_0''|_{\eta=d_0}, \quad (4.5a)$$

689

$$690 \quad ik\hat{P}_G = \left\{ \psi'''|_{\eta=d_0} - 3\frac{\hat{d}}{d_0} \Psi_0'''|_{\eta=d_0} + k^2\hat{d} \Psi_0''|_{\eta=d_0} \right\}. \quad (4.5b)$$

691 We point out that $\psi \propto \hat{d}$ and, thus, \hat{d} once again cancels from (3.41), as it should. Also, the
692 spatial variations prescribed in (3.37) and (4.2) are equivalent in the linear limit $\hat{d} \rightarrow 0$,
693 where the curvilinear coordinates collapse with the Cartesian ones. Thus, $\partial_x \check{P}_G = \partial_\xi \check{P}_G$.

694 Panels 5a and 5b represent spatial linear stability predictions obtained with our WRIBL-
695 OS approach, based on (3.41) and (4.3c), for parameters according to the experiments of
696 Kofman *et al.* (2017) in an $H^*=19$ mm channel. According to panel 5a, the maximum of the
697 growth rate dispersion curve increases with increasing counter-current gas flow rate, up until
698 forming a pinch point at $\text{Re}_G=-8490$, where the AI limit is reached (curve with crosses).

699 This destabilization of the liquid film is caused by the inter-phase pressure coupling, as can
700 be deduced by confronting panel 5a with panel 5b, where we have represented corresponding
701 growth rate curves in the limit $\Pi_\rho=0$. In that case, the gas-effect enters only via T_G , and we
702 observe a stabilization of the liquid film at large $|\text{Re}_G|$ (compare crosses and pentagons).
703 Models that do not account for the gas pressure P_G , e.g. the weak-confinement first-order
704 WRIBL model of Tseluiko & Kalliadasis (2011), may thus give qualitatively incorrect linear
705 stability predictions for the current configuration. The same observation also holds at weaker
706 confinement, as shown by confronting panels 5c and 5d, where we have chosen $H^*=40$ mm.

707 As a result of our frozen-interface assumption ($\Pi_u \gg 1$) expressed through the last two
708 equations in (4.3d), one would obtain exactly the same linear stability problem (4.3) should
709 one apply no slip and no penetration conditions at $y^*=H^*$ instead of a symmetry condition
710 at $y^*=D^*$. This is because the primary gas flow would remain symmetrical about the center
711 line of the gas layer. Thus, for all linear stability calculations based on the gas-side OS BVP
712 (4.3), our symmetry condition (4.3d) is valid analytically.

713

4.2. OS-OS approach

714 Linear stability calculations based on our WRIBL-LW and WRIBL-OS approaches may be
715 limited to long-wave instability modes. To capture short-wave instability modes (section 6.2),
716 we introduce a stability formulation based on the full Navier-Stokes equations (3.1) in the
717 liquid and the full RANS equations (4.3) in the gas.

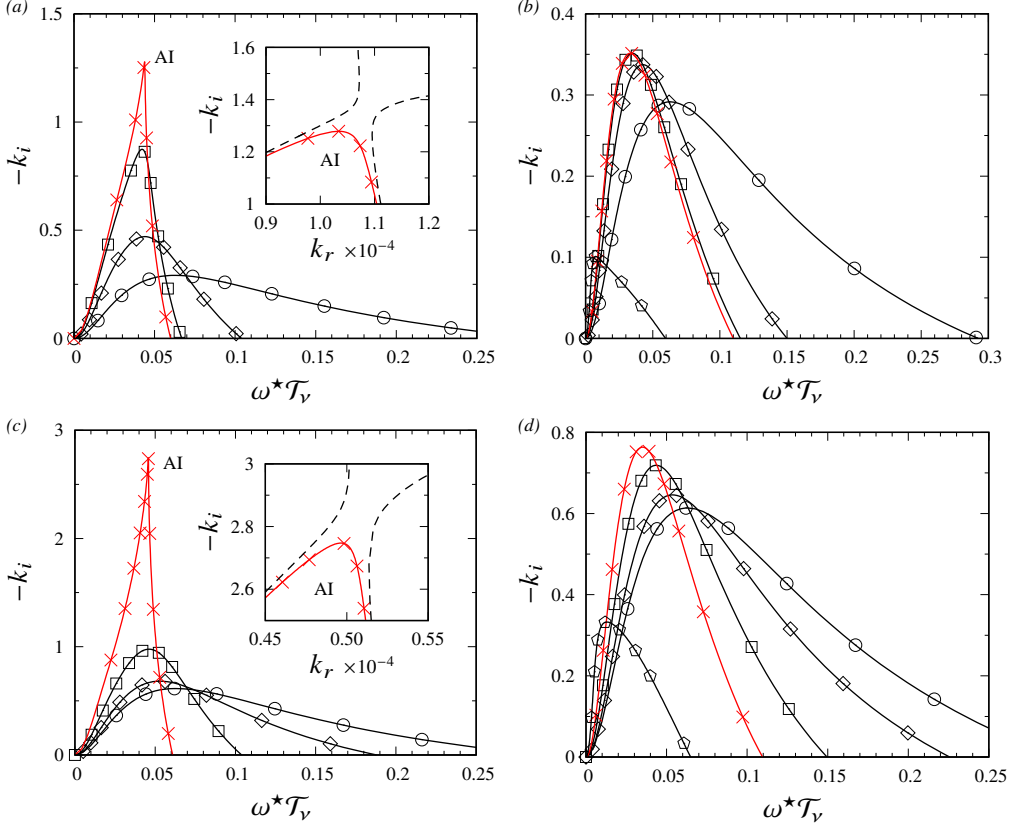


Figure 5: Spatial linear stability calculations with WRIBL-OS approach. Parameters based on experiments of Kofman *et al.* (2017): $Ka=3174$ (water and air I in table 1), $\phi=5^\circ$, $Re_L=45$. Circles: passive-gas limit, $\Pi_\rho=\Pi_\mu=0$ in (3.41). $[Re_G]$ increases in the order: [diamonds, squares, crosses, pentagons]. (a,c) Full model; (b,d) $\Pi_\rho=0$ in (3.41). (a,b) $H^*=19$ mm; (c,d) $H^*=40$ mm. (a) $Re_G=[-6234, -8145, -8490$ (AI)]. Dashed: $Re_G=-8500$; (b) $Re_G=[-6234, -8145, -8490, -15000]$; (c) $Re_G=[-8145, -15000, -20430$ (AI limit)]. Dashed: $Re_G=-20440$; (d) $Re_G=[-8145, -15000, -20430, -35000]$. We have rescaled ω with $\mathcal{T}_v=2.207 \times 10^{-3}$ s (3.34).

718 The gas-side linear response is governed by the same equations as in the WRIBL-OS
 719 approach, i.e. (4.3) and (4.5), and we focus here on deriving those governing the liquid-side
 720 linear response. For this, we perturb the film thickness as:

$$721 \quad h = h_0 + \check{h} = h_0 + \hat{h} \exp \{ ik(x - ct) \}, \quad (4.6)$$

722 assuming a temporal stability formulation this time, i.e. $k \in \mathbb{R}$ and $c=c_r + i c_i \in \mathbb{C}$, where c_r
 723 denotes the wave speed and kc_i the temporal growth rate.

724 We start with the full governing equations (3.1). Considering these in the limit of fully
 725 developed flow with $h=h_0$, yields the liquid primary flow:

$$726 \quad u_{L0} = \frac{1}{2} Re_L \left\{ \Pi_\rho \partial_x p_{G0} - \frac{\sin(\phi)}{Fr^2} \right\} (y^2 - 2yh_0) + \frac{\Pi_\mu \Pi_u}{\Pi_L} T_{G0} y, \quad (4.7a)$$

727

$$728 \quad \partial_y p_{L0} = -\frac{\cos(\phi)}{Fr^2}. \quad (4.7b)$$

Fluids	ρ (kg/m ³)	ν (m ² /s)	σ (N/m)	Ka	T (°C)	figures
Water	998.3	$1.03 \cdot 10^{-6}$	0.071	3174	19	5, 6, 8, 9, 11-13,
Air I	1.209	$14.9 \cdot 10^{-6}$	-	-	19	18-21, 24-27
DMSO(83%)-water	1098.3	2.85×10^{-6}	0.0484	509.5	25	22, 23
Glycerol(54%)-water	1000	2.3×10^{-6}	0.0626	963	22	7
Air II	1.185	$15.6 \cdot 10^{-6}$	-	-	25	7, 22, 23
Methanol	791	$0.73 \cdot 10^{-6}$	0.022	1988	25	28, 29a
Helium	0.165	$12.1 \cdot 10^{-5}$	-	-	25	

Table 1: Fluid combinations used in our computations. The Kapitza number is defined as $Ka = \sigma / \rho_L / g^{1/3} / \nu_L^{1/3}$, where σ , ρ_L , and ν_L denote the surface tension, density and kinematic viscosity of the liquid, and g designates the gravitational acceleration.

729 Next, we introduce the liquid stream function Φ :

$$730 \quad u_L = \partial_y \Phi, \quad v_L = -\partial_x \Phi, \quad (4.8)$$

731 which we perturb around the primary flow:

$$732 \quad \Phi = \Phi_0 + \check{\Phi} = \Phi_0 + \phi(y) \exp \{ik(x - ct)\}. \quad (4.9)$$

733 Substituting (4.8) and (4.9) into (3.1), linearizing w.r.t. $\check{\Phi}$, subtracting the primary flow, and
734 applying standard manipulations, we obtain the liquid-side Orr-Sommerfeld equation:

$$735 \quad \phi^{iv} - 2k^2 \phi'' + k^4 \phi = ik \text{Re}_L \left\{ (c - u_{L0}) (k^2 \phi - \phi'') - \phi u_{L0}' \right\}, \quad (4.10a)$$

736 the boundary conditions at $y=0$:

$$737 \quad \phi'' = \phi = 0, \quad (4.10b)$$

738 and the inter-phase coupling conditions at $y=h_0$:

$$739 \quad \phi u_{L0}' + \tilde{c} \{ \phi'' + k^2 \phi \} = \Pi_\mu \Pi_u \tilde{c} \hat{T}_G, \quad (4.10c)$$

$$742 \quad -\frac{1}{\text{Re}_L} \{ 2k^2 \phi u_{L0}' + \tilde{c} [3k^2 \phi' - \phi'''] \} - ik \tilde{c} \{ -\tilde{c} \phi' - \phi u_{L0} \} \quad (4.10d)$$

$$+ ik \phi p_{L0}' = ik \frac{\Pi_\rho \Pi_u^2}{\text{Re}_G} \tilde{c} \hat{P}_G + ik^3 \text{We} \phi,$$

743 where primes denote differentiation w.r.t. y , and where we have introduced $\tilde{c} = c - u_{L0}|_{y=h_0}$.

744 The non-linearity involving \tilde{c} in (4.10d) can be eliminated via (4.10c). Further, \hat{T}_G and \hat{P}_G
745 are rescaled versions of the amplitudes in (4.5):

$$746 \quad \hat{T}_G = -\hat{h} \frac{\hat{T}_G}{\hat{d}}, \quad \hat{P}_G = \hat{h} \frac{\hat{P}_G}{\hat{d}}, \quad (4.11)$$

747 where \hat{d} is an arbitrary deflection amplitude used in the solution of the gas-side problem
748 (4.3), and \hat{h} is directly linked to ϕ via the kinematic condition (3.1f):

$$749 \quad \hat{h} = \frac{\phi|_{y=h_0}}{\tilde{c}}. \quad (4.12)$$

750 The rescaling in (4.11) allows to solve the gas- and liquid-side problems sequentially.

751 We solve the two-phase BVP comprising (4.3) and (4.10) by expanding the stream
 752 function amplitudes ϕ and ψ in terms of Chebyshev polynomials (Boomkamp *et al.* 1997;
 753 Barmak *et al.* 2016b):

$$754 \quad \phi(\zeta) = c_{L0} + \sum_{j=1}^{N_p} c_{1j} T_j(\zeta), \quad \psi(\zeta) = c_{G0} + \sum_{j=1}^{N_p} c_{gj} T_j(\zeta), \quad (4.13)$$

755 where T_j are j th-degree Chebyshev polynomials of the first kind, defined on the interval
 756 $\zeta \in [-1, 1]$, with:

$$757 \quad \zeta = 2 \frac{y}{h_0} - 1 \quad \text{for } 0 \leq y \leq h_0, \quad (4.14)$$

$$758 \quad \zeta = 1 - 2 \frac{\eta}{d_0} \quad \text{for } 0 \leq \eta \leq d_0. \quad (4.15)$$

760 Thus, there are $2(N_p + 1)$ unknown coefficients c_{kj} , which are fixed by the 8 conditions
 761 in (4.10b), (4.10c), (4.10d), and (4.3d), and $2(N_p + 1) - 8$ additional constraints obtained by
 762 evaluating the ODEs (4.10a) and (4.3c) at the inner collocation points $\zeta_2, \dots, \zeta_{N_p-2}$, defined
 763 according to:

$$764 \quad \zeta_i = \cos \left[\frac{i\pi}{N_p} \right] \quad \forall i \in [0, N_p]. \quad (4.16)$$

765 Instead of solving for the coefficients c_{kj} , we solve directly for the $2(N_p + 2)$ unknowns
 766 $\phi(\zeta_i)$ and $\psi(\zeta_i)$, arranged into the solution vectors:

$$767 \quad \boldsymbol{\phi} = [\phi(\zeta_0), \dots, \phi(\zeta_{N_p})]^T, \quad \boldsymbol{\psi} = [\psi(\zeta_0), \dots, \psi(\zeta_{N_p})]^T. \quad (4.17)$$

768 Then, by making use of the Chebyshev differentiation matrix \mathbf{D} (Trefethen 2000):

$$769 \quad [\phi^{(i)}(\zeta_0), \dots, \phi^{(i)}(\zeta_{N_p})]^T = \mathbf{D}^i [\phi(\zeta_0), \dots, \phi(\zeta_{N_p})]^T, \quad (4.18)$$

770

$$771 \quad [\psi^{(i)}(\zeta_0), \dots, \psi^{(i)}(\zeta_{N_p})]^T = \mathbf{D}^i [\psi(\zeta_0), \dots, \psi(\zeta_{N_p})]^T, \quad (4.19)$$

772 where $i=1, 2, 3, 4$, and (i) indicates the order of differentiation w.r.t. ζ , (4.10) is cast into a
 773 generalized eigenvalue problem in matrix form:

$$774 \quad \underline{A}\boldsymbol{\phi} = \tilde{c} \underline{B}\boldsymbol{\phi}, \quad (4.20)$$

775 and (4.3) is cast into a linear system of equations:

$$776 \quad \underline{C}\boldsymbol{\psi} = \mathbf{b}, \quad (4.21)$$

777 introducing the coefficient matrices \underline{A} , \underline{B} , and \underline{C} , and the inhomogeneity \mathbf{b} . With the help
 778 of MATLAB (MATLAB 2015), we first solve (4.21) for $\boldsymbol{\psi}$ by numerical inversion via the /
 779 operator and then (4.20) for the eigenvalues \tilde{c} and eigenvectors $\boldsymbol{\phi}$ via the eig function.

780 Using this approach, the full set of eigenmodes is computed at once. Thus, short-wave
 781 instability modes, i.e. modes with $c_i \neq 0$ at $k=0$, can be readily obtained. Once a mode has
 782 been identified at a given wavenumber k , it can be tracked by advancing k , using the function
 783 eig, which searches for eigenvalues in the vicinity of a previous solution.

784 In appendix A, we validate our OS-OS approach, (4.20) and (4.21), versus Vellingiri *et al.*
 785 (2015) and Schmidt *et al.* (2016). Figure 6 confronts temporal linear stability predictions
 786 from this approach (solid lines) with predictions from our WRIBL-OS approach (symbols),
 787 for similar parameters as panel 5a. Agreement is good up to $|\text{Re}_G| \sim 8000$. Thus, our liquid-side
 788 WRIBL description suffices to predict the gas-effect on the long-wave Kapitza instability.

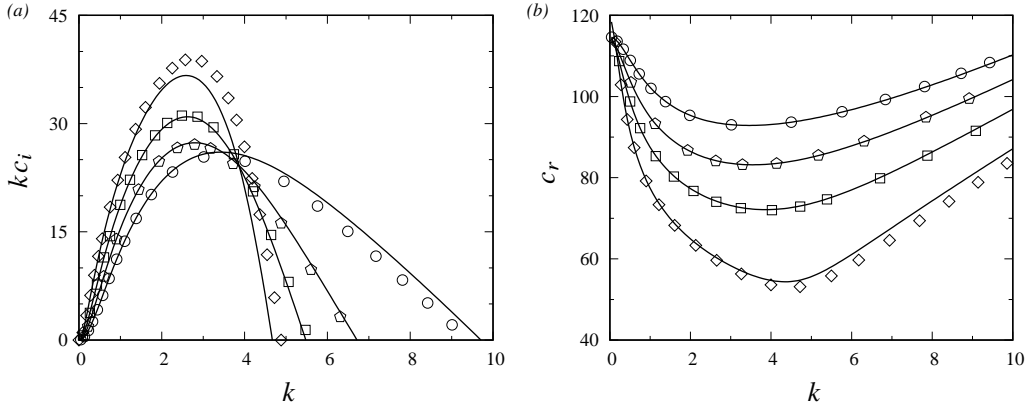


Figure 6: Temporal stability predictions from OS-OS (solid curves) and WRIBL-OS (open symbols) approaches. Similar parameters as in panel 5a: $Ka=3174$, $H^*=19$ mm, $\phi=5^\circ$, $Re_L=32.7$. Circles: passive-gas limit ($\Pi_\rho=\Pi_\mu=0$ in equation 3.41), pentagons: $Re_G=4123$, squares: $Re_G=6173$, diamonds: $Re_G=8220$. (a) Growth rate; (b) wave speed.

789 5. Model validation

790 To evaluate the linear and nonlinear predictions of our WRIBL-LW model, we confront these
 791 with stability predictions from Vellingiri *et al.* (2015) and Samanta (2014), our own stability
 792 calculations using the WRIBL-OS approach, and experiments from Kofman (2014).

793 By design, our WRIBL-LW model exactly predicts the neutral linear stability bound of
 794 the long-wave Kapitza instability. We consider a temporal linear stability formulation and
 795 expand the complex wave speed $c=\omega/k$ in terms of $k \in \mathbb{R}$ around the limit $k=0$:

$$796 \quad c = c_0 + kc_1 + O(k^2). \quad (5.1)$$

797 Inserting this into (3.41), and truncating order by order, we obtain c_0 and c_1 :

$$798 \quad c_0 = 2 u_{L0}|_{h_0} + \Pi_\mu \Pi_u T_{G0} \left\{ -h_0 + \frac{h_0^2}{d_0} \right\} + Re_L \Pi_\rho \Pi_u^2 \frac{h_0^3}{d_0} \left\{ -\frac{\partial_x P_{G0}}{Re_G} + \Pi_u^{-4} \frac{\sin(\phi)}{Fr^2} \right\}, \quad (5.2a)$$

$$799 \quad c_1 = i \mathcal{R}, \quad (5.2b)$$

801 where $\mathcal{R} \in \mathbb{R}$ is written out in appendix B, and the primary flow yields:

$$802 \quad u_{L0}|_{h_0} = \frac{1}{2} \frac{Re_L}{Fr^2} \sin(\phi) h_0^2 + \Pi_\mu \Pi_u T_{G0} h_0 - \frac{1}{2} \Pi_\rho \Pi_u^2 \frac{Re_L}{Re_G} \partial_x P_{G0} h_0^2. \quad (5.3)$$

803 Thus, the asymptotic wave speed is given by c_0 , the (temporal) growth rate by kc_1 , and the
 804 neutral stability bound by $\mathcal{R}=0$.

805 In the zero-confinement limit, $h_0/d_0 \rightarrow 0$, c_0 (5.2a) and c_1 (5.2b) should collapse with the
 806 expressions in equations (B4b) and (B7b) of Vellingiri *et al.* (2015). Applying this limit to
 808 (5.1) and rescaling appropriately, we obtain:

$$809 \quad \underline{c} = \underline{c}_0 + \underline{k} \underline{c}_1 + O(\underline{k}^2) = 2 + \underline{T}_{G0} + i \underline{k} \left\{ \frac{4}{15} \underline{Re}_L (2 + \underline{T}_{G0}) - \frac{2}{3} \cot(\phi) [1 - \Pi_\rho] \right. \\ \left. + \frac{1}{3} \Pi_\rho \frac{Re_L}{\Pi_\mu^2} \frac{\underline{c}_1}{\underline{d}_0} + \frac{1}{2} \Pi_\mu \frac{1}{\underline{d}_0} \partial_{\underline{\eta}} \underline{U}_1 \Big|_{\underline{d}_0} \right\} + O(\underline{k}^2), \quad (5.4)$$

810 where the underline refers to the scaling of Vellingiri *et al.* (2015), i.e. $\underline{\mathcal{L}}=h_0^*$ and

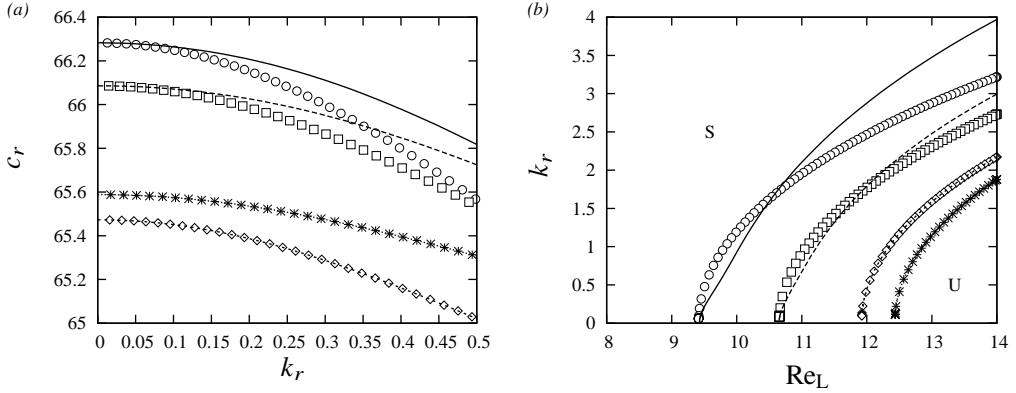


Figure 7: Spatial linear stability predictions obtained from WRIBL-LW (symbols) and WRIBL-OS (lines) calculations. Inclined falling liquid film sheared by a co-current gas based on parameters in Samanta (2014): $Ka=963$ (glycerol-water and air II in table 1), $\phi=4^\circ$, $H^*=15$ mm, $Re_G=2000$. S/U indicate stable/unstable regions. Circles: full formulation; squares: $\Pi_\rho=0$ in (3.41); diamonds: $T_G=T_{G0}$, $\Pi_\rho=0$; crosses: $\Pi_\mu=\Pi_\rho=0$. (a) Wave speed $c_r=\omega/k_r$ around the long-wave limit $k_r \rightarrow 0$; (b) neutral stability bound, $k_i=0$.

811 $\underline{U}=\underline{U}_G=\frac{1}{2}v_L^{-1}g \sin(\phi) h_0^{*2}$. Our result matches that in the reference, except for three
 812 additional terms: the gas-density correction in the $\cot(\phi)$ term, and the last two terms within
 813 the accolades, which stem from the linear perturbations of P_G and T_G . In the laminar limit:

$$814 \quad \underline{C}_1 = \frac{6}{35} d_0^2 T_{G0}^2, \quad \partial_{\underline{d}_0} \underline{U}_1 \Big|_{d_0} = \frac{4}{105} \frac{\Pi_\rho Re_L}{\Pi_\mu^3} d_0^3 T_{G0}^2, \quad (5.5)$$

815 and, thus, these terms do not necessarily vanish for $1/d_0 \rightarrow 0$. Thus, the gas pressure P_G can
 816 affect stability even under weak confinement, in line with observations in panels 5c and 5d.

817 Figure 7 compares spatial linear stability predictions of our WRIBL-LW model (symbols)
 818 with calculations using the WRIBL-OS approach (solid lines), for parameters based on figure
 819 3 in Samanta (2014), which are inspired by the experiments of Liu & Gollub (1994) in a
 820 water-glycerol film. We fix the channel height at $H^*=15$ mm and apply a co-current turbulent
 821 gas flow with $Re_G=2000$. Panel 7a represents dispersion curves of the linear wave speed
 822 $c_r=k_r/\omega$ around the long-wave limit. We see that the two data sets converge as $k \rightarrow 0$. Further,
 823 our WRIBL model accurately captures the long-wave instability threshold, as evidenced by
 824 the neutral stability bounds plotted in panel 7b. Comparing the circles (full model) with the
 825 diamonds (passive-gas limit $\Pi_\rho=\Pi_\mu=0$), we see that the gas-effect is destabilizing, and this is
 826 maintained in the limit $\Pi_\rho=0$ (squares). By contrast, assuming $T_G=\text{const}$ and $\Pi_\rho=0$ (crosses),
 827 according to the model of Samanta (2014), results in a qualitatively incorrect prediction of
 828 gas-induced stabilization.

829 We now turn to the experimental conditions of Kofman (2014), who considered a falling
 830 liquid film sheared by a turbulent counter-current gas flow. Figure 8 confronts linear spatial
 831 growth rate dispersion curves from our WRIBL-LW model (panels 8a, 8c) with calculations
 832 based on our WRIBL-OS approach (panels 8b, 8d). Comparing panels 8a and 8b, we see that
 833 our WRIBL-LW model predicts the gas-effect on the maximum growth rate $\{-k_i\}_{\max}$ and on
 834 the associated angular frequency $\{\omega\}_{\max}$ reasonably well. And, the AI limit is predicted with
 835 a precision of 10 %, i.e. $Re_G^{AI}=-9157$ from WRIBL-LW versus $Re_G^{AI}=-8220$ from WRIBL-OS.
 836 Panels 8c and 8d represent corresponding stability calculations in the limit $\Pi_\rho=0$. Versus
 837 panels 8a and 8c, we observe a qualitative change in the gas-effect from destabilizing to
 838 stabilizing (similar to figure 5), and our WRIBL-LW model accurately captures this feature.

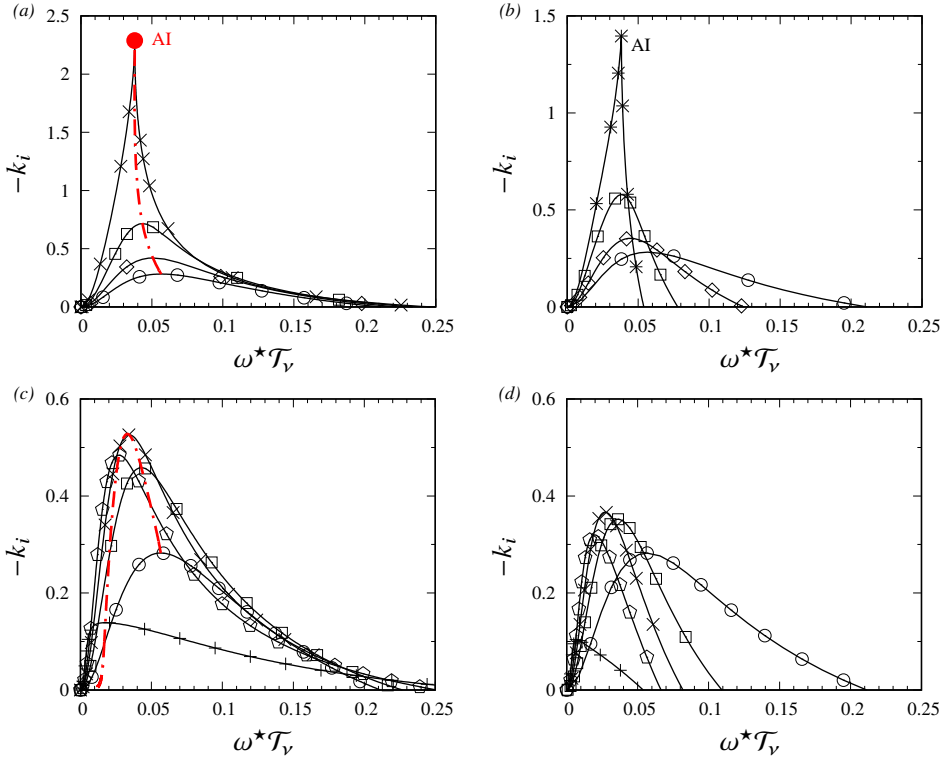


Figure 8: Spatial linear stability predictions from WRIBL-LW (panels *a,c*) and WRIBL-OS (panels *b,d*) approaches. Parameters according to experiments of Kofman (2014): $Ka=3174$ (water and air I in table 1), $H^*=19$ mm, $\phi=5^\circ$, $Re_L=32.7$. Open circles: passive-gas limit, $\Pi_\rho=\Pi_\mu=0$ in (3.41). $|Re_G|$ increases in the order: [diamonds,squares,crosses/asterisks,pentagons,pluses]. (*a,b*) Full model; (*c,d*) $\Pi_\rho=0$ in (3.41). (*a*) $Re_G=[-4123,-6713,-9157]$; (*b*) $Re_G=[-4123,-6713,-8220]$; (*c*) $Re_G=[-6713,-9100,-11000,-15000]$; (*d*) $Re_G=[-6713,-9100,-11000,-15000]$. Red dot-dashed curves track growth rate maximum $\{-k_i\}_{\max}$. We have rescaled ω with $\tau_v=2.207 \times 10^{-3}$ s (3.34).

839 In contrast to Tseluiko & Kalliadasis (2011), our WRIBL-LW model can thus be applied to
 840 confinement levels, where the gas pressure plays a role.

841 On the downside, our WRIBL-LW model cannot reproduce the strong gas-induced
 842 reduction of the cut-off frequency predicted by the WRIBL-OS calculation in panel 8b. This
 843 is due to truncating our asymptotic gas-side description (section 4.2) at $\mathcal{O}(\epsilon^1)$. However, it is
 844 almost inconsequential for the prediction of nonlinear Kapitza waves. Figure 9 compares film
 845 thickness time traces at a fixed streamwise position x , as obtained from open-domain (dashed
 846 black) and TWS (solid green) computations with our WRIBL-LW model, with experimental
 847 data (red open circles) from Kofman (2014). In these experiments, the counter-current gas
 848 flow rate was increased up to $|Re_G| \sim 7000$. Our WRIBL-LW model accurately captures the
 849 gas-effect on both the wave height and the number of precursory capillary ripples. The wave
 850 number k of precursory ripples is several tenfold greater than the cut-off wave number k_c of
 851 the Kapitza instability (Dietze 2016; Zhou & Prosperetti 2020). As a result, over-prediction
 852 of the linear cut-off (panel 8a) does not translate to a significant nonlinear error (figure 9).

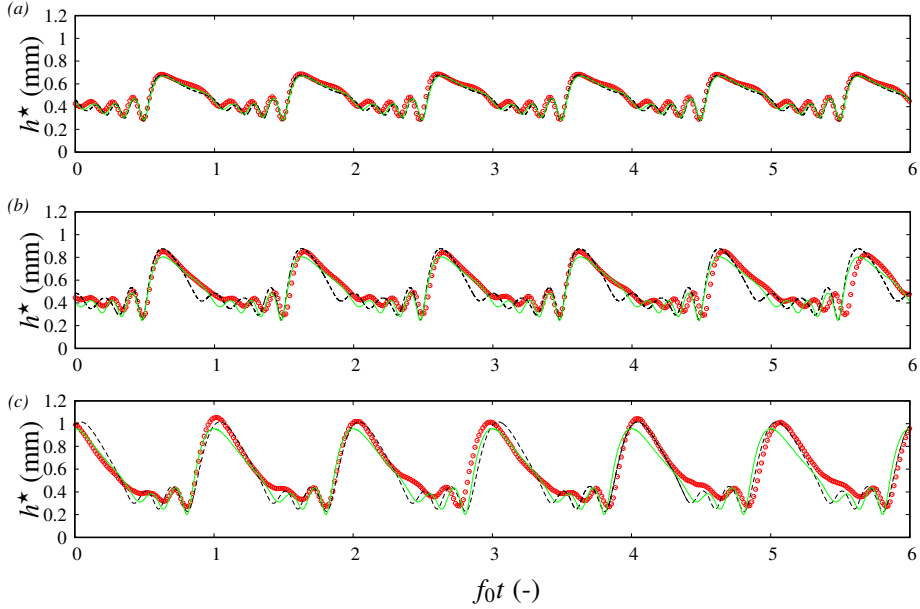


Figure 9: Nonlinear computations (solid and dashed lines) with our WRIBL-LW model (3.6) versus experiments (symbols) of Kofman (2014): $Ka=3174$ (water and air I in table 1), $H^*=19$ mm, $\phi=5^\circ$, $Re_L=32.7$, $f_0^*=2.8$ Hz ($\omega_0^* \mathcal{T}_v=0.039$). Film thickness time traces at fixed streamwise position. Solid green lines: TWS from numerical continuation; dashed black lines: open-domain computations with coherent inlet forcing ($\varepsilon_1=0.01$, $\varepsilon_2=0$). (a) Quiescent gas ($\Pi_\rho=\Pi_\mu=0$ in computations); (b) $Re_G=-4123$; (c) $Re_G=-6713$.

853 6. Results

854 Figure 10 shows top-view snapshots of one of our experiments, where we have successively
 855 increased the counter-current gas flow rate from the second panel onward. Guided by this
 856 experiment, using the different linear stability calculations as well as nonlinear computations
 857 with our WRIBL-LW model, we wish to understand how the waviness of the falling liquid
 858 film is altered under the effect of the gas flow. In particular, we are interested in the transition
 859 from a regular train of long waves (first panel), via an increasingly disordered wave pattern
 860 (e.g. tenth panel), until the occurrence of upward-travelling short ripples, which lead to a
 861 breakdown of our experiment (last panel).

862 6.1. Gas-effect on Kapitza waves

863 This section is concerned with the linear (subsection 6.1.1) and nonlinear (subsections 6.1.2
 864 and 6.1.3) gas-effect on the long-wave Kapitza instability. Waves resulting from this instability
 865 are dominant at weaker counter-current gas flow rates in figure 10, i.e. $|Re_G| \lesssim 6200$ (first ten
 866 panels), and the linear instability becomes absolute in this range, as will be shown in figure
 867 12.

868 6.1.1. Linear gas-effect

869 We start by discussing the gas-effect on the threshold of the Kapitza instability. Panel 11a
 870 represents the neutral stability bound, $c_1=0$ according to (5.2b), in terms of Re_L and Re_G ,
 871 for two inclination angles, i.e. $\phi=5^\circ$ (black curves with circles), which corresponds to our
 872 experiment in figure 10, and $\phi=1^\circ$ (red curves with diamonds). For each ϕ , we have plotted two
 873 curves, one obtained from our WRIBL-LW model for turbulent gas flow conditions (filled
 874 symbols), and another obtained from the fully-coupled governing equations (Tilley *et al.*

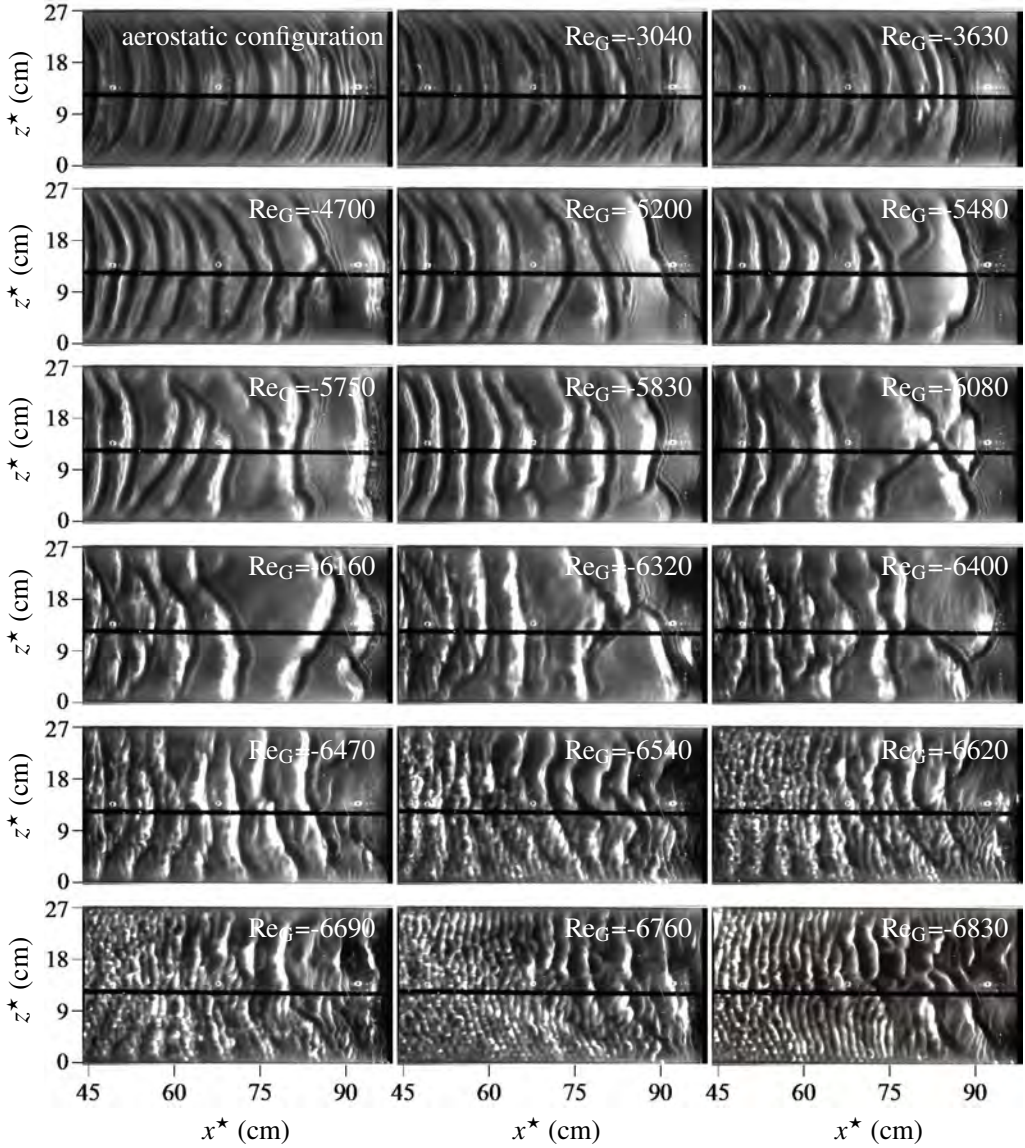


Figure 10: Top view snapshots from one of our experiments. Falling water film sheared by a counter-current air flow and subject to coherent inlet forcing: $H^* = 13$ mm, $\phi = 5^\circ$, $Re_L^{as} = 44.7$, $Re_L = 43.1$, $f_0^* = 3.0$ Hz. First panel: aerostatic configuration; panel 2 and onward: counter-current turbulent gas flow with increasing $|Re_G|$. Absolute instability limit from linear stability calculation in figure 12: $Re_G^{AI} = -5182$.

875 1994) for laminar gas flow conditions (open symbols). Only the curve segments within the
 876 appropriate Re_G range are represented with solid lines, and the laminar/turbulent transition
 877 is highlighted via the shaded region.

878 For $\phi = 5^\circ$ (black curves with circles), the linear effect of the counter-current gas flow is
 879 destabilizing. Further, when the counter-current gas flow rate is sufficiently large, the falling
 880 liquid film becomes unconditionally unstable (limit point marked by filled circle), i.e. for all
 881 Re_L , in agreement with previous works (Trifonov 2017; Kushnir *et al.* 2021). We find that

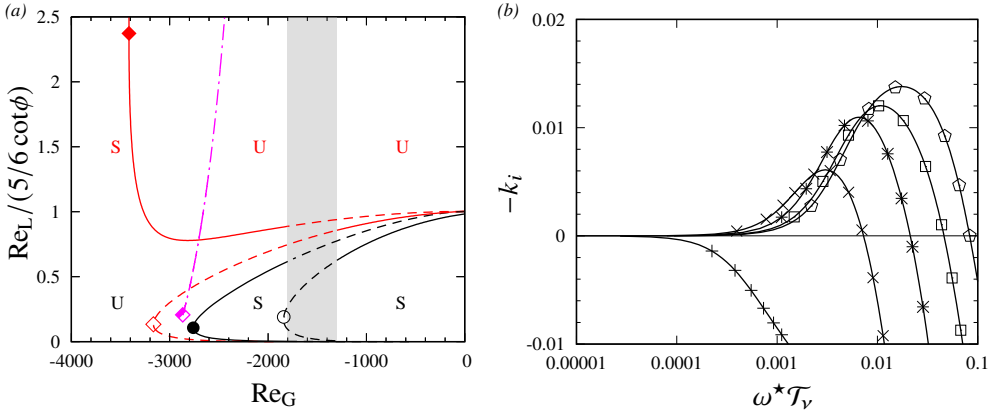


Figure 11: Gas-effect on threshold of long-wave Kapitza instability. Linear stability predictions for a falling liquid film sheared by a counter-current gas flow: $Ka=3174$ (water and air I in table 1), $H^*=13$ mm. (a) Neutral stability bounds. Black curves with circles: $\phi=5^\circ$, red curves with diamonds: $\phi=1^\circ$. Curves with filled symbols: WRIBL-LW/WRIBL-OS prediction for turbulent gas flow, curves with open symbols: fully-coupled prediction for laminar gas flow (Tilley *et al.* 1994), dot-dashed black curve: short-wave instability mode (section 6.2) at $\phi=1^\circ$, shaded zone: turbulence transition, $Re_G \in [-1800, -1300]$. S/U denote stable/unstable regions; (b) spatial growth rate dispersion curves from WRIBL-OS: $\phi=1^\circ$, $Re_L=1.5(5/6) \cot(\phi)$. Pentagons: $\Pi_\rho=\Pi_\mu=0$ in (3.41), squares to pluses: $Re_G=-1000, -2000, -3000, -3600$.

882 turbulence in the gas greatly delays this limit versus a laminar prediction (compare filled and
883 open circle).

884 By contrast, for $\phi=1^\circ$ (red curves with diamonds), we find a change in nature of the
885 gas-effect, as a result of gas-side turbulence. While the gas-effect remains destabilizing in
886 the laminar limit (red curve with open diamond), it switches to stabilizing when turbulence
887 is accounted for (red curve with filled diamond). This is further illustrated in panel 11b,
888 which represents dispersion curves of the linear spatial growth rate for increasing $|Re_G|$ at
889 $Re_L=1.5(5/6) \cot(\phi)$. Thus, turbulence allows to achieve a gas-induced suppression of the
890 Kapitza instability for the current confinement, $H^* \sim 10$ mm, which is much weaker than the
891 confinement studied in Lavallo *et al.* (2019), $H^* \sim 1$ mm, where the gas flow was laminar.
892 And, the counter-current gas flow can render the falling liquid film unconditionally stable to
893 long-wave disturbances at the limit point marked by a filled diamond in panel 11a. However,
894 as we will discover in section 6.2, the film can become unstable to a short-wave instability
895 mode at small ϕ , and the threshold for this mode (dot-dashed curve in panel 11a) lies below
896 the neutral stability bound of the Kapitza instability for the parameters considered here. Thus,
897 the falling liquid film cannot be fully stabilized in this case.

898 Gas-induced stabilization of the Kapitza mode is limited to small inclination angles, and
899 plays no role in our current experiments, where the effect of the counter-current gas flow
900 on the falling liquid film is destabilizing. In this case, it is interesting to determine the AI
901 limit and to confront it with the Re_G range of our experiments. Figure 12 represents WRIBL-
902 OS spatial linear stability predictions for the experimental parameters in figure 10. Upon
903 increasing the counter-current gas flow rate (from circles to crosses), the $-k_i$ versus ω curve
904 in panel 12a, and the c_r versus ω curve in panel 12b, develop a cusp at $Re_G=-5114$. This cusp
905 corresponds to a pinch point in the $-k_i$ versus k_r curve (inset of panel 12a), which indicates
906 the AI limit (Kupfer *et al.* 1987). Thus, the falling liquid film in figure 10 is absolutely
907 unstable from the 5th panel onward, i.e. well before the breakdown of our experiment due to
908 upward-travelling ripples ($Re_G \sim -6800$). Consequently, AI does not seem to play a role in

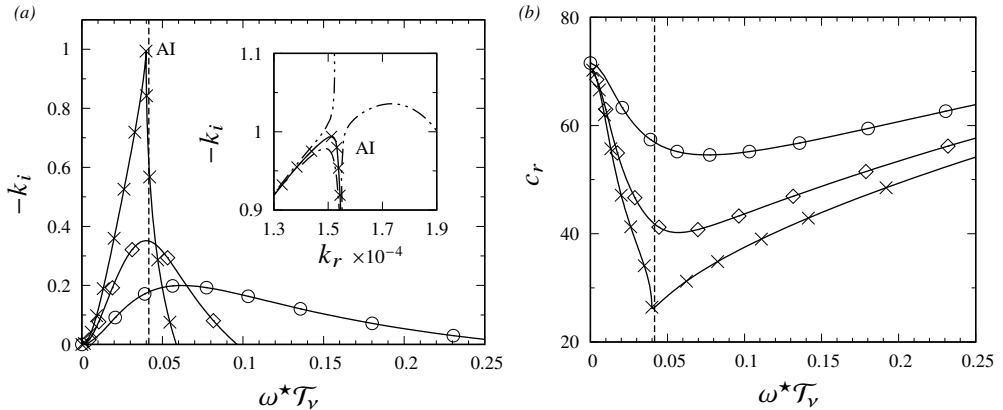


Figure 12: Transition to AI predicted by spatial linear stability analysis with our WRIBL-OS approach. Parameters according to experiment in figure 10: $\text{Ka}=3174$ (water and air I in table 1), $H^*=13$ mm, $\phi=5^\circ$, $\text{Re}_L=43.1$. Circles: $\Pi_\rho=\Pi_\mu=0$ in (3.41). Diamonds: $\text{Re}_G=-4000$, crosses: $\text{Re}_G=-5181$. (a) Growth rate $-k_i$ versus ω . Inset shows $-k_i$ versus k_r . Dot-dashed: $\text{Re}_G=-5180$, dot-dot-dashed: $\text{Re}_G=\text{Re}_G^{\text{AI}}=-5182$; (b) wave speed $c_r=\omega/k_r$. Vertical dashed: forcing frequency $f_0^*=3$ Hz from figure 10. We have rescaled ω with $\mathcal{T}_v=2.207 \times 10^{-3}$ s (3.34).

909 the flooding onset. On the contrary, well-defined downward-travelling Kapitza waves persist
 910 far beyond the AI limit (up to 10th panel in figure 10), and we will discuss the nonlinear
 911 dynamics of these waves in the next subsections.

912 6.1.2. Nonlinear gas-effect: travelling-wave solutions (TWS)

913 We wish to know whether the nonlinear response of the wavy falling liquid film is in line with
 914 the linear gas-effect discussed in the previous section. Figure 13 compares the wave height
 915 (panels 13a, 13c) and wave speed (panels 13b, 13d) of nonlinear TWS obtained from our
 916 WRIBL-LW model at fixed frequency f (solid curves), with experiments (symbols) from our
 917 current work (panels 13a, 13b), where $H^*=13$ mm, and from Kofman *et al.* (2017) (panels
 918 13c, 13d), where $H^*=19$ mm. The experimental wave height data in panel 13a were selected
 919 from film thickness time trace measurements performed over the entire channel length, which
 920 will be discussed in section 6.1.3 (figure 14 there). The wave speed data in panel 13b were
 921 obtained via video image processing from our experiment in figure 10, where Re_L is slightly
 922 different than in panel 13a.

923 Different solid curves in figure 13 correspond to different branches of TWS, which are
 924 associated with different numbers of precursory capillary ripples (CR) and distinguished by
 925 different filled symbols. For the experimental data points, the number of CR is distinguished
 926 via corresponding open symbols. Error bars in panel 13a represent the standard deviation
 927 of experimental film thickness time traces, which increases with increasing $|\text{Re}_G|$ as a result
 928 of wave coalescence events (section 6.1.3). Beyond a certain $|\text{Re}_G|$, coalescence entirely
 929 destroys the coherence of the wave train and comparison with TWS is futile.

930 Overall, our WRIBL-LW predictions in panels 13a, 13b, 13c, and 13d are in reasonable
 931 agreement with the experimental data. Both the gas-effect on the wave height and the wave
 932 speed are captured quantitatively, when accounting for the number of CR.

933 Based on these predictions, we may make the following observations. Downward-traveling
 934 TWS exist far beyond the AI limit, marked by open (WRIBL-LW calculation) and filled
 935 (WRIBL-OS calculation) red arrows in panels 13a and 13c. Below the AI limit, the wave
 936 height h_{max} increases with increasing $|\text{Re}_G|$, while the wave speed mainly decreases. And, we

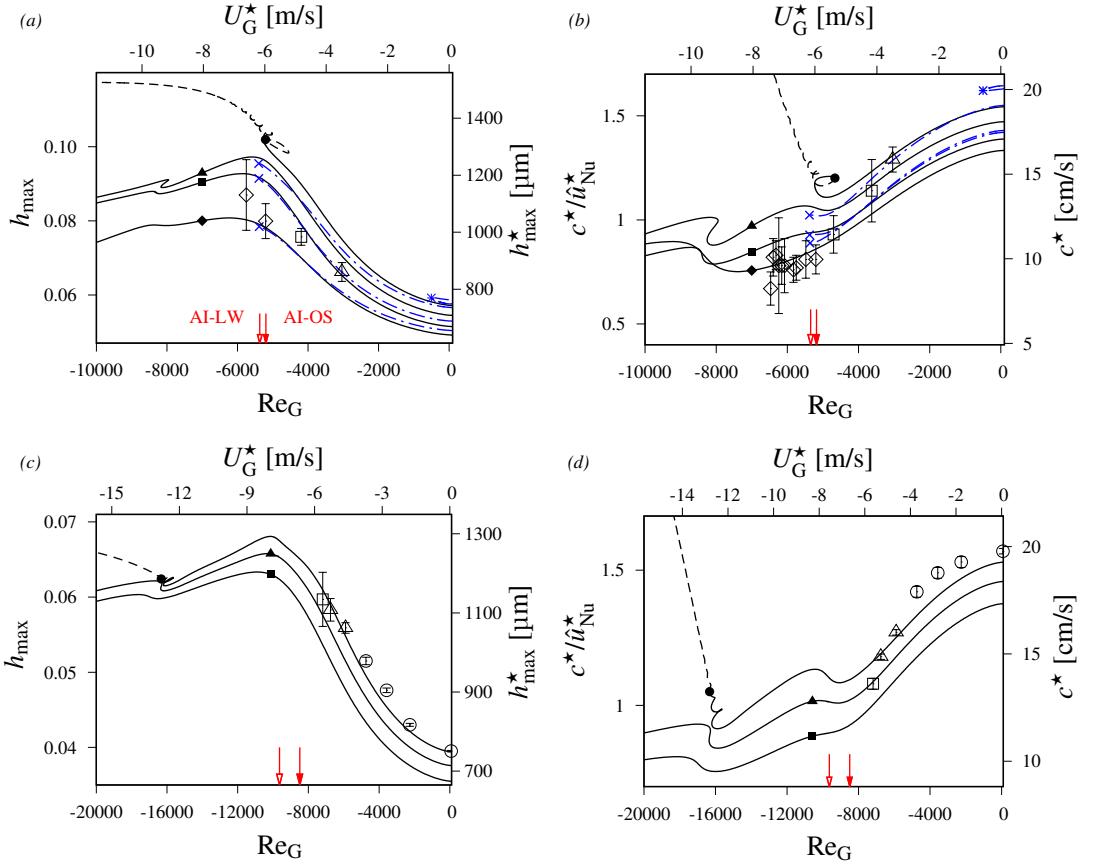


Figure 13: Gas-effect on nonlinear TWS obtained with our WRIBL-LW model (curves) versus experiments (empty symbols). Inclined falling liquid film sheared by counter-current turbulent gas flow: $Ka=3174$ (water and air I in table 1), $\phi=5^\circ$. Filled/open symbols distinguish number of capillary ripples (CR). Diamonds: 0-CR, squares: 1-CR, triangles: 2-CR, circles: 3-CR, dashed: >3 -CR. Solid curves: $f^*=f_0^*$, dot-dashed curves: $f^*=f_{max}^*$. Crosses: AI limit, asterisk: nonlinear LP. Open/filled red arrows mark AI limit obtained from WRIBL-LW/WRIBL-OS. (a,c) Wave height; (b,d) wave speed scaled with $\hat{u}_{Nu}^*=(3/2)q_{L0}^*/h_{Nu}^*$, where $h_{Nu}^*=(3q_{L0}^*\nu_L/g/\sin(\phi))^{1/3}$. (a,b) Versus our experiments: $H^*=13$ mm, $f_0^*=3.0$ Hz. (a) $Re_L=44.2 \pm 0.3$. Filled arrow: $Re_G^{AI}=-5194$, empty arrow: $Re_G^{AI}=-5366$. (b) $Re_L=43.1$; (c,d) versus experiments of Kofman *et al.* (2017): $H^*=19$ mm, $Re_L=45$, $f_0^*=3.05$ Hz. Filled arrow: $Re_G^{AI}=-8490$, empty arrow: $Re_G^{AI}=-9633$.

937 have checked that the relative wave amplitude h_{max}/\bar{h} (not shown here) also increases. Thus,
 938 the non-linear gas-effect is destabilizing, in line with the linear effect discussed in section
 939 6.1.1.

940 For the 0-CR, 1-CR, and 2-CR branches, the h_{max} versus $|Re_G|$ trend in panels 13a and
 941 13c changes beyond the AI limit, i.e. h_{max} now decreases with $|Re_G|$ (except for small non-
 942 monotonous regions). For the 3-CR branches (solid curves with filled circles), the trend
 943 beyond the AI limit is more complicated, i.e. h_{max} first decreases with $|Re_G|$, and then
 944 increases, beyond $|Re_G|=8000$ in panel 13a and beyond $|Re_G|=16000$ in panel 13c. This
 945 increase is associated with the formation of an increasing number of additional capillary
 946 ripples (dashed curve segments) and a strong increase of the wave speed c is observed in

947 panels 13b and 13d, whereas c mostly decreases with $|\text{Re}_G|$ for the other solution branches
 948 (solid curves with filled diamonds, squares, and triangles).

949 Focusing now on the experimental data points (open symbols in panels 13a and 13b), we
 950 observe that the number of CR decreases when increasing $|\text{Re}_G|$ (from open circles to open
 951 diamonds). According to the computations with our WRIBL-LW model (solid curves), this
 952 corresponds to a switching of TWS branches in the direction of lowest wave speed. This is
 953 surprising, because one would expect the fastest TWS to persist in an experiment at fixed
 954 Re_G . Additional effects must thus play a role in the wave selection.

955 In our experiment, saturated waves of fixed frequency f_0^* are formed before entering
 956 into contact with the counter-current gas flow. In panels 13a and 13b we have compared
 957 the gas-effect on such waves, i.e. TWS at $f^*=f_0^*=3$ Hz (solid curves), with TWS at the
 958 linearly most-amplified frequency, i.e. $f^*=f_{\text{max}}^*$ (dot-dashed blue curves). Except for the
 959 3-CR branch (dot-dashed curve with asterisk), both types of TWS behave quite similarly
 960 until the AI limit (where the f_{max}^* branches break down). This is because f_{max}^* does not vary
 961 much with Re_G , and, thus, the forcing frequency f_0^* chosen in the experiment remains close
 962 to f_{max}^* . By contrast, in the case of the 3-CR branch, the most-amplified TWS are lost due
 963 to a nonlinear limit point (filled blue circle), before the gas flow reaches the fully turbulent
 964 regime ($|\text{Re}_G| < 1800$).

965 6.1.3. Nonlinear gas-effect: spatio-temporal wave dynamics

966 In a spatially-evolving falling liquid film, the counter-current gas flow not only acts on
 967 nonlinear Kapitza waves individually, but can trigger interactions between consecutive waves.
 968 Thus, we study the gas-effect on the spatio-temporal dynamics of such waves.

969 Panel 14a summarizes spatial profiles of film thickness data obtained from our experiments
 970 at $\text{Re}_L^{\text{as}}=46$, $\text{Re}_L=44.2 \pm 0.7$, and $f_0^*=3$ Hz, under increasing $|\text{Re}_G|$. Symbols represent the
 971 ensemble average of the wave height h_{max}^* (over at least 100 waves) at a given streamwise
 972 position x^* , and error bars represent the corresponding standard deviation. Filled symbols
 973 identify the TWS data reported in panels 13a and 13b.

974 In the aerostatic configuration (open circles in panel 14a), the error bars are very short,
 975 implying that waves are highly regular in time. However, h_{max}^* varies in space as the result
 976 of the well-known secondary instability discovered by Liu & Gollub (1993).

977 In the counter-current configuration (from diamonds to triangles in panel 14a), we observe
 978 that h_{max}^* in the lower half of the channel ($x^* \gtrsim 50$ cm) significantly increases when $|\text{Re}_G|$ is
 979 increased. On the one hand, this is due to the gas-induced amplification of TWS discussed
 980 in section 6.1.2. On the other hand, the standard deviation of the h_{max}^* data significantly
 981 increases as $|\text{Re}_G|$ is increased. This is the signature of wave coalescence events that can
 982 suddenly increase the wave height. Figure 15 represents a sequence of snapshots illustrating
 983 such an event for $\text{Re}_G=-5200$ (pentagons in panel 14a). The red solid and dashed yellow lines
 984 highlight the fronts of two consecutive waves that eventually coalesce.

985 In panel 14a, we have marked the streamwise position beyond which such coalescence
 986 events become prevalent via check marks on the corresponding error bars. This position,
 987 which we will designate as x_c^* , is determined from the spatial evolution of the frequency
 988 spectrum of h^* , as illustrated in panel 14b for $\text{Re}_G=-5750$ (triangles in panel 14a). We see
 989 that the spectrum evolves from that of a regular wave train, with clear peaks at the forcing
 990 frequency f_0^* and its harmonics (left panel), to a form where the dominant frequency f_{max}^*
 991 is lower than the forcing frequency (right panel). The streamwise locations of the transition,
 992 i.e. where f_{max}^* becomes smaller than f_0^* (middle panel), is defined as x_c^* .

993 Judging by the standard deviation of the h_{max}^* profiles in panel 14a, wave coalescence
 994 becomes more prominent as $|\text{Re}_G|$ is increased. We have seen in panel 13b that the counter-
 995 current gas flow reduces the wave speed of TWS. At fixed wave frequency f^* , this leads to

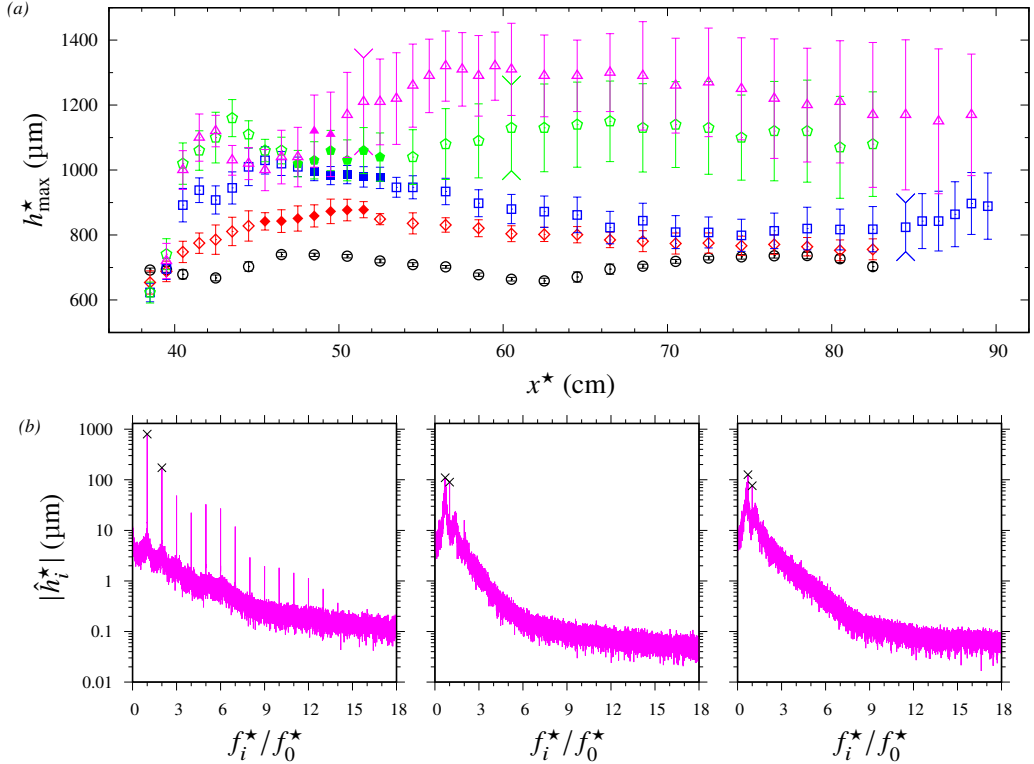


Figure 14: Gas-effect on streamwise evolution of the wavy liquid film. Compilation of our experiments: water/air, $H^*=13$ mm, $\phi=5^\circ$, $\text{Re}_L^{\text{as}}=46$, $\text{Re}_L=44.2\pm 0.3$, $f_0^*=3$ Hz, $\text{Re}_G^{\text{AI}}=-5194$. (a) Ensemble-averaged wave height h_{\max}^* . Error bars represent standard deviation, and check marks mark start of coalescence-dominated region. Filled symbols mark data points used in panel 13a. Circles: aerostatic configuration; diamonds: $\text{Re}_G=-3040$; squares: $\text{Re}_G=-4190$; pentagons: $\text{Re}_G=-5200$; triangles: $\text{Re}_G=-5750$; (b) frequency spectra of the film height h^* : $\text{Re}_G=-5750$. $|\hat{h}_i^*|$ denotes amplitude of Fourier mode with f_i^* . Crosses mark primary and secondary peaks. Left: $x^*=41.5$ cm, middle: $x^*=51.5$ cm, right: $x^*=58.5$ cm.

996 a reduction of the wave separation distance, thus favoring wave interaction and coalescence.
 997 Figure 16 provides a direct comparison of wave trains for two of the experiments from
 998 panel 14a. Panel 16a confronts film thickness time traces measured at $x^*=82.5$ cm for the
 999 aerostatic configuration (solid black curve) and for the counter-current configuration at $\text{Re}_G=-$
 1000 5750 (dashed red curve). Whereas the former represents a regular train of waves responding
 1001 well to the forcing frequency, the latter displays clear signs of coalescence-induced wave
 1002 coarsening, leading to large-amplitude tsunami waves with a wave height much greater than
 1003 the TWS in panel 13a. Panels 16b and 16c represent corresponding frequency spectra for
 1004 the two data sets. Whereas the forcing frequency $f_0^*=3$ Hz is dominant in the spectrum for
 1005 the aerostatic configuration (panel 16b), a lower frequency emerges for the counter-current
 1006 configuration, where periodicity is entirely lost (panel 16c).

1007 In figure 17, we have plotted the starting location x_c^* of the coalescence-dominated region
 1008 versus Re_G , based on all of our experiments for two values of Re_L . The error bars on x_c^*
 1009 correspond to the increment with which the x -position was varied in the experimental runs
 1010 reported in panel 14a. According to figure 17, coalescence is greatly precipitated by the
 1011 (turbulent) counter-current gas flow and this effect is stronger, the lower the liquid flow rate.

1012 The nonlinear wave phenomena discussed in figures 14 to 17 do not seem to be disrupted by

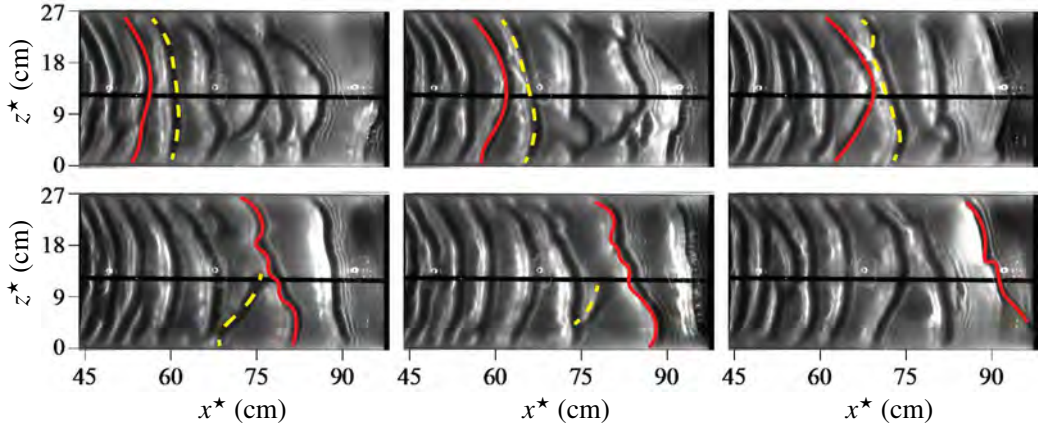


Figure 15: Wave coalescence event. Top view snapshots from our experiment in figure 10 (parameters similar to pentagons in panel 14a): $Re_L=43.1$, $Re_G=-5200$. Time increases from top left to bottom right with an increment of 0.48 s. Solid red and dashed yellow lines highlight two consecutive wave fronts.

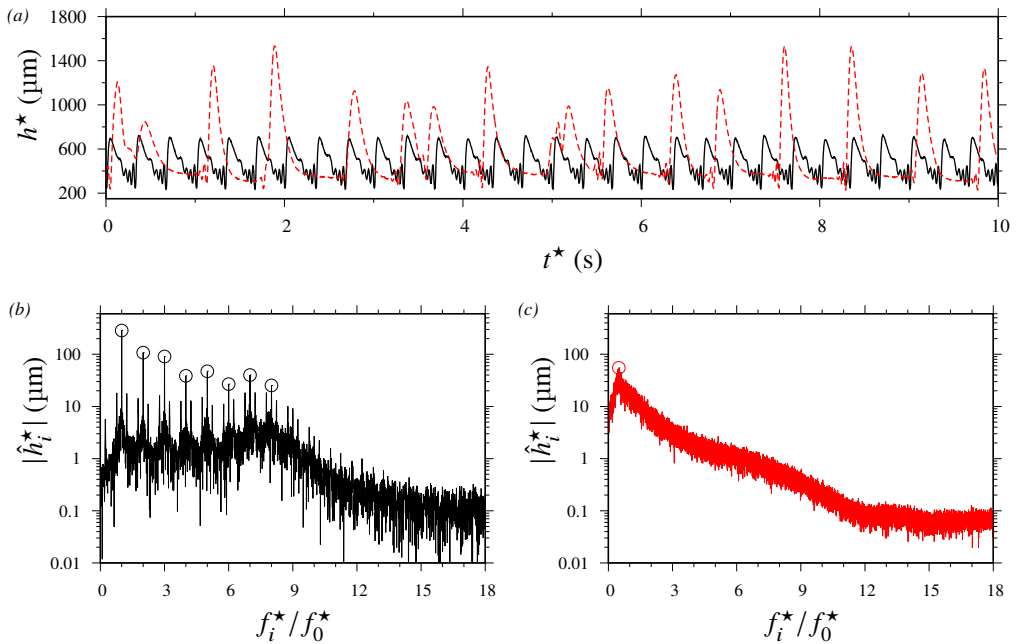


Figure 16: Wave trains for two data sets from panel 14a. (a) Film thickness time traces at $x^*=82.5$ cm. Solid: aerostatic configuration (circles in panel 14a), $Re_L^{as}=46.0$; dashed: counter-current configuration (triangles in panel 14a), $Re_L=44.2$, $Re_G=-5750$; (b,c) corresponding frequency spectra. $|\hat{h}_i^*|$ is the amplitude of the Fourier mode with f_i^* . (b) Aerostatic configuration. Open circles mark peaks at f_0^* and its harmonics; (c) counter-current configuration. Open circle marks global peak at most amplified frequency $f_{max}^*/f_0^*=0.49$.

1013 AI, even though we have considered values of $|Re_G|$ quite far beyond the AI limit, i.e. $Re_G^{AI}=-$
 1014 5194 at $Re_L=44.2$. This is favored by the protected zone used in our experiments, where
 1015 Kapitza waves are allowed to complete their linear and nonlinear growth in a quiescent gas,
 1016 and where the Kapitza instability remains convective. Only after having attained a saturated

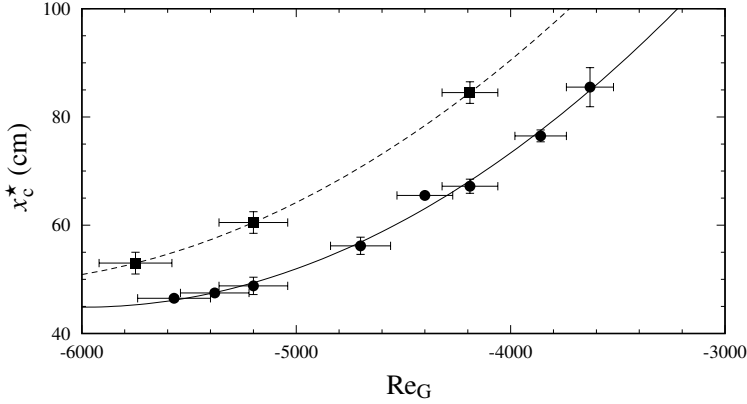


Figure 17: Gas-effect on the starting position x_c^* of the coalescence-dominated region. Compilation of our experiments: water/air, $H^*=13$ mm, $\phi=5^\circ$, $f_0^*=3$ Hz. Circles: $Re_L=32.5 \pm 0.6$, squares: $Re_L=44.3 \pm 0.3$, curves: polynomial fits to guide the eye.

1017 nonlinear state, these waves come into contact with the gas flow, and, consequently, the AI
1018 is bypassed.

1019 Next, we employ open-domain computations with our WRIBL-LW model to study the
1020 linear and nonlinear spatio-temporal evolution of Kapitza waves that feel the gas-effect
1021 from the start. In these computations, the turbulent counter-current gas flow is applied over
1022 the entire domain length. Of course, our WRIBL-LW model can only capture long-wave
1023 instabilities, such as the Kapitza instability, which we focus on in the current section.

1024 We start by studying the gas-effect on the dynamics of naturally-evolving Kapitza waves,
1025 which are more relevant for industrial applications. Here, the liquid flow rate q at the
1026 liquid inlet is subject to a noisy perturbation according to (3.46), with $\varepsilon_1=0$, $\varepsilon_2=5 \times 10^{-5}$.
1027 Figure 18 represents snapshots of our open-domain WRIBL-LW computations for parameters
1028 according to three of the experiments in panel 14a (circles, squares, and triangles there).
1029 In panels 18a (aerostatic configuration) and 18b ($Re_G=-4190$), the AI limit $Re_G^{AI}=-5114$
1030 (obtained from WRIBL-LW model) has not been reached, and we observe the same
1031 phenomena as in our experiments from figure 14. In particular, the counter-current gas
1032 flow exacerbates coalescence events, leading to large-amplitude tsunami waves, which
1033 move very rapidly and absorb numerous smaller waves in their path. This gas-assisted
1034 coarsening dynamics is illustrated in panel 19a, representing a spatio-temporal diagram for
1035 the computation in panel 18b (see also supplementary movie MovieFig18b).

1036 A very different dynamics unfolds when $|Re_G|$ is increased beyond the AI limit, as shown
1037 in panels 18c and 19b, which correspond to $Re_G=-5750$ (see also supplementary movie
1038 MovieFig18c). Here, coalescence events are absent, and a highly regular train of saturated-
1039 amplitude solitary waves develops. The height h_{max} of these waves is significantly smaller
1040 than that of the tsunami waves in panel 18b, thus limiting the risk of flooding. At the
1041 same time, h_{max} is large enough that a significant wave-induced intensification of heat and
1042 mass transport can be expected (Dietze 2019). Thus, AI is not necessarily dangerous in our
1043 configuration. On the contrary, the unbounded linear spatial growth rate associated with
1044 AI represents an effective linear wave selection mechanism that produces highly-regular
1045 nonlinear surfaces waves of the absolute frequency $f_{AI}^*=3.35$ Hz from ambient noise (f_{AI}^*
1046 is obtained from a WRIBL-LW calculation based on panel 12a). Thereby, nonlinear effects,
1047 which set in very close to the liquid inlet, allow the Kapitza waves to travel downstream,
1048 notwithstanding the temporal nature of the linear growth. As far as we know, such a dynamics

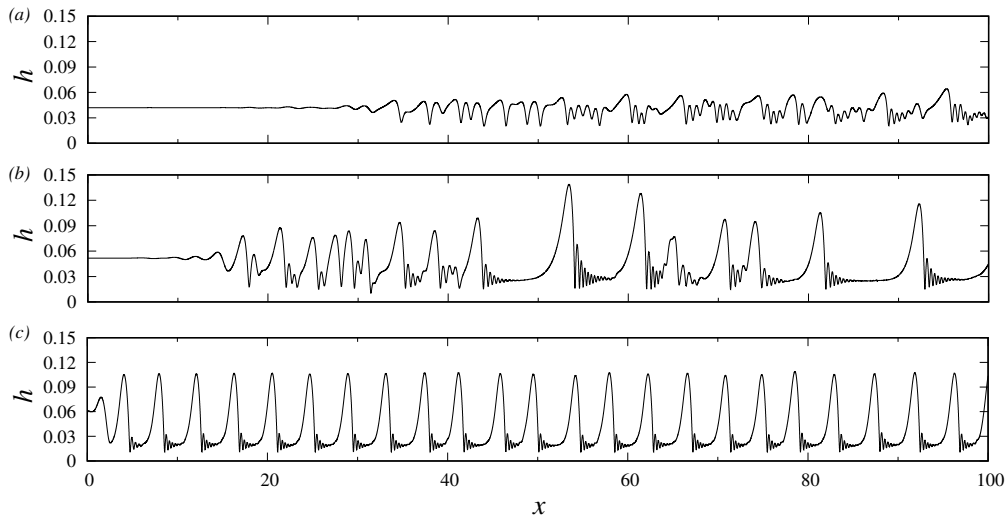


Figure 18: Gas-effect on spatial evolution of naturally-evolving Kapitza waves. Open-domain computations using our WRIBL-LW model on a domain of length $L^*=1.50$ m. The gas flow is applied over the entire domain length. Noisy inlet perturbation according to (3.46): $\varepsilon_1=0$, $\varepsilon_2=5 \times 10^{-5}$. Parameters according to experiments in panel 14a (circles, squares, and triangles there): $Ka=3174$ (water and air I in table 1), $H^*=13$ mm, $\phi=5^\circ$, $Re_L=43.1$. (a) $\Pi_\rho=\Pi_\mu=0$ in (3.6a); (b) $Re_G=-4190$; (c) $Re_G=-5750$. The AI limits, obtained from WRIBL-LW and WRIBL-OS, are $Re_G^{AI}=-5347$ and $Re_G^{AI}=-5182$.

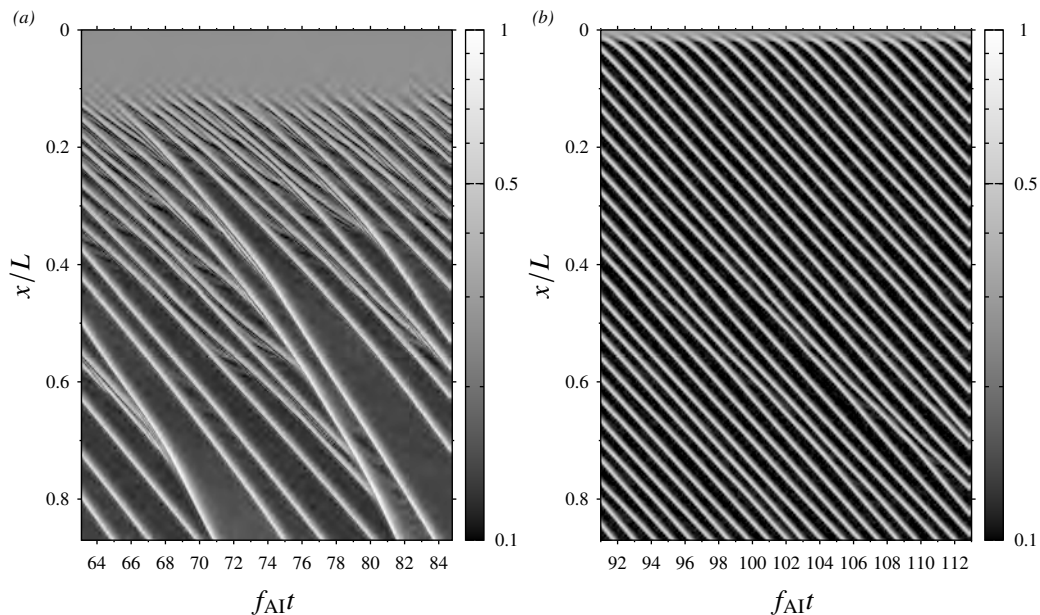


Figure 19: Spatio-temporal diagrams of the normalized film height h/h_{\max} for the computations in panels 18b and 18c. (a) $Re_G=-4190$; (b) $Re_G=-5750$. The AI frequency is $f_{AI}^*=3.35$ Hz, as obtained from linear stability analysis based on our WRIBL-LW model.

1049 has not been shown before, and we have checked that it persists at $Re_G=-6500$ (not shown
 1050 here), i.e. far beyond the value of $|Re_G|$ in panel 19b .

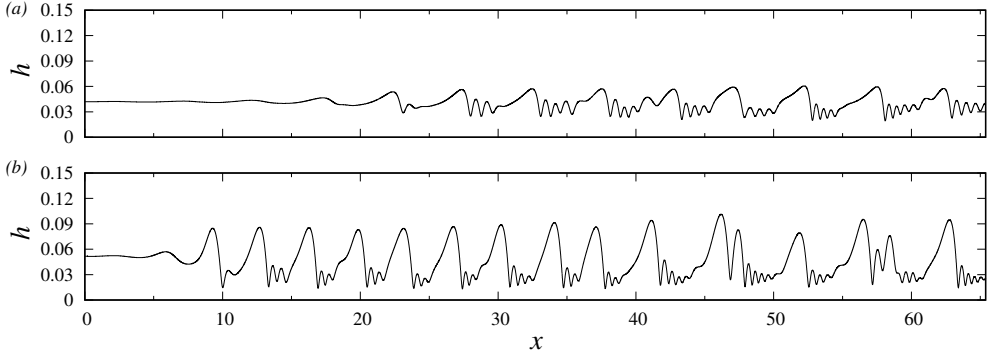


Figure 20: Computations according to panels 18a and 18b, but with additional coherent inlet forcing (3.46): $f_0^* = 3$ Hz, $\varepsilon_1 = 0.01$, $\varepsilon_2 = 5 \times 10^{-5}$. (a) $\Pi_\rho = \Pi_\mu = 0$ in (3.6a); (b) $\text{Re}_G = -4190$.

1051 By contrast, it is very hard to produce a regular wave train below the AI limit via coherent
 1052 inlet forcing. This is demonstrated in figure 20, which represents similar computations to
 1053 figure 18, only that we have additionally applied a harmonic inlet perturbation at frequency
 1054 $f_0^* = 3$ Hz, using $\varepsilon_1 = 0.01$ and $\varepsilon_2 = 5 \times 10^{-5}$ in (3.46). Although the applied coherent forcing
 1055 produces a regular wave train in the aerostatic configuration (panel 20a), coalescence events
 1056 cannot be avoided for $\text{Re}_G = -4190$ (panel 20b). We have not shown the corresponding
 1057 computation beyond the AI limit (see panel 21b for this), because it produces almost exactly
 1058 the same wave train as in panel 18c.

1059 Figure 21 summarizes the wave characteristics of our different WRIBL-LW open-domain
 1060 computations from figures 18 and 20 by plotting the maximum wave height h_{\max} versus the
 1061 streamwise position x . Error bars represent the range of temporal variation of h_{\max} at a given
 1062 position. We see that AI-induced wave selection allows to (1) reduce the maximum wave
 1063 height in the lower portion of the domain by about 40%, and (2) to suppress its variance
 1064 over the entire domain length. For completeness, the pentagons in panel 21b report results
 1065 from our computation with additional coherent inlet forcing for the parameters in panel 18c,
 1066 i.e. beyond the AI limit, evidencing that the wave train is not meaningfully altered by this
 1067 additional forcing.

1068 6.1.4. Standing ripples in a vertically-falling liquid film

1069 Our nonlinear spatio-temporal WRIBL-LW computations in section 6.1.3 did not reveal any
 1070 evidence of the gas-induced oscillatory secondary instability (OI) discovered by Lavalle *et al.*
 1071 (2020) for the configuration of a vertically falling liquid film sheared by a superconfined
 1072 counter-current laminar gas flow. In a spatially evolving regular train of surface waves
 1073 formed by coherent inlet forcing at frequency f_0 , this instability leads to a periodic spatial
 1074 modulation of the wave height, which entails an intensification of mixing.

1075 To check whether this dynamics can be recovered in our current weak-confinement
 1076 setting with a turbulent counter-current gas flow, we perform open-domain WRIBL-LW
 1077 computations for the same liquid-side parameters as in figure 3a of Lavalle *et al.* (2020), i.e.
 1078 $\text{Ka} = 509.5$, $\phi = 90^\circ$, $\text{Re}_L = 15$, and $f_0^* = 16$ Hz. Further, we set $\varepsilon_1 = 0.01$ and $\varepsilon_2 = 0$ in (3.46), and
 1079 we apply the counter-current gas flow over the entire domain length $L^* = 0.84$ m. In terms of
 1080 confinement, we set $H^* = 10$ mm, in contrast to $H^* = 1$ mm used by Lavalle *et al.* (2020). The
 1081 forcing frequency $f_0^* = 16$ Hz corresponds to the linearly most-amplified value in the limit
 1082 ($\Pi_\rho = \Pi_\mu = 0$), which is quite different from the AI frequency $f_{\text{AI}}^* = 26.8$ Hz, as obtained from
 1083 our WRIBL-LW model. We search for signs of the OI by increasing $|\text{Re}_G|$.

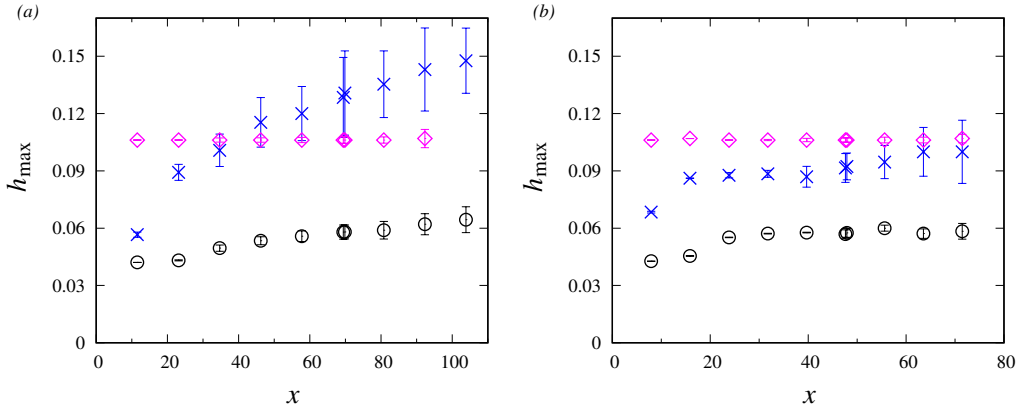


Figure 21: Summary of wave data from our computations in figures 18 and 20. Maximum wave height h_{\max} versus the streamwise location. Circles: $\Pi_\rho = \Pi_\mu = 0$; crosses: $\text{Re}_G = -4190$; diamonds: $\text{Re}_G = -5750$. Naturally-evolving versus forced waves. (a) Noisy inlet perturbation: $\varepsilon_1 = 0$, $\varepsilon_2 = 5 \times 10^{-5}$ in (3.46); (b) additional coherent inlet forcing: $f_0^* = 3.0$ Hz, $\varepsilon_1 = 0.01$, $\varepsilon_2 = 5 \times 10^{-5}$ in (3.46).

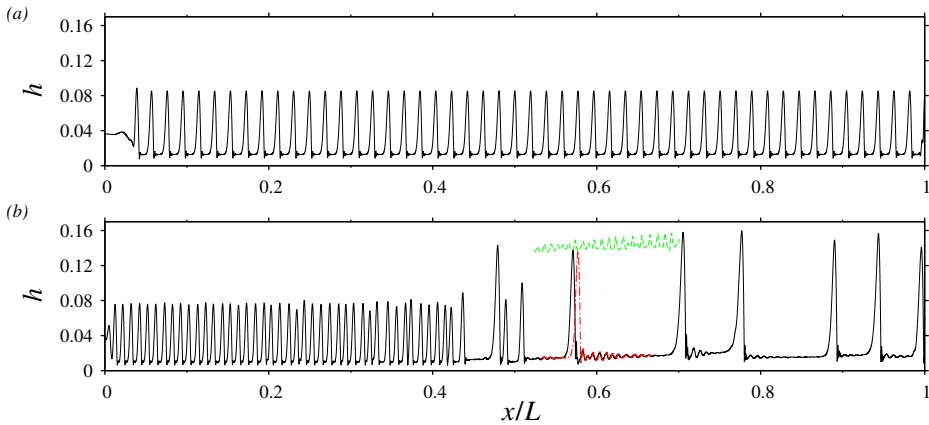


Figure 22: Vertically-falling liquid film sheared by a turbulent counter-current gas flow. Liquid-side conditions according to panel 3a in Lavalle *et al.* (2020): $\text{Ka} = 509.46$ (DMSO-water and air II in table 1), $\text{Re}_L = 15$, $f_0^* = 16$ Hz, $\text{Re}_G^{\text{AI}} = -6500$. WRIBL computation on an open domain of length $L^* = 0.843$ m. Snapshots of the film height profile $h(x)$ at $f_0 t = 61.4$. (a) At AI limit: $\text{Re}_G = \text{Re}_G^{\text{AI}} = -6500$; (b) beyond AI limit: $\text{Re}_G = -7500$. Dot-dashed red: $f_0 t = 61.6$, green dashed: Lagrangian path of a wave crest.

1084 Figure 22 reports results of computations for two values of $|\text{Re}_G|$. The first computation
 1085 (panel 22a) corresponds exactly to the AI limit $\text{Re}_G = \text{Re}_G^{\text{AI}} = -6500$ and represents the same
 1086 features as other computations at lower $|\text{Re}_G|$ (not shown here): an unaltered regular wave
 1087 train of frequency $f = f_0$ persists over the entire domain length.

1088 In the second computation (panel 22b), where the AI limit has been surpassed ($\text{Re}_G = -$
 1089 7500), a more interesting dynamics unfolds. Here, a quite regular wave train of frequency
 1090 $f = f_{\text{AI}}$ emerges near the liquid inlet, as a result of linear wave selection at the AI frequency.
 1091 However, the coherent inlet forcing at frequency f_0 competes with this wave selection, leading
 1092 to a slight perturbation of the wave train, which grows spatially and eventually disrupts the
 1093 wave train. As a result, large-amplitude tsunami waves form due to coalescence events. These
 1094 waves travel extremely fast and absorb all smaller waves travelling in front.

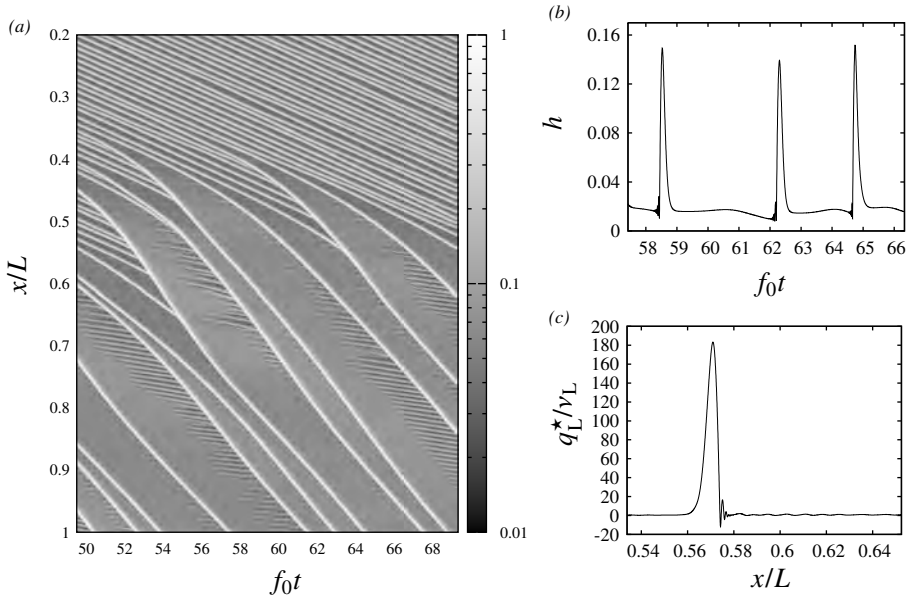


Figure 23: Standing ripples beyond the AI limit $\text{Re}_G^{\text{AI}}=-6500$. Computation from panel 22b: $\text{Re}_G=-7500$. (a) Spatio-temporal diagram of the normalized film height h/h_{\max} ; (b) film height time trace $h(t)$ at $x/L=0.6$; (c) spatial profile of the liquid flow rate $q_L(x)$ at $f_0 t=61.4$.

1095 This gas-induced coarsening dynamics, which is well illustrated by the spatio-temporal
 1096 diagram in panel 23a, leads to long portions of thin residual film in between two consecutive
 1097 tsunami waves. There, the liquid flow rate $q_L(x, t)$ is very small (see q_L profile in panel 23c),
 1098 and thus $|\text{Re}_G|$ is even further beyond the AI limit than for the primary flow q_{L0} . This leads to
 1099 the formation of small-amplitude ripples on the residual film. We call these *standing ripples*
 1100 because they are almost fixed in space, as evidenced by several features in figures 22 and 23.

1101 Firstly, the dot-dashed red profile segment in panel 22b, which corresponds to a slightly
 1102 later time than the main profile, shows no significant translation of the ripples. Secondly,
 1103 the wave fronts of the standing ripples in the spatio-temporal plot in panel 23a are almost
 1104 horizontal. Thirdly, the film height time trace in panel 23b does not show any signature of
 1105 the ripples in between two main wave humps.

1106 The standing ripples are felt like a surface roughness by the tsunami waves propagating
 1107 over the residual film. This leads to a spatial modulation of the film height h_{\max} , similar to
 1108 falling liquid films flowing on a corrugated substrate (Dietze 2019), where they have been
 1109 shown to intensify mixing and inter-phase mass transfer. This modulation is evidenced by
 1110 the dashed green curve in panel 22b, which represents the Lagrangian path of the crest of
 1111 one of the tsunami waves as it propagates through the domain. The absolute nature of the
 1112 standing ripples and their interaction with the large tsunami waves is further illustrated in the
 1113 supplementary movie [MovieFig23](#).

1114 In conclusion, although we have not found any sign of the OI reported by Lavallo *et al.*
 1115 (2020) for our confinement level, we nonetheless observe a similar gas-induced spatial
 1116 modulation of the Kapitza waves, albeit due to an entirely different mechanism.

1117 6.2. Upward-travelling ripples: a new short-wave instability

1118 We now turn to the upward-travelling ripples observed for $|\text{Re}_G| \gtrsim 6200$ in our experiment
 1119 of figure 10 (see last eight panels there). These ripples eventually lead to a breakdown of

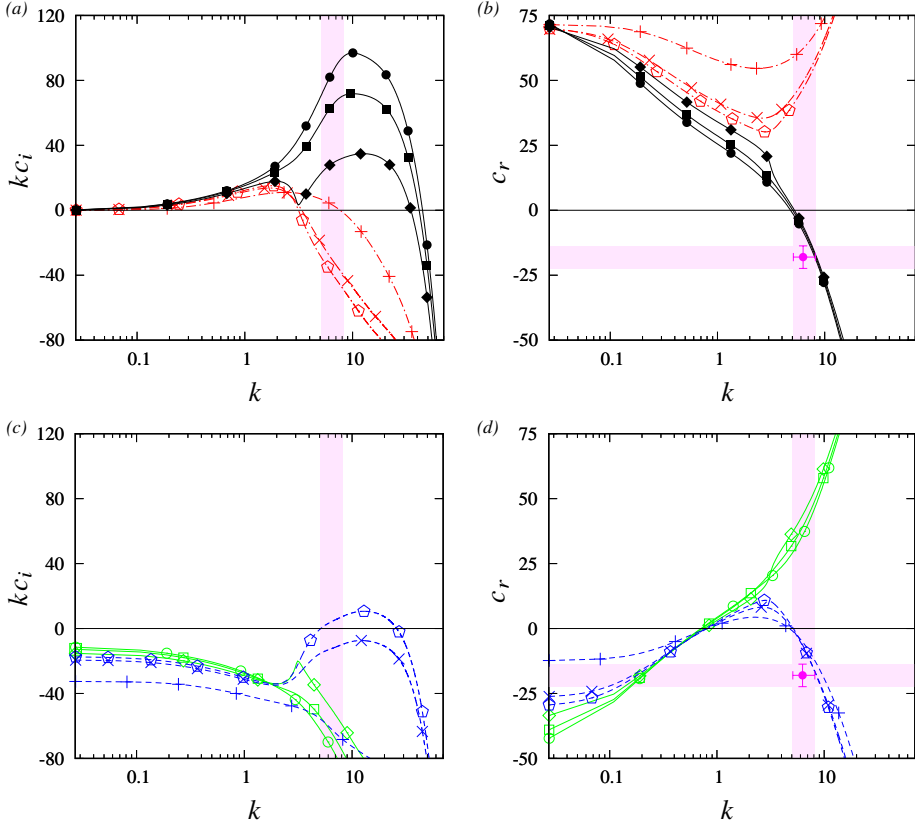


Figure 24: New short-wave instability mode. Falling liquid film sheared by a turbulent counter-current gas flow: $Ka=3174$ (water and air I in table 1), $H^*=13$ mm, $\phi=5^\circ$, $Re_L=43.1$, $Re_G^{AI}=-5182$. Temporal linear stability predictions using the OS-OS approach. Dashed blue: new short-wave mode, dot-dashed red: long-wave Kapitza mode, solid black with filled symbols: unstable merged mode, solid green with open symbols: stable merged mode. Pluses: $\Pi_\rho=\Pi_\mu=0$ in (3.41); crosses: $Re_G=-4700$; pentagons: $Re_G=-5200$; diamonds: $Re_G=-5750$; squares: $Re_G=-6400$; circles: $Re_G=-6760$. (a,c) Growth rate; (b,d) wave speed. Shaded magenta bands and filled magenta circle with error bars represent our experiment from figure 10: $Re_L=43.1$, $Re_G=-6760$, $\Lambda_{ripples}^*=(13 \pm 3)$ mm, $c_{ripples}^*=(-6.2 \pm 1.5)$ cm s $^{-1}$.

1120 our experiment due to the accumulation of liquid droplets in the gas loop, and, thus, can
 1121 be considered as the onset of flooding. In the current section, we seek to identify the origin
 1122 of these ripples via linear stability calculations using our OS-OS approach, which allows to
 1123 capture long- and short-wave instability modes.

1124 Figure 24 represents temporal OS-OS linear stability predictions for parameters from the
 1125 experiment. The different symbols correspond to five different values of Re_G , according
 1126 to the 4th ($Re_G=-4700$), 5th ($Re_G=-5200$), 7th ($Re_G=-5750$), 12th ($Re_G=-6400$), and 17th
 1127 ($Re_G=-6760$) panel in figure 10. The last panel in figure 10 ($Re_G=-6830$) corresponds to the
 1128 breakdown of our experiment, and is not considered here.

1129 Panels 24a and 24c represent growth rate dispersion curves for different instability modes
 1130 and panels 24b and 24d the corresponding dispersion curves for the linear wave speed.
 1131 We have separated the different plots into two panel pairs in order to better distinguish
 1132 the different modes. Red dot-dashed curves in panel 24a belong to the long-wave Kapitza

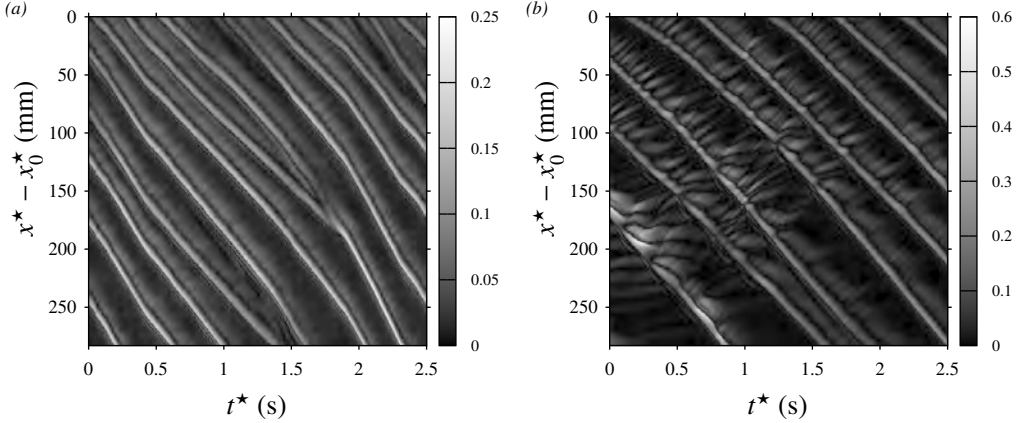


Figure 25: First signature of upward-travelling ripples in our experiments. Spatio-temporal diagrams of the film surface slope $\|\nabla h\|$ for parameters in figure 10, obtained with the synthetic Schlieren technique (Kofman *et al.* 2014): $H^*=13$ mm, $\phi=5^\circ$, $\text{Re}_L=43.1$, $f_0^*=3$ Hz, $x_0^*=48$ cm, $z^*=13$ cm. (a) $\text{Re}_G=-5200$: ripples start to appear in between Kapitza wave humps; (b) $\text{Re}_G=-6080$: ripples deform crests of Kapitza waves.

1133 mode, which we have discussed in section 6.1. The growth rate of this mode increases with
 1134 increasing $|\text{Re}_G|$ (from pluses to pentagons), while its cut-off wave number decreases.

1135 The blue dashed curves in panel 24c belong to a new short-wave instability mode, which
 1136 emerges upon increasing $|\text{Re}_G|$ beyond $|\text{Re}_G|=4837$ (between crosses and pentagons). We
 1137 call this new instability mode a short-wave mode, because the growth rate kc_i is positive
 1138 only within a finite span of the wavelength $\Lambda=2\pi/k$, and because the maximum growth rate
 1139 is observed at a large wave number, i.e. $k_{\max}\sim 10$ versus $k_{\max}\sim 2$ for the long-wave Kapitza
 1140 instability mode. The short-wave mode appears for $|\text{Re}_G|\gg 1800$, and this suggests that
 1141 turbulence in the gas is required to generate this instability mode. This may explain why
 1142 previous stability investigations (Schmidt *et al.* 2016; Trifonov 2017), where the gas flow
 1143 was assumed laminar, did not find the short-wave mode.

1144 At $\text{Re}_G=-5200$ (pentagons in figure 24), the growth rate of the short-wave mode (panel
 1145 24c) has surpassed that of the Kapitza mode (panel 24a). However, our experiments in figure
 1146 10 do not show any clear signature of the short-wave mode, except maybe slight modulations
 1147 on the crests of the first two wave fronts (see e.g. 8th panel in figure 10). This can be
 1148 attributed to the protected zone in our current experimental setup, where Kapitza waves are
 1149 allowed to develop in a virtually quiescent atmosphere, before entering the gas-sheared zone.
 1150 In other words, the gas-induced short-wave instability mode has to compete with saturated
 1151 fully-nonlinear Kapitza waves. We demonstrate this via an additional set of experiments that
 1152 was focused on detecting the first signs of ripples for the parameters in figure 10. Figure 25
 1153 shows spatio-temporal diagrams of the film surface slope obtained from these experiments,
 1154 using the synthetic Schlieren technique (Moisy *et al.* 2009; Kofman *et al.* 2014). In panel
 1155 25a, $\text{Re}_G=-5200$, wave fronts of upward-travelling ripples are clearly visible in between
 1156 downward-travelling Kapitza waves. However, these ripples cannot yet compete with the
 1157 large-amplitude Kapitza wave humps, and thus remain hidden in the dark inter-wave regions
 1158 of figure 10.

1159 Upon increasing Re_G further (diamonds in figure 24), the short-wave mode and the Kapitza
 1160 mode merge into a new unstable merged mode (open diamonds in panel 24a), which initially
 1161 displays a two-humped growth rate dispersion curve, and a new stable merged mode (filled
 1162 diamonds in panel 24c). Panel 26a shows the merging of the growth rate curves in detail.
 1163 According to this, the long-wave portion of the long wave mode (red dot-dashed curves)

1164 merges with the short-wave portion of the short-wave mode (blue dashed curves), creating
 1165 the unstable merged mode (solid black curve with filled diamonds). Vice versa, the short-
 1166 wave portion of the long-wave mode merges with the long-wave portion of the short-wave
 1167 mode, creating the stable merged mode (solid green curve with open diamonds).

1168 A direct consequence of the mode merging is a change in trend of the cut-off wave number
 1169 k_c versus Re_G when considering the growth rate curves originating at $k=0$, $kc_i=0$ in panel
 1170 24a. Before the merging (pluses to pentagons), these curves are associated with the long-wave
 1171 Kapitza instability, and k_c decreases with increasing $|\text{Re}_G|$. After the merging (diamonds to
 1172 circles), k_c jumps to a much greater value and its trend is reversed. This could explain the
 1173 sudden change in trend of the neutral stability bounds in figure 11 of Vellingiri *et al.* (2015),
 1174 which we have reproduced with our WRIBL-OS approach in panel 29a of appendix A.

1175 As $|\text{Re}_G|$ is increased beyond $|\text{Re}_G|=5750$ in panel 24a (from diamonds to circles), the
 1176 short-wave growth rate maximum of the unstable merged mode becomes dominant and
 1177 attains very large values. It is here that upward-travelling ripples become strong enough to
 1178 deform the crests of the Kapitza waves (see panel 25b), and thus become clearly visible
 1179 in our experiments (last eight panels of figure 10). The shaded magenta band in panel 24a
 1180 represents the experimental range of the wave number k for these ripples at $\text{Re}_G=-6760$
 1181 (next to last panel in figure 10), and this compares reasonably well with the most-amplified
 1182 wave number k_{max} of the corresponding unstable merged mode (curve with filled circles in
 1183 figure 24a). Better agreement is expected without the protected region used in our current
 1184 experimental setup. In our setup, short-wave ripples originate on the residual film in between
 1185 two preexisting large-amplitude nonlinear Kapitza waves, which is not quite comparable to
 1186 the primary flow underlying figure 24.

1187 The most important feature of the new short-wave instability mode observed in panels 24c
 1188 and 24d is that it displays negative wave speeds ($c_r < 0$ in panel 24d) in the range of unstable
 1189 wave numbers. And, this property is endowed to the unstable merged mode in panel 24b. In
 1190 particular, the linear wave speed c_r for $\text{Re}_G=-6760$ (solid curve with open circles in panel
 1191 24b) is negative across the entire wave number span of the upward-travelling ripples observed
 1192 in the corresponding experiment (vertical shaded magenta band in panel 24b). Moreover,
 1193 the ripple wave speed estimated from our experiments (filled magenta circle with error bars
 1194 in panel 24b) agrees quite well with the linear wave speed. Thus, we are confident that the
 1195 short-wave instability uncovered in figure 24 is at the origin of the upward-travelling ripples
 1196 observed in our experiment of figure 10.

1197 Upward travelling linear waves linked to the short-wave mode, or the unstable merged
 1198 mode, do not necessarily require a negative liquid velocity. This is shown in panel 26b,
 1199 where we have plotted the primary-flow liquid velocity at the liquid-gas interface $u_{L0}|_{y=h_0}$
 1200 in terms of Re_G for the liquid-side parameters from figure 24. Here, we confront our current
 1201 confinement (solid curve with symbols, $H^*=13$ mm) with those of Kofman *et al.* (2017)
 1202 (dot-dashed, $H^*=19$ mm) and Mergui *et al.* (2023) (dashed, $H^*=5$ mm). Focusing on the
 1203 solid curve, where symbols mark $|\text{Re}_G|$ values from panels 24b and 24d, we see that $u_{L0}|_{y=h_0}$
 1204 becomes negative far beyond the onset of the short-wave instability (between the square and
 1205 circle in panel 26b). Thus, the gas-induced linear short waves can travel upward even though
 1206 the liquid moves downward across the entire film thickness h_0 .

1207 To further characterize the nature of the short-wave instability mode, figure 27 represents
 1208 (normalized) profiles of the liquid-side (panel 27a) and gas-side (panel 27b) eigenfunctions,
 1209 ϕ and ψ (4.13), for the most-amplified long-wave (red dot-dashed curves) and short-wave
 1210 (blue dashed curves) instability modes at $\text{Re}_G=-5200$ (pentagons in panels 24a and 24c).
 1211 We see that ϕ is maximal at the liquid gas interface, $y=h_0$, for both the long-wave and
 1212 short-waves modes. We may thus conclude that the short-wave mode is an interfacial mode,

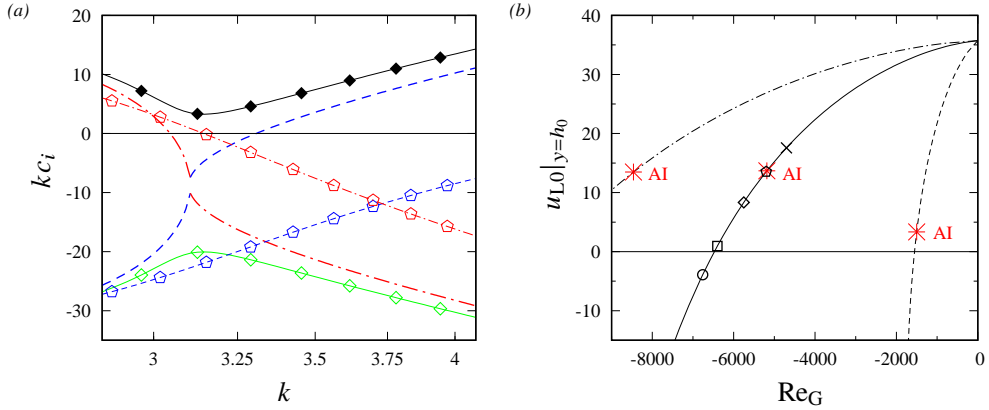


Figure 26: Details of OS-OS linear stability predictions from figure 24: $Ka=3174$, $Re_L=43.1$, $H^*=13$ mm, $\phi=5^\circ$. (a) Merging between the short-wave and long-wave instability modes from panels 24a and 24c. Diamonds: $Re_G=-5750$, thick lines without symbols: -5680 , pentagons: -5200 ; (b) primary-flow liquid velocity at the film surface. Solid: $H^*=13$ mm, $Re_G^{AI}=-5182$; dot-dashed: $H^*=19$ mm, $Re_G^{AI}=-8461$; dashed: $H^*=5$ mm, $Re_G^{AI}=-1501$. Asterisks indicate AI limit from WRIBL-OS spatial linear stability calculations.

1213 strengthening our assertion that it lies at the origin of the upward-travelling ripples observed in
 1214 our experiments.

1215 Interestingly, the onset of the short-wave instability mode in panel 24c, i.e. $Re_G=-5100$
 1216 (between crosses and pentagons), is very close to the AI limit of the Kapitza instability
 1217 observed in figure 12, i.e. $Re_G^{AI}=-5115$. This may explain why flooding predictions based on
 1218 the AI limit (Vellingiri *et al.* 2015) are reasonably good, even though AI does not seem to
 1219 produce any dangerous events in our experiments and nonlinear WRIBL-LW computations.

1220 7. Conclusion

1221 We have studied the effect of a confined turbulent counter-current gas flow on the linear and
 1222 nonlinear dynamics of a wavy falling liquid film, focusing on regimes beyond the absolute
 1223 instability (AI) limit of the Kapitza instability. We have done this via experiments and
 1224 numerical computations based on a new low-dimensional model, which we have introduced
 1225 and validated here. This model accurately captures the gas-induced transition to AI as well as
 1226 the nonlinear gas-effect on travelling Kapitza waves. In addition, we have performed linear
 1227 stability calculations based on the full Orr-Sommerfeld equations in the gas and the liquid.

1228 From our investigation, we may draw the following conclusions. (1) AI is not necessarily
 1229 dangerous, i.e. no flooding events linked to Kapitza waves were observed even far beyond
 1230 the AI limit. On the contrary, AI can act as an effective linear wave selection mechanism
 1231 in a naturally evolving falling liquid film, leading to highly regular downward-travelling
 1232 nonlinear waves, precluding dangerous coalescence events.

1233 (2) Flooding is eventually triggered by upward-traveling ripples, which were discovered
 1234 in the experiments of Kofman *et al.* (2017) and reproduced here. We find that these ripples
 1235 result from a short-wave interfacial instability associated with a negative linear wave speed.
 1236 As far as we know, this short-wave instability has not yet been reported in the literature. On
 1237 the contrary, the instability was not found in several previous stability investigations of falling
 1238 liquid films (Schmidt *et al.* 2016; Trifonov 2017). In these investigations, the counter-current
 1239 gas flow was assumed laminar, even though the gas Reynolds number Re_G was increased
 1240 far beyond the turbulence threshold. We may thus surmise that Reynolds stresses associated

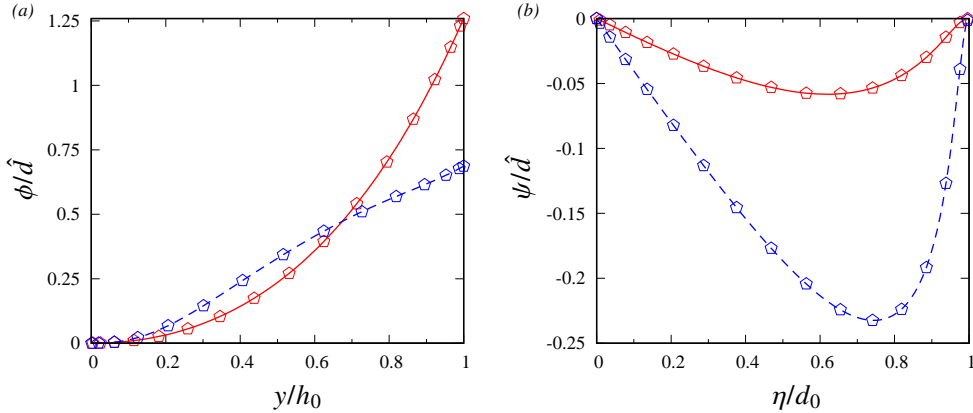


Figure 27: Eigenfunctions (4.13) for different instability modes from figure 24. Turbulent counter-current gas flow: $\text{Re}_G=5200$. Linearly most-amplified short-wave (dashed blue lines, $k=12.8$) and long-wave (solid red lines, $k=1.6$) instability modes. (a) Liquid film, ϕ ; (b) gas layer, ψ .

1241 with gas-side turbulence are essential for generating the short-wave instability, at least in the
 1242 parameter range where ripples are observed experimentally.

1243 (3) The onset of the short-wave instability approximately coincides with the AI limit
 1244 of the long-wave Kapitza instability. This could explain why predictions of the flooding
 1245 threshold based on the AI limit have been found to agree reasonably well with experiments
 1246 (Vellingiri *et al.* 2015), even though the trends of these two thresholds w.r.t. to the liquid
 1247 Reynolds number are opposed.

1248 (4) At larger counter-current gas flow rates, the short-wave instability mode merges with
 1249 the long-wave Kapitza mode, leading to a sudden and drastic increase of the cut-off wave
 1250 number. This may explain the sudden change in the θ -trend of the neutral stability curves
 1251 reported in figure 11 of Vellingiri *et al.* (2015), which we have reproduced in figure 29a
 1252 based on our own computations.

1253 (5) Absolute instability of the long-wave Kapitza mode and instability of the new short-
 1254 wave mode can coincide in a certain parameter range (see panels 12a and 24c). It remains
 1255 to be seen, how downward-travelling long waves generated by AI interact/compete with
 1256 upward-travelling ripples generated by the short-wave instability in a naturally evolving
 1257 falling liquid film. Unraveling the interaction between these two wave types, may be the key
 1258 to understanding flooding in gas-sheared falling liquid films. In our current experiments, this
 1259 could not be studied, as fixed-frequency saturated-amplitude nonlinear waves were allowed
 1260 to develop in a protected region, before entering into contact with the counter-current gas
 1261 flow. In this configuration, Kapitza waves are privileged until the growth rate of the merged
 1262 instability mode (panel 24a) becomes dominant and upward-travelling ripples appear.

1263 Conversely, computations with our current WRIBL-LW model cannot capture the new
 1264 short-wave instability. Although this is a limitation of the model, it allowed us to show that the
 1265 long-wave AI alone does not produce any catastrophic events. An interesting goal for future
 1266 work is to extend our model to overcome this limitation. For this, the gas-side representation,
 1267 which currently relies on an $O(\epsilon)$ long-wave approximation, needs to be improved. This will
 1268 require relaxing our symmetry condition (3.13b). Velocimetry experiments similar to those
 1269 of Cohen & Hanratty (1968), would allow to gauge the extent of asymmetry in the gas flow.

1270 By contrast, our $O(\epsilon^2)$ liquid-side WRIBL representation is capable of capturing short
 1271 waves, as evidenced by the precursory capillary ripples in figure 9, which have a smaller
 1272 wavelength than the upward-travelling ripples. Also, our comparisons between WRIBL-OS

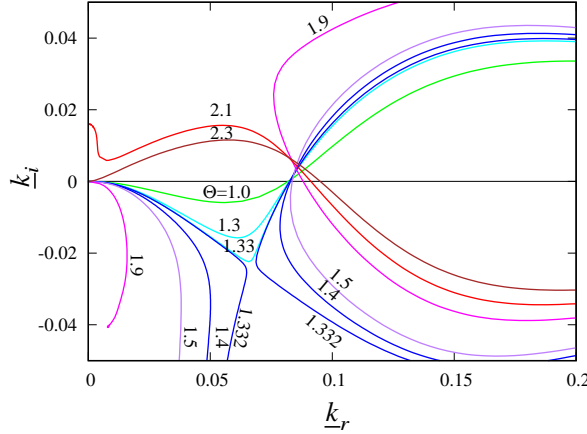


Figure 28: Validation of our WRIBL-OS approach (section 4.1). Spatial linear stability predictions for parameters in figure 15 of Vellingiri *et al.* (2015): $Ka=2000$ (methanol and helium in table 1), $\phi=90^\circ$, $Re_0=3Re_L/\sin(\phi)=10$, $H^*=30$ mm, $\Pi_\rho=0$, (3.6a) truncated at $O(\epsilon)$. Quantities are scaled with $\underline{\mathcal{L}}=h_0^*$ and $\underline{\mathcal{U}}=h_0^{*2}g \sin(\phi)/2\nu_L$. The counter-current gas shear stress is quantified via $\Theta=T_{G0}^*|\underline{\mathcal{L}}/\mu_L/\underline{\mathcal{U}}$.

1273 and OS-OS linear stability calculations show good agreement (figures 6), including for the
1274 short wave mode (figure 30).

1275 Finally, a detailed study of the new short-wave instability is necessary, and we intend to
1276 pursue our work in this direction. For example, it should be verified whether the instability
1277 also occurs for the conditions studied by Trifonov (2017) and Schmidt *et al.* (2016). And, the
1278 mechanism of the instability should be elucidated. For example, how does it compare to the
1279 Kelvin-Helmholtz instability and the generation of wind-driven waves?

1280 Appendix A. Validation of WRIBL-OS and OS-OS approaches

1281 In figure 28, we have used our WRIBL-OS approach from section 4.1 to reproduce the
1282 growth rate dispersion curves obtained from temporal linear stability analysis in figure
1283 15 of Vellingiri *et al.* (2015), for a vertically-falling liquid film sheared by an unconfined
1284 counter-current turbulent gas flow. To recover the formulation used in that reference, we have
1285 truncated our liquid-side WRIBL model (3.6a) at $O(\epsilon)$, set $\Pi_\rho=0$, and increased H^* until
1286 it no longer affected our results. All quantities in figure 28 have been scaled with $\underline{\mathcal{L}}=h_0^*$
1287 and $\underline{\mathcal{U}}=h_0^{*2}g \sin(\phi)/2\nu_L$, according to Vellingiri *et al.* (2015). Thus, results are directly
1288 comparable with data in figure 15 of that reference, exhibiting very good agreement.

1289 In figure 29, we have used our OS-OS approach from section 4.2 to reproduce several
1290 temporal linear stability predictions from Vellingiri *et al.* (2015) and Schmidt *et al.* (2016). In
1291 panel 29a, we have reproduced the neutral stability predictions in figure 11 of Vellingiri *et al.*
1292 (2015), where a vertically-falling liquid film sheared by an unconfined turbulent counter-
1293 current gas flow was considered. Crosses correspond to our OS-OS prediction and open
1294 circles to calculations of Vellingiri *et al.* (2015). In the same figure, we have also plotted
1295 predictions obtained from our WRIBL-OS approach (curves). To reproduce the unconfined
1296 configuration considered in Vellingiri *et al.* (2015), we have once again increased H^* until
1297 it no longer meaningfully affected our results.

1298 Agreement between crosses and circles in panel 29a is good, except for data at
1299 $\Theta=T_{G0}^*\underline{\mathcal{L}}/\mu_L/\underline{\mathcal{U}}=3$. This is where the trend of the cut-off wave number k in terms of the

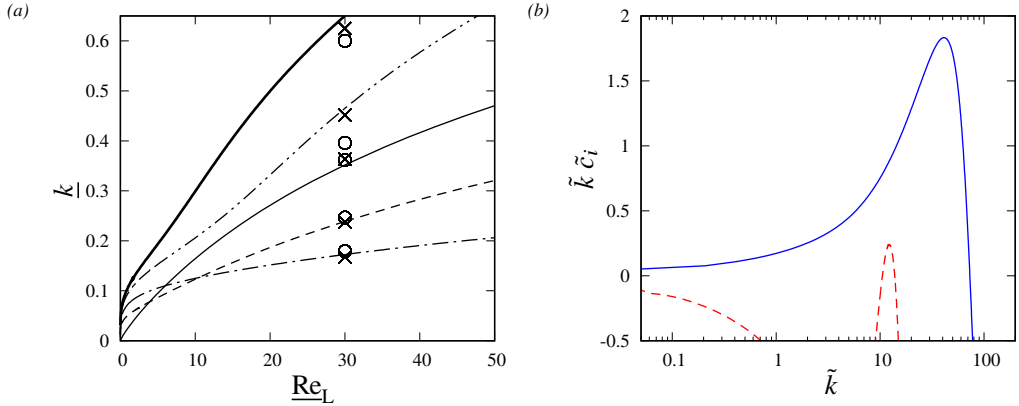


Figure 29: Validation of our WRIBL-OS (section 4.1) and OS-OS (section 4.2) approaches. Temporal linear stability predictions for a gas-sheared vertically-falling liquid film. (a) Neutral stability curves for parameters according to figure 11 in Vellingiri *et al.* (2015): $Ka=2000$, $H^*=300$ mm. Crosses: OS-OS; solid lines: WRIBL-OS; open circles: data from Vellingiri *et al.* (2015). Thin solid: $\Theta=0$; dashed: $\Theta=1$; dot-dashed: $\Theta=2$; dot-dot-dashed: $\Theta=3$; thick solid: $\Theta=3.5$. Same scaling as in figure 28; (b) growth rate dispersion curves for parameters according to panel 4e in Schmidt *et al.* (2016): $H^*=10$ mm, $\rho_L=1000$ kg/m³, $\mu_L=0.5 \times 10^{-3}$ Pa s, $\rho_G=1$ kg/m³, $\mu_G=1 \times 10^{-6}$ Pa s, $\sigma=1$ mN m⁻¹, $\delta_L=h_0^*/H^*=0.08$, $\tilde{Fr}=\tilde{U}/\sqrt{g\tilde{L}}=3$, $Re_L=6166$, $Re_G=48322$. Tildes indicate scaling with $\tilde{L}=H^*$ and $\tilde{U}=[\partial_x P_{G0}^* H^*/\rho_G]^{1/2}$. Solid blue: long-wave Kapitza mode; dashed red: short-wave Tollmien-Schlichting mode.

1300 dimensionless gas shear stress Θ changes. We believe that this is the result of the mode
 1301 merging that we have observed in section 6.2. At thresholds where the stability behavior
 1302 changes, large discrepancies between two calculations may occur as a result of small
 1303 differences between the employed procedures. In particular, we have used a different set
 1304 of curvilinear coordinates than Vellingiri *et al.* (2015). We believe that this explains the
 1305 discrepancy between the cross and circle for $\Theta=3$.

1306 Interestingly, we have observed that our OS-OS predictions in panel 29a change signifi-
 1307 cantly when setting $\Pi_\rho=0$ (not shown). This confirms our conclusion based on equation (5.5)
 1308 that P_G can affect stability even in the unconfined limit.

1309 In panel 29b, we have reproduced with our OS-OS approach the growth rate dispersion
 1310 curves in figure 4e of Schmidt *et al.* (2016), where a vertically-falling liquid film sheared by a
 1311 confined laminar ($\tilde{l}_t=0$ in equations 3.27 and 3.28) counter-current gas flow was considered.
 1312 All quantities have been scaled with $\tilde{L}=H^*$ and $\tilde{U}=[\partial_x P_{G0}^* H^*/\rho_G]^{1/2}$, according to
 1313 Schmidt *et al.* (2016). Thus, results are directly comparable with data in figure 4e of that
 1314 reference, exhibiting very good agreement, both for the long-wave Kapitza mode (solid blue
 1315 curve) and the Tollmien-Schlichting mode (dashed red curve).

1316 Appendix B. Neutral stability bound based on equation (5.2)

1317 In (5.2), we have introduced the first-order contribution c_1 , arising in the long-wave expansion
 1318 ($k \rightarrow 0$) of the linear wave speed c :

$$1319 \quad c = c_0 + kc_1 + O(k^2),$$

$$1320 \quad c_1 = i\mathcal{R}.$$

1321 The neutral stability bound is given by $\mathcal{R}=0$, and the solution for \mathcal{R} obtained from our
1322 WRIBL-LW model (3.6) is:

$$\begin{aligned}
1323 \quad \mathcal{R} = & \frac{1}{3} \cos(\phi) \frac{\text{Re}_L}{\text{Fr}^2} h_0^3 \left\{ -1 + \frac{\Pi_\rho}{\Pi_u^2} \right\} & (B 1) \\
1324 \quad & + \frac{\sin^2(\phi)}{\text{Fr}^4} \text{Re}_L^3 \left\{ \frac{2}{15} h_0^6 + \frac{2}{5} \frac{\Pi_\rho^2}{\Pi_u^4} \frac{h_0^8}{d_0^2} + \frac{10}{21} \frac{\Pi_\rho}{\Pi_u^2} \frac{h_0^7}{d_0} \right\} \\
1325 \quad & + \Pi_\mu \frac{\sin(\phi)}{\text{Fr}^2} \text{Re}_L^2 T_{G0} \left\{ \frac{\Pi_\rho}{\Pi_u} \left[\frac{7}{24} \frac{h_0^6}{d_0} + \frac{4}{5} \frac{h_0^7}{d_0^2} \right] + \Pi_u \left[\frac{2}{15} h_0^5 + \frac{10}{21} \frac{h_0^6}{d_0} \right] \right\} \\
1326 \quad & + \Pi_\mu^2 \Pi_u^2 \text{Re}_L T_{G0}^2 \left\{ \frac{7}{24} \frac{h_0^5}{d_0} + \frac{2}{5} \frac{h_0^6}{d_0^2} \right\} \\
1327 \quad & - \Pi_\mu \Pi_\rho \frac{\text{Re}_L}{\text{Re}_G} \Pi_u^3 T_{G0} \partial_x P_{G0} \left\{ \frac{2}{15} h_0^5 + \frac{43}{56} \frac{h_0^6}{d_0} + \frac{4}{5} \frac{h_0^7}{d_0^2} \right\} \\
1328 \quad & - \frac{\sin(\phi)}{\text{Fr}^2} \frac{\text{Re}_L^3}{\text{Re}_G} \partial_x P_{G0} \left\{ \Pi_\rho^2 \left[\frac{10}{21} \frac{h_0^7}{d_0} + \frac{4}{5} \frac{h_0^8}{d_0^2} \right] + \Pi_\rho \Pi_u^2 \left[\frac{4}{15} h_0^6 + \frac{10}{21} \frac{h_0^7}{d_0} \right] \right\} \\
1329 \quad & + \frac{\text{Re}_L^3}{\text{Re}_G^2} \Pi_\rho^2 \Pi_u^2 \partial_x P_{G0}^2 \left\{ \frac{2}{15} h_0^6 + \frac{10}{21} \frac{h_0^7}{d_0} + \frac{2}{5} \frac{h_0^8}{d_0^2} \right\} \\
1330 \quad & + \frac{1}{2} \Pi_\mu \Pi_u \frac{h_0^2}{d_0} \partial_\eta U_1|_{d_0} + \frac{1}{3} \Pi_\rho \Pi_u^2 \text{Re}_L \frac{h_0^3}{d_0} C_1, \\
1331
\end{aligned}$$

1332 where C_1 and U_1 are obtained by solving (3.27) and (3.28). Solutions for C_1 and $\partial_\eta U_1|_{d_0}$ in
1333 the laminar limit are given in (5.5).

1334 Appendix C. Accounting for derivatives of T_G and P_G in (3.6a)

1335 We check to what extent the temporal and spatial derivatives of T_G and P_G , which appear in
1336 (3.6a) and which we have neglected in our WRIBL-LW and WRIBL-OS computations, play
1337 a role in the linear stability of a gas-sheared falling liquid film. Figure 30 represents linear
1338 stability predictions obtained with three approaches for conditions according to figure 24.
1339 Solid curves correspond to OS-OS calculations based on (4.20) and (4.21), dot-dashed curves
1340 to WRIBL-OS calculations based on (3.41), and dashed curves to WRIBL-OS calculations
1341 with account of the space and time derivatives of T_G and P_G in (3.6a).

1342 According to this, both WRIBL approaches accurately capture the gas-effect on the long-
1343 wave Kapitza instability mode (red curves in panel 30a), and accounting for the derivatives
1344 of T_G and P_G does not bear much benefit. By contrast, not surprisingly, the growth rate of
1345 the new short-wave mode is less well predicted by both WRIBL approaches (blue curves in
1346 panel 30a). Here, accounting for the derivatives of T_G and P_G (dashed blue curve) improves
1347 predictions at intermediate k , but the standard WRIBL-OS approach performs better at large
1348 k . Finally, both WRIBL approaches produced quite good predictions of the merged instability
1349 mode (panel 30b), whereby the standard WRIBL-OS approach behaves better.

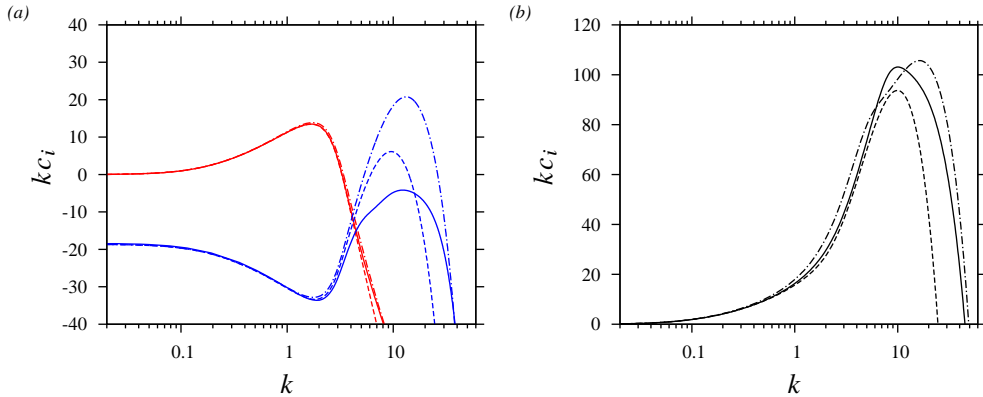


Figure 30: Accounting for temporal and spatial derivatives of T_G and P_G in (3.6a). Temporal linear stability predictions based on three approaches for conditions according to figure 24: $Ka=3174$ (water and air I in table 1), $H^*=13$ mm, $\phi=5^\circ$, $Re_L=43.1$. Dot-dashed: WRIBL-OS (3.41), solid: OS-OS (4.20) and (4.21), dashed: WRIBL-OS including derivatives of T_G and P_G in (3.6a). (a) $Re_G=-4700$. Red: long-wave Kapitza mode, blue: short-wave mode; (b) $Re_G=-6760$: merged mode.

1350 In summary, accounting for the derivatives of T_G and P_G does not meaningfully improve
 1351 predictions at low wave numbers k . And, at large k , it may even deteriorate them. This is
 1352 because the WRIBL-OS description becomes unbalanced at large k , as a result of truncating
 1353 the governing equations at different orders in the liquid (truncate at $O(\epsilon^2)$ and neglect
 1354 $O(\epsilon^2 Re_L)$ inertial corrections) and gas (full governing equations). Retaining supplementary
 1355 terms in the governing equations has been shown to deteriorate long-wave model predictions
 1356 in other configurations (Oron & Gottlieb 2004; Thompson *et al.* 2019). It is interesting to
 1357 note that both the new short-wave (panel 30a) and merged (panel 30b) instability modes can
 1358 be captured by the WRIBL approach.

1359 **Acknowledgements.** Johannes Amrani, Alban Aubertin, Lionel Auffray, and Rafael
 1360 Pidoux contributed to building the experimental setup.

1361 **Declaration of Interests.** The authors report no conflict of interest.

REFERENCES

- 1362 ALEKSEENKO, S. V., AKTERSHEV, S. P., CHERDANTSEV, A. V., KHARLAMOV, S. M. & MARKOVICH, D. M.
 1363 2009 Primary instabilities of liquid film flow sheared by turbulent gas stream. *International Journal*
 1364 *of Multiphase Flow* **35**, 617–627.
- 1365 ALEKSEENKO, S. V., ANTIPIN, V. A., BOBYLEV, A. V. & MARKOVICH, D. M. 2007 Application of PIV to
 1366 velocity measurements in a liquid film flowing down an inclined cylinder. *Experiments in Fluids*
 1367 **43** (2-3), 197–207.
- 1368 AZZOPARDI, B. J., MUDE, R. F., LO, S., MORVAN, H., YAN, Y. & ZHAO, D. 2011 *Hydrodynamics of*
 1369 *Gas-Liquid Reactors: Normal Operation and Upset Conditions*. John Wiley & Sons.
- 1370 BANKOFF, S. G. & LEE, S. C. 1986 *A critical review of the flooding literature*, vol. 2, pp. 95–180. Springer
 1371 Berlin Heidelberg.
- 1372 BARMAK, I., GELFGAT, A., ULLMAN, A. & BRAUNER, N. 2016a Stability of stratified two-phase flows in
 1373 inclined channels. *Physics of Fluids* **28**, 084101.
- 1374 BARMAK, I., GELFGAT, A., VITOSHKIN, H., ULLMAN, A. & BRAUNER, N. 2016b Stability of stratified two-phase
 1375 flows in horizontal channels. *Physics of Fluids* **28**, 044101.
- 1376 BOOMKAMP, P. A. M., BOERSMA, B. J., MIESEN, R. H. M. & BEIJNON, G. V. 1997 A Chebyshev collocation
 1377 method for solving two-phase flow stability problems. *Journal of Computational Physics* **132**, 191–
 1378 200.

- 1379 BROOKE BENJAMIN, T. 1957 Wave formation in laminar flow down an inclined plane. *J. Fluid Mech.* **2**,
1380 554–574.
- 1381 BROOKE BENJAMIN, T. 1959 Shearing flow over a wavy boundary. *J. Fluid Mech.* **6**, 161–205.
- 1382 CAMASSA, R., OGROSKY, H. R. & OLANDER, J. 2017 Viscous film-flow coating the interior of a vertical tube.
1383 part 2. air-driven flow. *Journal of Fluid Mechanics* **825**, 1056–1090.
- 1384 CHANG, H. C., DEMEKHIN, E. A. & KALALIDIN, E. 1996a Simulation of noise-driven wave dynamics on a
1385 falling film. *AIChE J.* **42** (6), 1553–1568.
- 1386 CHANG, H. C., DEMEKHIN, E. A., KALALIDIN, E. & YE, Y. 1996b Coarsening dynamics of falling-film solitary
1387 waves. *Phys. Rev. E* **54** (2), 1467–1477.
- 1388 COHEN, L. S. & HANRATTY, T. J. 1968 Effect of waves at a gas—liquid interface on a turbulent air flow.
1389 *Journal of Fluid Mechanics* **31** (3), 467–479.
- 1390 COHEN-SABBAN, J., GAILLARD-GROLEAS, J. & CREPIN, P.-J. 2001 Quasi-confocal extended field surface
1391 sensing. In *Proceedings of SPIE* (ed. A. Duparre & B. Singh), *Optical Metrology Roadmap for the*
1392 *Semiconductor, Optical, and Data Storage Industries II*, vol. 4449, pp. 178–183.
- 1393 DEMEKHIN, E. A. 1981 Nonlinear waves in a liquid film entrained by a turbulent gas stream. *Fluid Dyn.* **16**,
1394 188–193.
- 1395 DIETZE, G. F. 2016 On the Kapitza instability and the generation of capillary waves. *Journal of Fluid*
1396 *Mechanics* **789**, 368–401.
- 1397 DIETZE, G. F. 2019 Effect of wall corrugations on scalar transfer to a wavy falling liquid film. *Journal of*
1398 *Fluid Mechanics* **859**, 1098–1128.
- 1399 DIETZE, G. F. & RUYER-QUIL, C. 2013 Wavy liquid films in interaction with a confined laminar gas flow. *J.*
1400 *Fluid Mech.* **722**, 348–393.
- 1401 DOEDEL, E. J. 2008 AUTO07P: Continuation and bifurcation software for ordinary differential equations.
1402 *Montreal Concordia University*.
- 1403 DROSOS, E. I. P., PARAS, S. V. & KARABELAS, A. J. 2006 Counter-current gas-liquid flow in a vertical narrow
1404 channel - liquid film characteristics and flooding phenomena. *Int. J. Multiphase Flow* **32**, 51–81.
- 1405 FAIR, J. R. & BRAVO, J. L. 1990 Distillation columns containing structured packing. *Chemical Engineering*
1406 *Progress* **86** (1), 19–29.
- 1407 FLORYAN, J. M., DAVIS, S. H. & KELLY, R. E. 1987 Instabilities of a liquid film flowing down a slightly
1408 inclined plane. *Phys. Fluids* **30** (4), 983–989.
- 1409 FREDERICK, K. A. & HANRATTY, T. J. 1988 Velocity measurements for a turbulent nonseparated flow over
1410 solid waves. *Experiments in Fluids* **6** (7), 477–486.
- 1411 HALPERN, D. & GROTBORG, J. B. 2003 Nonlinear saturation of the rayleigh-instability due to oscillatory flow
1412 in a liquid-lined tube. *J. Fluid Mech.* **492**, 251–270.
- 1413 HANRATTY, T. J. & ENGEN, J. M. 1957 Interaction between a turbulent air stream and a moving water surface.
1414 *AIChE Journal* **3** (3), 299–304.
- 1415 KALLIADASIS, S., RUYER-QUIL, C., SCHEID, B. & VELARDE, M. G. 2012 *Falling Liquid Films, Applied*
1416 *Mathematical Sciences*, vol. 176. Springer Verlag.
- 1417 KAPITZA, P. L. 1948 Wave flow of thin layer of viscous fluid (in Russian). *Zhurn. Eksper. Teor. Fiz.* **18** (1),
1418 3–28.
- 1419 KOFMAN, N. 2014 Films liquides tombants avec ou sans contre-écoulement de gaz: application au problème
1420 de l'engorgement dans les colonnes de distillation. PhD thesis, Université Pierre et Marie Curie.
- 1421 KOFMAN, N., MERGUI, S. & RUYER-QUI, C. 2014 Three-dimensional instabilities of quasi-solitary waves in
1422 a falling liquid film. *Journal of Fluid Mechanics* **757**, 854–887.
- 1423 KOFMAN, N., MERGUI, S. & RUYER-QUIL, C. 2017 Characteristics of solitary waves on a falling liquid film
1424 sheared by a turbulent counter-current gas flow. *Int. J. Multiph. Flow* **95**, 22–34.
- 1425 KUPFER, K., BERS, A. & RAM, A. K. 1987 The cusp map in the complex-frequency plane for absolute
1426 instabilities. *Physics of Fluids* **30** (10), 3075–3082.
- 1427 KUSHNIR, R., BARMAK, I., ULLMANN, A. & BRAUNER, N. 2021 Stability of gravity-driven thin-film flow in
1428 the presence of an adjacent gas phase. *International Journal of Multiphase Flow* **135**, 103443.
- 1429 LAPKIN, A. & ANASTAS, P. T., ed. 2018 *Green Chemical Engineering, Handbook of Green Chemistry*,
1430 vol. 12. Wiley-VHC.
- 1431 LAVALLE, G., GRENIER, N., MERGUI, S. & DIETZE, G. F. 2020 Solitary waves on superconfined falling liquid
1432 films. *Physical Review Fluids* **5** (3), 032001(R).
- 1433 LAVALLE, G., LI, Y., MERGUI, S., GRENIER, N. & DIETZE, G. F. 2019 Suppression of the kapitza instability
1434 in confined falling liquid films. *Journal of Fluid Mechanics* **860**, 608–639.

- 1435 LAVALLE, G., MERGUI, S., GRENIER, N. & DIETZE, G. F. 2021 Superconfined falling liquid films: linear
1436 versus nonlinear dynamics. *Journal of Fluid Mechanics Rapids* **919**, R2.
- 1437 LEL, V.V., AL-SIBAI, F., LEEFKEN, A. & RENZ, U. 2005 Local thickness and wave velocity measurement
1438 of wavy films with a chromatic confocal imaging method and a fluorescence intensity technique.
1439 *Experiments in Fluids* **39** (5), 856–864.
- 1440 LIU, J. & GOLLUB, J. P. 1993 Onset of spatially chaotic waves on flowing films. *Physical Review Letters*
1441 **70** (15), 2289–2292.
- 1442 LIU, J. & GOLLUB, J. P. 1994 Solitary wave dynamics of film flows. *Physics of Fluids* **6** (5), 1702–1712.
- 1443 LUCHINI, P. & CHARRU, F. 2019 On the large difference between Benjamin’s and Hanratty’s formulations of
1444 perturbed flow over uneven terrain. *Journal of Fluid Mechanics* **871**, 534–561.
- 1445 MATLAB 2015 *Version 8.6 (R2015b)*. Natick, Massachusetts: The MathWorks Inc.
- 1446 MCCREADY, M. J. & CHANG, H.-C. 1994 Formation of large disturbances on sheared and
1447 falling liquid films. *Chemical Engineering Communications* **141-142** (1), 347–358, arXiv:
1448 <http://www.tandfonline.com/doi/pdf/10.1080/00986449608936423>.
- 1449 MERGUI, S., LAVALLE, G., LI, Y., GRENIER, N. & DIETZE, G. F. 2023 Nonlinear dynamics of strongly-confined
1450 gas-sheared falling liquid films. *Journal of Fluid Mechanics* **954**, A19.
- 1451 MEZA, C. E. & BALAKOTAIAH, V. 2008 Modeling and experimental studies of large amplitude waves on
1452 vertically falling films. *Chemical Engineering Science* **63**, 4704–4734.
- 1453 MIESEN, R. & BOERSMA, B. J. 1995 Hydrodynamic stability of a sheared liquid film. *J. Fluid Mech.* **301**,
1454 175–202.
- 1455 MILES, J. W. 1957 On the generation of surface waves by shear flows. *J. Fluid Mech.* **3**, 185–204.
- 1456 MIYARA, A. 1999 Numerical analysis on flow dynamics and heat transfer of falling liquid films with
1457 interfacial waves. *Heat and Mass Transfer* **35**, 298–306.
- 1458 MOISY, F., RABAUD, M. & SALSAC, K. 2009 A synthetic schlieren method for the measurement of the
1459 topography of a liquid interface. *Experiments in Fluids* **46**, 1021–1036.
- 1460 NÁRAIGH, L. Ó., SPELT, P. D. M., MATAR, O. K. & ZAKI, T. A. 2011 Interfacial instability in turbulent flow
1461 over a liquid film in a channel. *International Journal of Multiphase Flow* **37** (7), 812–830.
- 1462 ORON, A. & GOTTLIEB, O. 2004 Subcritical and supercritical bifurcations of the first- and second-order
1463 Benney equations. *Journal of Engineering Mathematics* **50** (2-3), 121–140.
- 1464 ORSZAG, S. A. 1971 Accurate solution of the Orr-Sommerfeld stability equation. *Journal of Fluid Mechanics*
1465 **50** (4), 689–703.
- 1466 ÖZGEN, S., CARBONARO, M. & SARMA, G. S. R. 2002 Experimental study of wave characteristics on a thin
1467 layer of de/anti-icing fluid. *Physics of Fluids* **14** (10), 3391–3402.
- 1468 POPE, S. B. 2000 *Turbulent Flows*. Cambridge University Press.
- 1469 PRANDTL, L. 1925 Bericht über Untersuchungen zur ausgebildeten Turbulenz. *Zeitschrift für angewandte*
1470 *Mathematik und Mechanik* **5**, 136–139.
- 1471 RICHARD, G., RUYER-QUIL, C. & VILA, J. P. 2016 A three-equation model for thin films down an inclined
1472 plane. *Journal of Fluid Mechanics* **804**, 162–200.
- 1473 RUSSO, S. & LUCHINI, P. 2016 The linear response of turbulent flow to a volume force: comparison between
1474 eddy-viscosity model and dns. *Journal of Fluid Mechanics* **790**, 104–127.
- 1475 RUYER-QUIL, C. & MANNEVILLE, P. 1998 Modeling film flows down inclined planes. *Eur. Phys. J. B* **6** (2),
1476 277–292.
- 1477 RUYER-QUIL, C. & MANNEVILLE, P. 2000 Improved modeling of flows down inclined planes. *Eur. Phys. J.*
1478 *B* **15** (2), 357–369.
- 1479 RUYER-QUIL, C. & MANNEVILLE, P. 2002 Further accuracy and convergence results on the modeling of flows
1480 down inclined planes by weighted-residual approximations. *Phys. Fluids* **14** (1), 170–183.
- 1481 SAMANTA, A. 2014 Shear-imposed falling film. *Journal of Fluid Mechanics* **753**, 131–149.
- 1482 SAMANTA, A. 2020 Optimal disturbance growth in shear-imposed falling film. *AIChE Journal* **66** (5),
1483 0001–1541.
- 1484 SCHMIDT, P., NÁRAIGH, L. Ó., LUCQUIAUD, M. & VALLURI, P. 2016 Linear and nonlinear instability in vertical
1485 counter-current laminar gas-liquid flows. *Physics of Fluids* **28**, 042102.
- 1486 SHKADOV, V. YA. 1967 Wave flow regimes of a thin layer of viscous fluid subject to gravity. *Fluid Dyn.* **2** (1),
1487 29–34.
- 1488 THOMPSON, A. B., GOMES, S. N., DENNER, F., DALLASTON, M. C. & KALLIADASIS, S. 2019 Robust low-
1489 dimensional modelling of falling liquid films subject to variable wall heating. *Journal of Fluid*
1490 *Mechanics* **877**, 844–881.

- 1491 THORSNESS, C. B., MORRISROE, P. E. & HANRATTY, T. J. 1978 A comparison of linear theory with
1492 measurements of the variation of shear stress along a solid wave. *Chem. Eng. Sci.* **33**, 579–592.
- 1493 TILLEY, B. S., DAVIS, S. H. & BANKOFF, S. G. 1994 Linear stability theory of two-layer fluid flow in an
1494 inclined channel. *Phys. Fluids* **6** (12), 3906–3922.
- 1495 TREFETHEN, L. N. 2000 *Spectral methods in MATLAB*. Philadelphia: SIAM.
- 1496 TRIFONOV, Y. Y. 2010a Counter-current gas-liquid wavy film flow between the vertical plates analyzed using
1497 the Navier-Stokes equations. *AIChE Journal* **56** (8), 1975–1987.
- 1498 TRIFONOV, Y. Y. 2010b Flooding in two-phase counter-current flows: Numerical investigation of the gas-
1499 liquid wavy interface using the Navier-Stokes equations. *Int. J. Multiphase Flow* **36**, 549–557.
- 1500 TRIFONOV, Y. Y. 2017 Instabilities of a gas-liquid flow between two inclined plates analyzed using the
1501 Navier-Stokes equations. *International Journal of Multiphase Flow* **95**, 144–154.
- 1502 TRIFONOV, Y. Y. 2019 Nonlinear wavy regimes of a gas-liquid flow between two inclined plates analyzed
1503 using the Navier-Stokes equations. *International Journal of Multiphase Flow* **112**, 170–182.
- 1504 TSELUIKO, D. & KALLIADASIS, S. 2011 Nonlinear waves in counter-current gas-liquid film flow. *J. Fluid*
1505 *Mech.* **673**, 19–59.
- 1506 VALLURI, P., MATAR, O. K., HEWITT, G. F. & MENDES, M. A. 2005 Thin film flow over structured packings
1507 at moderate Reynolds numbers. *Chem. Eng. Sci.* **60**, 1965–1975.
- 1508 VAN DRIEST, E. R. 1956 On turbulent flow near a wall. *Journal of the Aeronautical Sciences* **23** (11),
1509 1007–1011, arXiv: <https://doi.org/10.2514/8.3713>.
- 1510 VELLINGIRI, R., TSELUIKO, D. & KALLIADASIS, S. 2015 Absolute and convective instabilities in counter-
1511 current gas-liquid film flows. *Journal of Fluid Mechanics* **763**, 166–201.
- 1512 VLACHOS, N. A., PARAS, S. V., MOUZA, A. A. & KARABELAS, A. J. 2001 Visual observations of flooding in
1513 narrow rectangular channels. *Int. J. Multiphase Flow* **27**, 1415–1430.
- 1514 YIH, C. S. 1963 Stability of liquid flow down an inclined plane. *The Physics of Fluids* **6** (3), 321–334.
- 1515 YOSHIMURA, P. N., NOSOKO, P. & NAGATA, T. 1996 Enhancement of mass transfer into a falling laminar liquid
1516 film by two-dimensional surface waves—some experimental observations and modeling. *Chemical*
1517 *Engineering Science* **51** (8), 1231–1240.
- 1518 ZAPKE, A. & KRÖGER, D. G. 2000 Countercurrent gas-liquid flow in inclined and vertical ducts - I: Flow
1519 patterns, pressure drop characteristics and flooding. *International Journal of Multiphase Flow* **26**,
1520 1439–1455.
- 1521 ZHOU, G. & PROSPERETTI, A. 2020 Capillary waves on a falling film. *Physical Review Fluids* **5**, 114005.
- 1522 ZILKER, D. P., COOK, G. W. & HANRATTY, T. J. 1977 Influence of the amplitude of a solid wavy wall on a
1523 turbulent flow. part 1. non-separated flows. *Journal of Fluid Mechanics* **82** (1), 29–51.